ISSN 1732-9353
eISSN 2543-7496

Scientific Review

Engineering and Environmental Sciences

Przegląd Naukowy
Inżynieria i Kształtowanie Środowiska

Vol. 30 (3) 2021 Issue 93
Quarterly

Scientific Review Engineering and Environmental Sciences Vol. 30 (3) 2021 Issue 93

SCIENTIFIC REVIEW
ENGINEERING AND ENVIRONMENTAL SCIENCES
Quarterly

The list of reviewers is published in the last issue of the volume and on the http://iks_pn.sggw.pl

EDITORIAL OFFICE ADDRESS
Wydział Budownictwa i Inżynierii Środowiska SGGW
ul. Nowoursynowska 159, 02-776 Warsaw, Poland
tel. (+48 22) 59 35 363, 59 35 210, 59 35 302
e-mail: srees@sggw.edu.pl
http://iks_pn.sggw.pl

ISSN 1732-9353
e-ISSN 2543-7496

Printed version of the Scientific Review Engineering and Environmental Sciences is primary version

All papers are indexed in the data bases as follows: AGRO(Poznań), BazTech, Biblioteka Nauki, **CrossRef**, **DOAJ**, **Google Scholar**, **Index Copernicus**, INFONA, POL-Index, **SCOPUS**, SIGŻ(CBR)

Instruction for Authors

The journal publishes in English languages, peer-reviewed original research, critical reviews and short communications, which have not been and will not be published elsewhere in substantially the same form. Author of an article is required to transfer the copyright to the journal publisher, however authors retain significant rights to use and share their own published papers. The published papers are available under the terms of the principles of Open Access Creative Commons CC BY-NC license. The submitting author must agree to pay the publication charge (see Charges).

The author of submitted materials (e.g. text, figures, tables etc.) is obligated to restricts the publishing rights. All contributors who do not meet the criteria for authorship should be listed in an Acknowledgements section of the manuscript. Authors should, therefore, add a statement on the type of assistance, if any, received from the sponsor or the sponsor's representative and include the names of any person who provided technical help, writing assistance, editorial support or any type of participation in writing the manuscript.

Uniform requirements for manuscripts

Manuscript should be sent with tables, graphs and abstract on separate pages by e-mail: iks_pn@sggw.edu.pl. All figures and tables should be placed near their reference in the main text and additionally sent in a form of data files (e.g. Excel, Visio, Adobe Illustrator, Adobe Photoshop, CorelDRAW). Figures are printed in black and white on paper version of the journal (color printing is combined with an additional fee calculated on a case-by-case basis), while on the website are published in color.

The size of the manuscript should be limited up to 10 pages including overview, summary, references and figures (the manuscript more than 13 pages is unacceptable); Please set the text format in single column with paragraphs (A4 paper format), all margins to 25 mm, use the font Times New Roman, typeface 12 points and line spacing one and half.

The submitted manuscript should include the following parts:

- name and SURNAME of the author(s) – up to 5 authors
- affiliation of the author(s), ORCID Id (optional)
- title of the work
- key words
- abstract (about 500 characters)
- text of the paper divided into: Introduction, Material and Methods, Results and Discussion, Conclusions, References and Summary
- references in APA style are listed fully in alphabetical order according to the last name of the first author and not numbered; please find the details below
- post and mailing address of the corresponding author:

  Author's address:
  Name, SURNAME
  Affiliation
  Street, number, postal code, City
  Country
  e-mail: adress@domain

- Plagiarism statement (http://iks.pn.sggw.pl/Szablony/PublEth.pdf)

Reference formatting

In the Scientific Review Engineering and Environmental Sciences the APA 6th edition style is used.

Detailed information

More information can be found: http://iks.pn.sggw.pl

Scientific Review

Engineering and Environmental Sciences

Przegląd Naukowy

Inżynieria i Kształtowanie Środowiska

Vol. 30 (3) 2021 Issue 93

Contents

Editorial work – Anna Dołomisiewicz, Elżbieta Wojnarowska

ISSN 1732-9353 eISSN 2543-7496

Printing: Libra-Print, al. Legionów 114B, 18-400 Łomża

Scientific Review – Engineering and Environmental Sciences (2021), 30 (3), 379–387
Sci. Rev. Eng. Env. Sci. (2021), 30 (3)
Przegląd Naukowy – Inżynieria i Kształtowanie Środowiska (2021), 30 (3), 379–387
Prz. Nauk. Inż. Kszt. Środ. (2021), 30 (3)
http://iks.pn.sggw.pl
DOI 10.22630/PNIKS.2021.30.3.32

Ahmed S. HASSAN, Hasan M. AZEEZ

Mustansiriyah University, College of Science

Relation between CO_2 emissions and crude oil combustion in Iraq

Key words: CO_2 emission, crude oil, CO_2 concentration, Iraq

Introduction

The main issue of climate changes that the rapidly increasing of carbon dioxide emissions. Human activities results in emissions for four main greenhouse gases (GHGs): carbon dioxide (CO_2), methane (CH_4), nitrous oxide (N_2O), and hydrofluorocarbons (HFCs). These gases accumulate in atmosphere, then affecting the Earth's energy balance (Shahzad, 2015). The main part of these emissions came from combustion fossil fuel to use in transportation, electricity production, building heating and cooling, manufacture of cement and other goods. Annual average of NO_2 over Iraq increased as linear growth rate 9.8 per year, because the anthropogenic emissions, topography and weather conditions (Rajab, Hassan, Kadhum, Al-Salihi & San Lim, 2020). Carbon dioxide emission from fossil fuel combustion and processes contributed about 78% of the total GHGs emission increase from 1970 to 2010 (Blanco et al., 2014). Global warming began from increased CO_2 concentration is widely considered as main risk for Earth life. The role of CO_2 emission in relationship with increased global surface temperature, that pointed out to debate on accuracy of temperature reconstructions as well as on the exact impact that CO_2 has on global warming (Florides & Christodoulides, 2009).

Carbon dioxide emissions are the main results of burning fossil fuels, and given the important role it plays in climate change, that need to understand the uncertain spatial estimates of these emissions by relying on network data. This data has been studied in the United States, where a total estimate of emissions is made in the states, based on large volume sources and locations of the size of the large points of that network as well

as the distribution and size of the non--point sources, as there are other sources of greenhouse CO_2 gases. In order to determine spatial emissions, they are measured by fossil fuels and industrial processes observed by Boden, Andres and Marland (2017). Energy data statistics can also estimate the time series of CO_2 emissions produced by the initial flow of fossil fuels, as the flow of CO_2 increased in an unimaginable way during the World War I, however were represented by time series for the period from 1751 to 1950, represented by the total emission of CO_2, even during the Industrial Revolution (Andres et al., 2012). The rate growth of total cumulative CO_2 emissions continues to grow during present times, generating debate on the probability of enhanced greenhouse warming. China is largest energy consuming and CO_2 emitter, developed methods for constructing CO_2 emissions for Chinese cities based on energy balance table. This construction, according to the regional emissions report of the Intergovernmental Panel on Climate Change (IPCC), as emissions in social and economic sectors reached 47, 17 fossil fuels, and 9 primary industrial products, and examined uncertainties inventories basis for many climate polices (Shan et al., 2017). The consequence of environmental changing, not only on climate but also on the ecosystems, it is urgent needed to improve the predictive skills of the models used for instance in the prediction models organized by the IPCC. Where total carbon emission was 9 Gt in 2016 as result of fossil fuel combustions. The comparisons between the different methods used to estimate the spatial and temporal air – sea interactions of carbon substantial discrepancies both regional and temporal, this lead to understand the role played by these interactions in the functioning of the ecosystems (Aumont, 2016). Many publications about the carbon emission research domain, which has been more visible especially during 2016–2018. The most significant contribution to the domain was reported from China, United States, and England. While most prolific authors and institutions of the domain were from China, reported the best connection links. It was revealed that evaluating greenhouse gas emissions and estimating the carbon footprint was well known among the researchers. Moreover, climate change and environmental effects of carbon emissions were also significant points of concern in carbon emission research (Udara Willhelm Abeydeera, Wadu Mesthrige & Samarasinghalage, 2019). The carbon monoxide (CO) affecting air quality and climate and acts as a serious indirect GHGs. The vertical distribution of CO over Iraq found that seasonal difference, where winter recorded higher value of CO than summer and autumn. The satellite measurement are able to determine the increased of atmospheric CO concentration over varied region (Abdulfattah, Rajab, Al-Salihi, Suliman & Lim, 2020).

Munn (2019) focus on global fossil CO_2 emissions had increased in last three years consecutively: +1.5% in 2017, +2.1% in 2018, and +0.6% in 2019. Economic indicators and trends in global natural gas and oil use suggest a further rise in emissions in 2020. Global CO_2 emissions from oil increased over the next decade or more. Stronger global commitments and carbon pricing would help implement such policies at scale

and in time. Moreover (Hassan & Zaki, 2018) studied for three states of fossil fuel in Iraq, the analysis of CO_2 emissions and for three types of fossil fuels: gas, liquid, steel, gases emitted from these cases are considered greenhouse gases, which in turn affect the radiation balance of the Earth, where the emission density is the average rate of emission. Therefore, the burning of carbon since the Industrial Revolution increased the concentration of CO_2 in the atmosphere, as results showed that the consumption of gaseous fuel increased by about 10 times, up to 1,045.10 kt, the CO_2 emission presented from the consumption of fossil fuels increased by 10.4 greater than it was, which reached to 86,759 kt. The per capita gross domestic production (GDP) was main determinant of CO_2 emissions in global panel, thereby carried out positive effect on CO_2 (Sharma, 2011). The relationship between total of CO_2 emissions and GDP by using the environment Kuznets curve (EKC) model in Iraq. This relationship takes invert U-shape and CO_2 emissions increased more than five times after 2000 than before, that's refer to increased had damage environmental (Al-rukabie, Hassan & Kadhum, 2020). When looking into global carbon intensity of crude oil production by developed the climate intensity (CI) model identify major drives of these emissions, and estimation emissions for 90 countries in 2015 from 8,966 oil fields represent 98% of global crude oil condensation production with above of average global CI. The link between climate and sustainable development are strong. Poor and developing countries, particularly least developed countries, will be among those most adversely affected and least able to cope with the anticipated shocks to their social, economic and natural systems. The goal of this research is to calculate the annual total CO_2 emissions from crude oil in Iraq, then compare the results with estimation of total CO_2 emissions over Iraq. The ratio between annual total CO_2 emissions for Iraq and world found out. The annual CO_2 concentration investigated over Iraq then calculated the percentage of this concentration to annual CO_2 concentration over world.

Methodology and dataset

Iraq is now the second largest producer and exporter in world, and expected to grow its oil production capacity over the next decade and account for a significant share of additional supply. In spite of all these positives have disadvantages; Iraq has faced environmental degradation over by rising CO_2 emissions. The question that is addressed here is how many tons of CO_2 emissions are generated by the crude oil being burned. So that, it is necessary understanding CO_2 molecules weight and the structure of it, beside more information about crude oil. The crude oil weight about 136 kg (159 l), the crude oil has on carbon ratio maximum and that equal 78%. The carbon ratio in one barrel is approximate to 118 kg. The molecular weight of carbon is 12, where molecular weight of oxygen is 16, it has mass of ≈ 16 u, that's mean molecular weight ratio of CO_2 equal to 44; the density of one barrel of oil is 0.85 $g \cdot cm^{-3}$. The crude oil has on carbon ratio maximum and that equal 78%

that means the carbon ratio in one barrel is approximate to 118 kg, so that carbon ratio from total molecular weight is 27.27% of carbon in CO_2. Carbon dioxide emission from one barrel equal 433 kg. The calculation for CO_2 emissions that used in this paper is Eq. (1), it is simple equation depend on crude oil production only, as followed.

$$CO_2\ emission = \frac{P_{oil}}{27.27} = P_{oil} \cdot 3.67 \cdot 0.118 \quad (1)$$

where:
$CO_2\ emission$ – carbon dioxide emission from crude oil,
P_{oil} – crude oil prediction.

The sources of datasets consist of three parts: first, dataset for crude oil production in Iraq for period of 1980–2018. These datasets available from Trading Economics Application Programming Interface (TEAPI) provides direct access to annual crude oil production for Iraq. The second source provides data was the Carbon Dioxide Information Analysis Center (CDIAC) annual data used in this study to compare between Iraq and global emissions (Andres et al., 2012; Andres, Boden & Higdon, 2014). The CDIAC' estimates of CO_2 emissions from fossil-fuel consumption for annual total CO_2 emissions data for Iraq and world sourced from CDIAC for long period (1980–2014) to found out the ratio between of them (Andres et al., 2014). Third dataset was annual averaged of CO_2 concentration observed data provide in parts per million (ppm), for Iraq from 2002 to 2016, while for world in 1980–2018 (Friedlingstein et al., 2019).

Results and discussion

Carbon dioxide is continuously emitted into the atmosphere through several processes, such as those from fossil fuel combustion, black oil refining, unstopped engines and even plants. The amount of this gas emitted from these sources varies by location and time. Therefore, the CO_2 emissions from fossil fuel for Iraq was calculated by using the Eq. (1) depend on amount of crude oil production carbon thereby determined the amount of CO_2 emitted from it. The results carried out the heights value of emission was in 2018 that reach to 1.97 Mt, however the last four years begin this rise of emissions from 2012 (1.29 Mt) to end of study period; that represented the highest period of emissions than whole period study as shown in Figure 1. The minimum value of CO_2 emissions was 0.1 Mt in 1991, compatible with the lower crude oil production was in 1992–1996 (0.2 Mt) because that Iraq was under economic embargo of UN and the crude oil production was so limited. The next period witnessed fluctuation in production, and therefore the amount of CO_2 emissions was fluctuating, in contrast to the subsequent period, which found that there was a slowly increase to reach maximum values at the end of the study period with oil production more than 4 million barrels per day, then the emission activity returned and remained to this day without providing any clarifications or treatments.

The main common between CO_2 emissions for Iraq and world that have same behavior, rapidly increased, especially in last decade of this study as shown in Figure 2. There was a clear increased in the quantities of emissions gradually

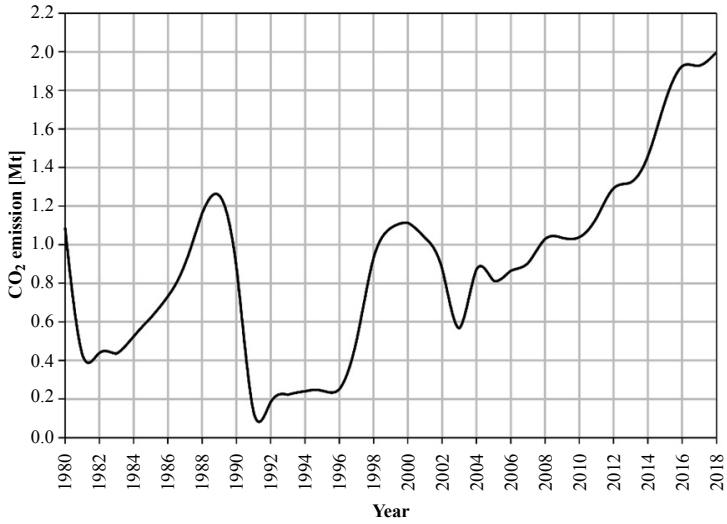

FIGURE 1. Time series for calculated of total CO_2 emissions from crude oil for period of 1980–2018 of Iraq

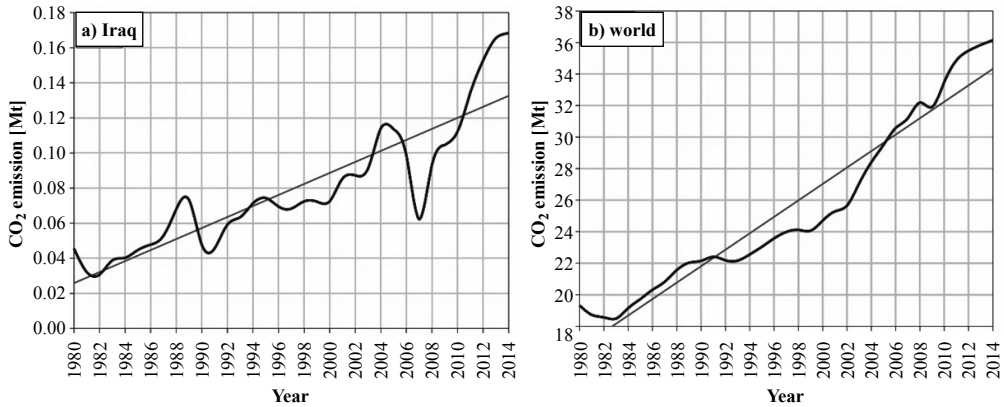

FIGURE 2. Time series of annual CO_2 emissions from fossil fuel production in 1980–2014 for Iraq (a) and the world (b)

and represented from 1980 to 2014 for both Iraq and the world, but there was a different slope of the average line, that was 0.5 for the world and 0.003 for Iraq. This means that the average global CO_2 emissions are 166.6 times higher than that of Iraq. The behavior of two curves were similar in Figure 2 except for the middle of the study period (1990–2008), where Iraqi emissions recorded a decline in 1991 and 2007 (0.042 and 0.061 Mt, respectively), while the world was emissions during the same the period was below the average slope line. Both world and Iraqi CO_2 emissions were increased as exponential function from 2008 to end of study period (2014) to reach 36 and 0.17 Mt, respectively.

Considering that the converging behavior between CO_2 emissions for Iraq and the world leads to divide the Iraqi CO_2 emissions to total CO_2 global emissions, to achieve this goal calculating the ratio from fossil fuel between them as shown in the table from period 1980 to 2008. This ratio explain that two different periods have different variance; first period (1981–1997) that change approximately 0.0001 each year, while second period (1998–2008) change 0.0001 each two–three years, and the high ratio found in 2008 (0.0034). These ratios for both periods were very small to refer CO_2 emission for Iraq was very low compared to world's emissions.

The atmosphere contains a range of greenhouse gases and the most important of these gases is CO_2 emitted to the atmosphere through several processes and several ways where this emission can have concentrations vary from place to place because of GCM as the movement of the wind cycle in the atmosphere important in reducing or increasing CO_2 concentrations over the duration of history. Where the results showed that the concentrations of CO_2 gas, which existed since industrial revolution in increasing till today as non-liner functions.

Carbon dioxide concentration for Iraq as represented in Figure 3, show the growth rate of 1.875 ppm per year, with continuity increased from 375.93 ppm in 2002 to reach highest value of 403 ppm was in 2016. Statistics indicated that Iraq is one of the countries in dealing with CO_2 emissions according to international agreements, in spite of despite that; it is consistent with the concentrations when compared to the world concentrations.

The global CO_2 concentrations shown slowly increased with slop the average line equal to 1.75 ppm per year, from minimum value of 338.6 ppm was in 1980, while maximum value of 407.05 ppm was in 2018, that means three of the four highest annual increases have occurred in the past four years. It's no coincidence that the last four years also had the highest CO_2 emissions on record. Undoubtedly, there is no decrease in CO_2 concentrations unless emissions are addressed. Compared to Iraq's CO_2 concentrations, there is also an increase in concentrations due to emissions, concentrations increased approximately two times through study period.

TABLE. The ratio between CO_2 emissions from fossil fuel for Iraq to world in 1981–2008

Year	Ratio	Year	Ratio	Year	Ratio	Year	Ratio
1981	0.002049	1988	0.002576	1995	0.002938	2002	0.003243
1982	0.002142	1989	0.002643	1996	0.00299	2003	0.003284
1983	0.002230	1990	0.002675	1997	0.00304	2004	0.003303
1984	0.002314	1991	0.002738	1998	0.003088	2005	0.003342
1985	0.002354	1992	0.002798	1999	0.003112	2006	0.003379
1986	0.002431	1993	0.002856	2000	0.003157	2007	0.003415
1987	0.002505	1994	0.002854	2001	0.003201	2008	0.003433

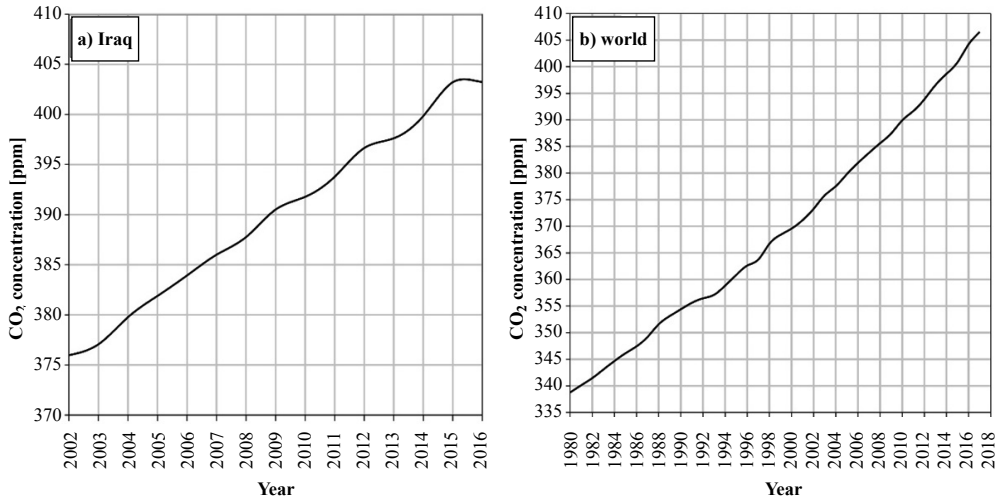

FIGURE 3. Time series of annual CO_2 concentration for Iraq (a) and the world (b) in the 2002–2018

Conclusions

1. Carbon dioxide emissions calculated from crude oil for Iraq was increased from 2012 (1.29 Mt) without any decline to reach end of study period in 2018 (1.97 Mt), while the minimum value was in 1991 (0.1 Mt).
2. Total observed CO_2 emissions increased with different slop of average line that was 0.5 for world, 0.003 for Iraq. The behavior of two carve were similar except decline in 1991 and 2007 in middle period study. The world and Iraq CO_2 emissions were increased exponential function from 2008 to 2014 to reach 36 and 0.17 Mt, respectively.
3. The ratio of Iraqi CO_2 emissions to world CO_2 emission divided into two periods: first period (1980–1997) was 0.0001 each year, while second period (1998–2008) was 0.0001 each two–three years. These results shown that Iraqi CO_2 emissions very small compared with CO_2 emissions.
4. The global CO_2 concentrations slowly increased with slop the average line equal to 1.75 ppm per year, from minimum value was 338.6 ppm in 1980, while maximum value was 407.05 ppm in 2018, that means three of the four highest annual increases have occurred in the past four years. Iraqi CO_2 concentrations was increased two times than before, where highest value of 403 ppm was in 2016. That's mean no decreased in CO_2 concentration unless emissions addressed.

References

Abdulfattah, I.S., Rajab, J.M., Al-Salihi, A.M., Suliman, A. & Lim, H.S. (2020). Observed vertical distribution of tropospheric carbon monoxide during 2012 over Iraq. *Scientific Review – Engineering and Environmental Sciences*, *29*(2), 184-195.

Al-rukabie, J.S.A., Hassan, A.S. & Kadhum, J.H. (2020). Empirical analysis of CO_2 emission using EKC model in Iraq. *International Journal of Advanced Science and Technology*, *29*(3), 557-564.

Andres, R.J., Boden, T.A. & Higdon, D. (2014). A new evaluation of the uncertainty associated with CDIAC estimates of fossil fuel carbon dioxide emission. *Tellus B: Chemical and Physical Meteorology*, *66*(1), 23616. https://doi.org/10.3402/tellusb.v66.23616

Andres, R.J., Boden, T.A., Bréon, F.M., Ciais, P., Davis, S., Erickson, D., Gregg, J.S., Jacobson, A., Marland, G., Miller, J., Oda, T., Olivier, J.G.J., Raupach, M.R. & Treanton, K. (2012). A synthesis of carbon dioxide emissions from fossil-fuel combustion. *Biogeosciences*, *9*(5), 1845-1871.

Aumont, O. (2016). *Étude des cycles biogéochimiques marins au moyen de la modélisation* [*Study on marine geochemical cycles using modelling*]. Paris: Sorbonne University.

Blanco, G., Gerlagh, R., Suh, S., Barrett, J., Coninck, H.C. de, Morejon, C.F.D., Mathur, R., Nakicenovic, N., Ahenkorah, A.O., Pan, J., Pathak, H., Rice, J., Richels, R., Smith, S.J., Stern, D.I., Toth, F.L. & Zhou, P. (2014). Drivers, trends and mitigation. In *Climate Change 2014: Mitigation of Climate Change. Contribution of Working Group III to the Fifth Assessment Report of the Intergovernmental Panel on Climate Change* (pp. 351-411). Cambridge: Cambridge University Press.

Boden, T., Andres, R. & Marland, G. (2017). *Global, Regional, and National Fossil-Fuel CO2 Emissions (1751–2014) (V. 2017)*. https://doi.org/10.3334/CDIAC/00001_V2017

Florides, G.A. & Christodoulides, P. (2009). Global warming and carbon dioxide through sciences. *Environment International*, *35*(2), 390-401.

Friedlingstein, P., Jones, M.W., O'Sullivan, M., Andrew, R.M., Hauck, J., Peters, G.P., Peters, W., Pongratz, J., Sitch, S., Le Quéré, C., Bakker, D.C.E., Canadell, J.G., Ciais, P., Jackson, R.B., Anthoni, P., Barbero, L., Bastos, A., Bastrikov, V., Becker, M., Bopp, L., Buitenhuis, E., Chandra, N., Chevallier, F., Chini, L.P., Currie, K.I., Feely, R.A., Gehlen, M., Gilfillan, D., Gkritzalis, T., Goll, D.S., Gruber, N., Gutekunst, S., Harris, I., Haverd, V., Houghton, R. A., Hurtt, G., Ilyina, T., Jain, A.K., Joetzjer, E., Kaplan, J.O., Kato, E., Klein Goldewijk, K., Korsbakken, J.I., Landschützer, P., Lauvset, S. K., Lefčvre, N., Lenton, A., Lienert, S., Lombardozzi, D., Marland, G., McGuire, P.C., Melton, J.R., Metzl, N., Munro, D. R., Nabel, J.E.M.S., Nakaoka, S.-I., Neill, C., Omar, A.M., Ono, T., Peregon, A., Pierrot, D., Poulter, B., Rehder, G., Resplandy, L., Robertson, E., Rödenbeck, C., Séférian, R., Schwinger, J., Smith, N., Tans, P.P., Tian, H., Tilbrook, B., Tubiello, F.N., Werf, G.R. van der, Wiltshire, A.J. & Zaehle, S. (2019). Global carbon budget 2019. *Earth System Science Data*, *11*(4), 1783-1838.

Hassan, A.S. & Zaki, K.N. (2018). Decadal Analysis of Carbon Dioxide Emissions from Different State of Fossil Fuels in Iraq. *Indian Journal of Public Health Research & Development*, *9*(12), 865-868.

Munn, C.B. (2019). *Marine microbiology: ecology & applications*. Boca Raton: CRC Press.

Rajab, J.M., Hassan, A.S., Kadhum, J.H., Al-Salihi, A.M. & San Lim, H. (2020). Analysis of tropospheric NO_2 over Iraq using OMI satellite measurements. *Scientific Review – Engineering and Environmental Sciences*, *29*(1), 3-16.

Shahzad, U. (2015). Global warming: Causes, effects and solutions. *Durreesamin Journal*, *1*(4), 1-7.

Shan, Y., Guan, D., Liu, J., Mi, Z., Liu, Z., Liu, J., Schroeder, H., Cai, B., Chen, Y. & Shao, S. (2017). Methodology and applications of city level CO_2 emission accounts in China. *Journal of Cleaner Production*, *161*, 1215-1225.

Sharma, S.S. (2011). Determinants of carbon dioxide emissions: empirical evidence from 69 countries. *Applied Energy*, *88*(1), 376-382.

Udara Willhelm Abeydeera, L.H., Wadu Mesthrige, J. & Samarasinghalage, T.I. (2019). Global research on carbon emissions: a scientometric review. *Sustainability*, *11*(14), 3972. https://doi.org/10.3390/su11143972

Summary

Relation between CO_2 emissions and crude oil combustion in Iraq. Fossil fuel is the main source for CO_2 emissions that causes global warming. This fact is the starting point for this paper, that consider on three different sources of data: crude oil used to calculate CO_2 emissions for Iraq for the period from 1980 to 2018; annual data of total CO_2 emissions available from the Carbon Dioxide Information Analysis Center (CDIAC) for Iraq and the world for the period from 1980 to 2014; and CO_2 concentrations for Iraq for the period from 2002 to 2006 and for the world for the period from 1980 to 2018. The result is a multifaceted according to the dataset sources. Carbon dioxide emissions calculated from Iraqi crude oil was increased from 1.29 Mt in 2012 to 1.97 Mt in 2018. The world and Iraq CO_2 emissions with different slop of average line that was 0.5 for world, 0.003 for Iraq, while increased exponential function from 2008 to 2014 to reach 36 and 0.17 Mt, respectively. The highest value of Iraqi CO_2 concentration was 403 ppm in 2016, while the global CO_2 concentrations slowly increased with slop line equal to 1.75 ppm per year, from minimum value of 338.6 ppm was in 1980, while maximum value of 407.05 ppm was in 2018, that's mean no decreased in CO_2 concentration unless emissions addressed.

Authors' address:
Ahmed S. Hassan – corresponding author
(https://orcid.org/0000-0001-5029-5642)
Mustansiriyah University
College of Sciences
Atmospheric Sciences Department
Palestine Street, postal code 46131, Baghdad
Iraq
e-mail: ahmed.s.atmsc@uomustansiriyah.edu.iq

Hasan M. Azeez
Mustansiriyah University
College of Sciences
Atmospheric Sciences Department
Palestine Street, postal code 46131, Baghdad
Iraq
e-mail: hassan.m.a7878@uomustansiriyah.edu.iq

Scientific Review – Engineering and Environmental Sciences (2021), 30 (3), 388–399
Sci. Rev. Eng. Env. Sci. (2021), 30 (3)
Przegląd Naukowy – Inżynieria i Kształtowanie Środowiska (2021), 30 (3), 388–399
Prz. Nauk. Inż. Kszt. Środ. (2021), 30 (3)
http://iks.pn.sggw.pl
DOI 10.22630/PNIKS.2021.30.3.33

Salwa S. NAIF, Thoalfaqar Al-RBAYEE, Monim H. Al-JIBOORI

Mustansiriyah University, College of Science

Detecting the relations between meteorological elements and alpha and beta activity concentration at Al-Tuwaitha site, Baghdad

Key words: alpha activity, beta activity, airborne radioactivity, meteorology, Al-Tuwaitha site

Introduction

Al-Tuwaitha site is one of the nuclear places existing in Baghdad province, Iraq that was seriously damaged during the Gulf War 1991. This facility as the source of radioactive rays has a potentially significant amounts of wastes which cause radiological contamination of the site and surrounding areas around it by dispersing radionuclides attached on aerosols and water vapors (Interational Atomic Energy Agency [IAEA], 2012). Such contamination has adverse effects on human health, plants and animals especially when decaying radioactive materials which emit energetic charged particles such as alpha, beta, gamma or neutron radiation according to the radioisotope existing (Reiman, 2002; Shahbazi-Gahrouei, Gholami & Setayandeh, 2013; Nassif, Wahab, Al-Jiboori & Ali, 2020). Thus, their concentrations in surface air is mainly affected by emissions fine particles resulting from the variations of atmospheric conditions: strong solar insulation, high wind speed, wind direction changes and air stability.

In recent decade and based on the average bulk mass or surface concentration, some local and international studies were assessed the radioactive level at Al--Tuwaitha site by taking some samples for different places from its soil, plant and even air (Jarjies, Abbas, Fernandes, Wong & Coates, 2013; Mansour, Al-Bakhat & Karkosh, 2017; Salih et al., 2018; Nassif et al., 2020). In present research, we reanalyze alpha and beta activity concentration measurements published in the reference of (Salih et al., 2018) to explore the relationships between these concentrations and meteorological

elements. Airborne radionuclides have high energy leading to large localized radiation doses inhaled the body whereas meteorology has significant effect in dispersion and transport of pollutants (Lazaridis, 2011; Al-Jiboori, 2015).

There was a few studies that investigated the quantitative relations between meteorological parameters and alpha and beta activity concentrations. For example, Dueñas, Fernández, Liger and Carretero (1999), Arkian, Salahinejad, Bidokhti and Meshkatee (2008), and Salih et al. (2018) showed that maximum concentration of alpha and beta were found during spring and summer seasons. Also these references illustrated that these concentrations were weakly inversely proportional with air temperature and wind speed while they were proportional with relative humidity. In this work, we focus to (1) study the variations of alpha and beta activity concentration with six meteorological elements: air temperature, solar radiation, wind speed, wind direction, air pressure, and relative humidity; (2) find the correlation coefficient among them with *p*-value; and (3) calculate air stability classes with their frequencies and then examine their relations with the concentrations above.

Description of Al-Tuwaitha site

At 18 km southeast of Baghdad, Al-Tuwaitha site is located as the foundation of Iraq's nuclear research center from 1967 until its final damage in 2003. It covers an area 1.3 km^2 and away about 1 km east of the Tigris river (Fig. 1). It is extended with latitude 33°10′ – 33°15′ N, longitude 44°29′ – 44°35′ E and 32 m above mean sea level.

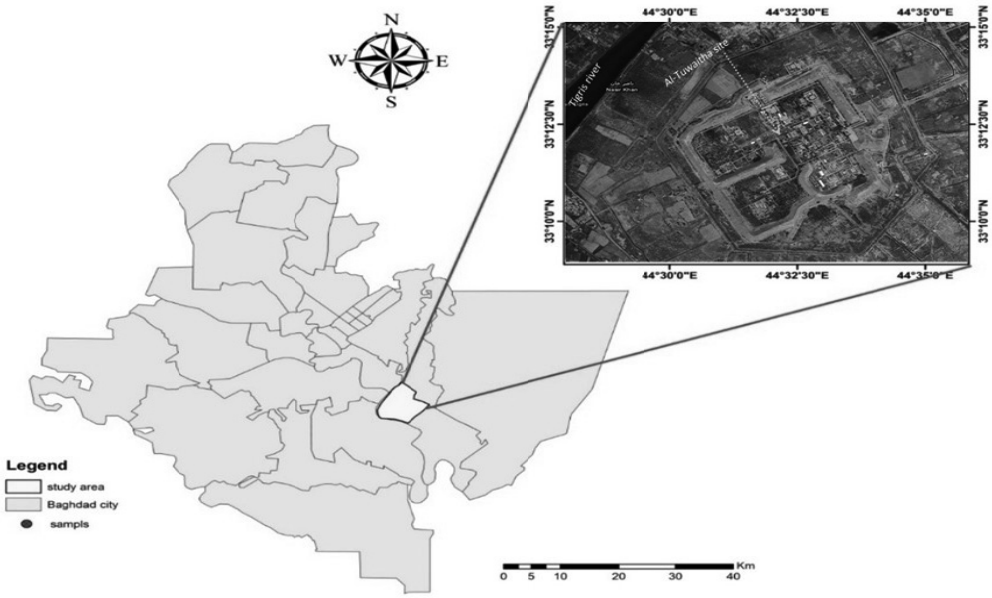

FIGURE 1. Map of Baghdad city including study area with its aerial photograph

There are large earthen beams that were placed around the key facilities to fortify them. In 1991, the Al-Tuwaitha had 90 buildings dedicated to nuclear fuel fabrication, radiochemistry, uranium enrichment, radioactive waste treatment and biological research (Zaboon, Al Obaidy & Al Sharaa, 2013). The famous reactors were Osiraq, 5-MW IRT--5000, 40-MW Tammuz-1 and 500-KW Tammuz-2, which suffered substantial physical damage since 1991 and then displayed to secret operations combined with the bombing of nuclear facilities and subsequent looting by dwellers. Therefore, Al-Tuwaitha and nearby villages suffered widespread radioactive contamination (Chesser, Rodgers, Bondarkov, Shubber & Philips, 2009).

Material and methods

Two different datasets were used to execute this study: (1) counting alpha and beta rates and (2) meteorological observations, which were measured at the same time at 50 places within and outside the Al-Tuwaitha site for worked 39 days with date starting from 28 December 2016 to 13 April 2017. The observation time was at daytime from 09:20 am and 12:20 am and for approximately 1 h. Airborne dust samples and drawn from ambient air at flow rate 10–15 $m^3 \cdot h^{-1}$ were daily collected in a glass-fiber filters with diameter 5.5 cm. To represent the radioactive contaminated air, the device was put 20 m far from the buildings with collection efficiency 99%. Later, using Ludlum 3030P scaler alpha/beta sample counter, the air filters analyzed to measure simultaneous alpha and beta particles. The structure and feature of this instrument can be found in more detail in reference (Ludlum Measurements, 2017). The device was daily calibrated and checked the quality control before using it to ensure the validation of measurements.

The activity concentration of radionuclides (alpha and beta) is the activity of these in a radioactive substance in an air divided by the volume of the air. The change in counting and background rates represents the number of spontaneous nuclear transformations taking place in the relevant number of radionuclides in a time interval (Δt) divided by this time.

$$AAC/BAC = \frac{\text{counting rate (alpha/beta)} - \text{background rate (alpha/beta)}}{\Delta t \cdot V \cdot E_f} \quad (1)$$

where E_f is the filter efficiency. Thus the unit of activity concentration in SI system is the Becquered per cubic meter [$Bq \cdot m^{-3}$], whereas 1 Becquered equals 1 disintegration per 1 second. Becquered is a unit to express strength of radioactivity.

During the period of this study, meteorological parameters such as wind speed, wind direction, air pressure, and relative humidity were also recorded by portable devices at Al-Tuwaitha site, while only solar radiation measurements was supplied by the nearby automatic weather station located at Mustansiriyah University, which is far from the site with 21 km. The latter parameter is required in calculating air stability, which was determined using modified Pasquill–Turner (Table 1).

TABLE 1. Modified Pasquill–Turner stability classes

Wind speed [m·s^{-1}]	Daytime solar radiation [W·m^{-2}]			Overcast
	> 600	300–600	< 300	
< 2	A	A–B	B	C
2–3	A–B	B	C	C
3–5	B	B–C	C	C
5–6	C	C–D	D	D
> 6	C	D	D	D

A – very unstable; B – moderate unstable; C – slight unstable; D – neutral.

Statistical analysis

First, sometimes, at the values for air pressure and wind speed, there were several different values of alpha and beta activity concentration. Thus, means were calculated with standard deviation – represent the dispersion around the mean values – plotted as vertical lines in some figures of this study. Second to identify the variations of these concentration affected by the meteorological parameters, linear and non-linear fitting lines were performed using Origin software (version 9.3). Other statistical analyses including maximum and minimum values, frequencies, wind rose, Pearson's correlation coefficients (R), and a significant level represented with p-value less than 0.05 were also computed.

Results and discussion

Daily alpha/beta activity concentrations were analyzed to derive the statistical relationships with meteorological elements measured at the same time. Table 2 displays their arithmetic means, standard deviation (*SD*), minimum and maximum values. *AAC* values were ranged from 0.42 to 4.18 Bq·m^{-3} and have a mean of 1.78 Bq·m^{-3} with *SD* = = 0.84 Bq·m^{-3}. While *BAC* values that are always larger than *AAC* range from 0.93 to

TABLE 2. Mean values for meteorological variables with their SD, minimum and maximum

Meteorological variable	Mean	*SD*	Minimum	Maximum
Alpha activity concentration [Bq·m^{-3}]	1.78	0.84	0.42	4.18
Beta activity concentration [Bq·m^{-3}]	3.9	1.8	0.93	9.21
Air temperature [°C]	20.8	4.1	15	30
Wind speed [m·s^{-1}]	4.8	1.96	1	7.1
Relative humidity [%]	52.5	17.7	21	83
Air pressure [mmHg]	761.8	3.61	754.5	769.6
Solar radiation [W·m^{-2}]	417.4	198.6	0	700

9.21 Bq·m^{-3} with an average 3.9 Bq·m^{-3} and SD = 1.84 Bq·m^{-3}. The above values in this study are approximately close to the measurements recorded at the air of university of Malaga, Spain which characterize with warm climate with little rain (Dueñas et al., 1999).

During the study period, there were also clear variations in meteorological elements. This can be verified in terms of their ranges, air temperature: 15–30°C, wind speed: 1–7.1 m·s^{-1}, relative humidity: 21–83%, air pressure: 754–769.6 mmHg and solar radiation: 0–700 W·m^{-2}. The means of these variables are 20.8°C, 4.8 m·s^{-1}, 52.5%, 761.8 mmHg and 417.8 W·m^{-2}, respectively.

Correlation coefficients between *AAC*/*BAC* and meteorological elements

To identify which meteorological element is effected on the fluctuations of *AAC* and *BAC*, thus we present the *AAC* and *BAC* measurements on Y-axis and meteorological observations on X-axis as shown in Figures 2–6. In general, there was high scatter in *BAC* values comparing to those of *AAC*. Also, according to observed behavior with respect to each figure, we could make the best fitting lines, solid and dashed lines plotted for *AAC* and *BAC*, respectively. They were obeyed to mathematical relations which have empirical constants deriving from the field measurements for all parameters in this study. We first calculate correlation coefficients which reported in Table 3 with p-value results.

Figure 2 presents *AAC* and *BAC* measurements against air temperature. The decreasing behavior for these concentrations is clear when increasing temperature, i.e. there has inverse relation between *AAC*/*BAC* and air temperature (T_a). Activity concentration of radionuclides (alpha and beta) could be expressed by the following equations:

$$AAC = 6.9 - 0.37 \cdot T + 0.006 \cdot T^2 \qquad (2)$$

$$BAC = 15.4 - 0.84 \cdot T + 0.014 \cdot T^2 \qquad (3)$$

This decreasing was also confirmed negative moderate correlation coefficient (R = –0.57 with p = 0.00002) for the relation between *AAC* and temperature, while R = –0.58 with p = 0.00001 when correlated with *BAC*.

TABLE 3. Correlation coefficients (R) and significance p-values for relation between *AAC*/*BAC* and meteorological variables

Variable	*AAC*		*BAC*	
	R	*p*	*R*	*p*
Air temperature	–0.57	0.000016	–0.58	0.00001
Wind speed	–0.72	0.0022	–0.76	0.001
Relative humidity	0.21	0.15	0.22	0.13
Air pressure	0.58	0.00083	0.58	0.00075
Solar radiation	–0.33	0.03	–0.34	0.025

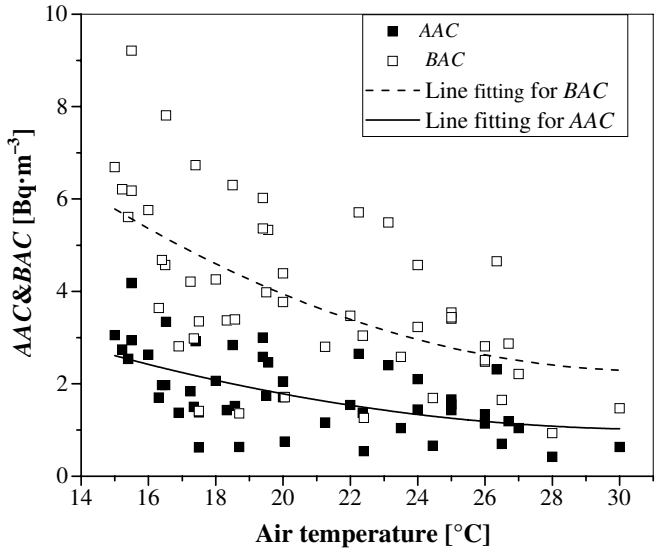

FIGURE 2. Variation of *AAC* and *BAC* with air temperature

The same behavior was also found when plotting *AAC*/*BAC* values with wind speeds (Fig. 3). The best fitting line passing through these data is described by the the following expressions:

$$AAC = 4.02 - 0.88 \cdot U + 0.007 \cdot U^2 \quad (4)$$

$$BAC = 10.06 - 2.22 \cdot U + 0.17 \cdot U^2 \quad (5)$$

The good inverse correlation coefficients between *AAC*/*BAC* values and wind speed were observed as shown in Table 3 where $R = -0.72$ with $p = 0.0022$ for *AAC* and wind and $R = -0.76$ with $p = 0.001$ for *BAC* and wind.

Because high scatter for *AAC*/*BAC* measurements with relative humidity, correlation coefficients were positive weak $R = 0.21$ and 0.13, respectively with $p > 0.05$. Although high scatter and weak correlation coefficient, the relations between them appear to have linear behavior which obeys to linear regression equations:

$$AAC = 1.24 + 0.88 \cdot RH\,\% \quad (6)$$

$$BAC = 2.71 + 0.02 \cdot RH\,\% \quad (7)$$

The values of *AAC* and *BAC* show a linear relation with air pressure (*P*) as illustrated in Figure 5, in which the plotted solid and dashed lines drawn are fitting for these values for these values followed by linear regression equations:

$$AAC = -75 + 0.1 \cdot P \quad (8)$$

$$BAC = -186.7 + 0.25 \cdot P \quad (9)$$

As stated in Table 3, both *AAC* and *BAC* values have the same moderate positive correlation coefficient with air pressure ($R = 0.58$ with $p = 0.0008$).

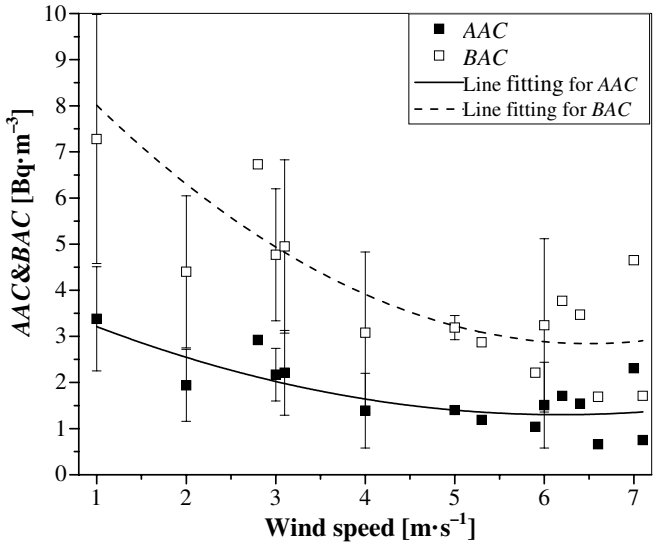

FIGURE 3. Variation of *AAC* and *BAC* with wind speed

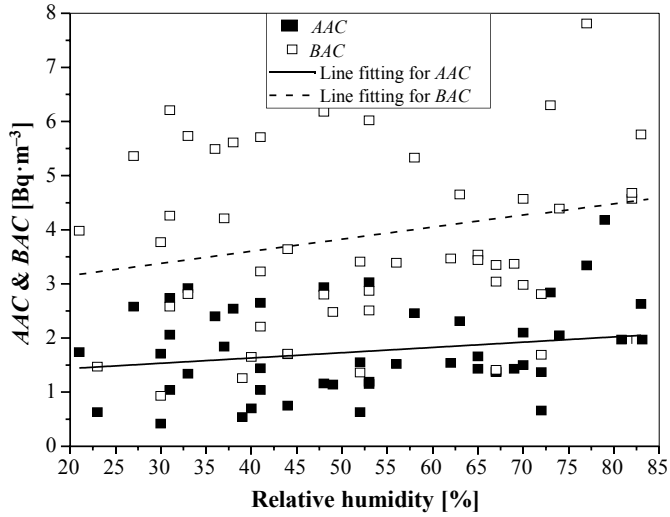

FIGURE 4. Variation of *AAC* and *BAC* with relative humidity

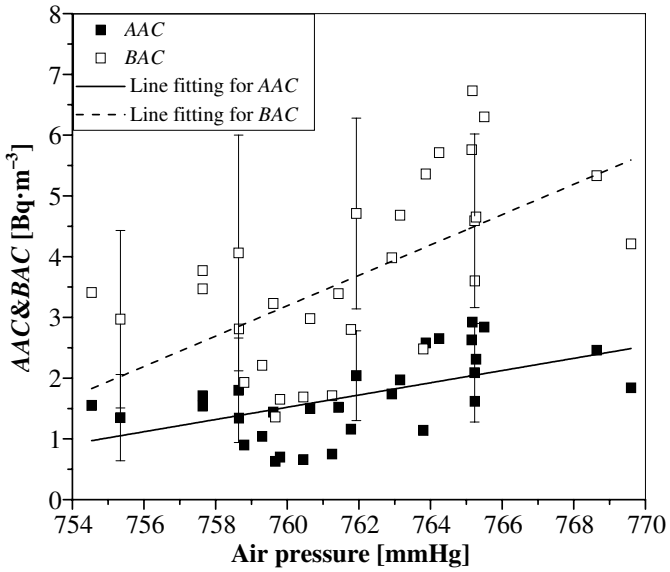

FIGURE 5. Variation of *AAC* and *BAC* with air pressure

Lastly, when solar radiation (*SR*) values were less than 300 W·m^{-2}, the *AAC* and *BAC* values have constant behavior and then continuously decrease when *SR* > 300 W·m^{-2} as shown in Figure 6. These non-linear behaviors could be represented by the the following expressions:

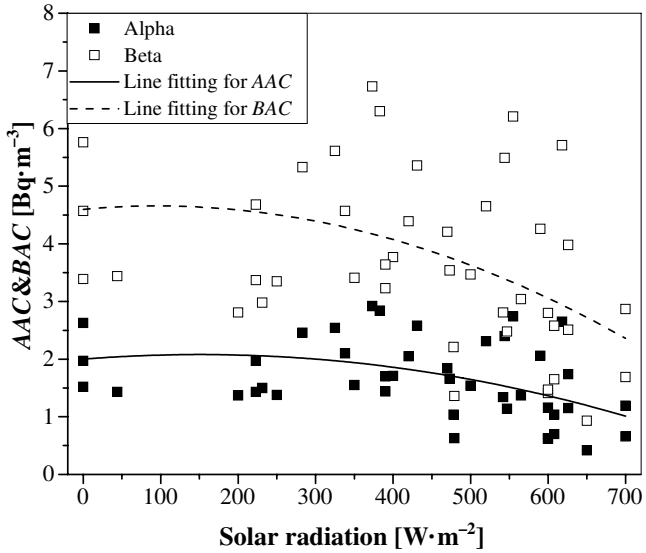

FIGURE 6. Variation of *AAC* and *BAC* with solar radiation

$$AAC = 4.02 - 0.88 \cdot SR + 0.07 \cdot SR^2 \quad (10)$$

$$BAC = 10.06 - 2.22 \cdot SR + 0.17 \cdot SR^2 \quad (11)$$

The overall correlation coefficients for both *AAC* and *BAC* with solar radiation data were negative weak, $R = -0.33$ with $p = 0.025$.

Effect of wind direction on *AAC*/*BAC*

To study the potential effect of daily wind direction, we presented wind rose shown in Figure 7, in which the main direction is at northwest that represents prevailing wind direction with frequency ratio (46%) during the study period. The other prevailing direction with ratio 23% is north. These two directions roughly forms 70% of total number of measurements.

Through both prevailing directions, the mean concentration activity for *AAC* and *BAC* with *SD* was calculated. The frequency with its percentage and mean with *SD* were reported in Table 4. When the northwesterly wind dominates the mean *AAC* and *BAC* values arise as high

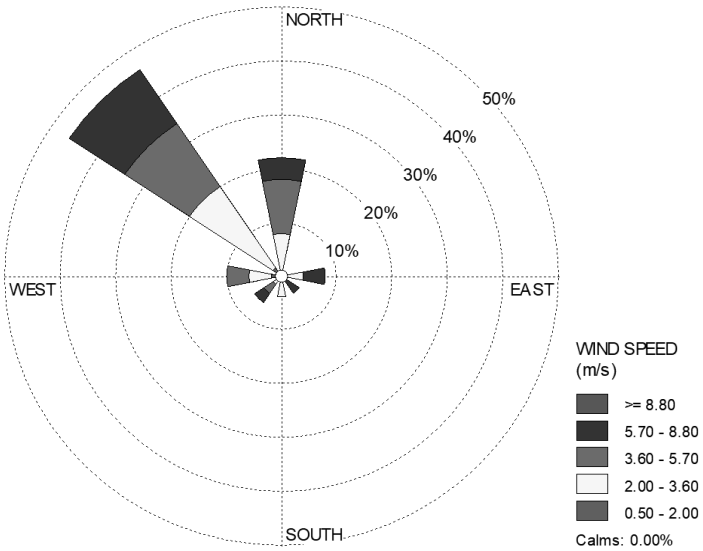

FIGURE 7. Wind rose at Al-Tuwaitha site during the studied period

TABLE 4. Frequencies of *AAC* and *BAC* and their means for prevailing wind directions in this study

Wind direction	Number of frequencies	Activity concentration	Mean [Bq·m^{-3}]	*SD*	Minimum	Maximum
NW	23	*AAC*	2.05	0.88	0.6	4.18
		BAC	4.52	1.92	1.41	9.21
N	10	*AAC*	1.4	0.73	0.63	2.74
		BAC	3.15	1.63	1.36	6.21

as from north. Although minimum values for both *AAC* and *BAC* are approximately similar for both above directions, the maximum *AAC* and *BAC* at northwest is higher than those at north.

Effect of air stability on *AAC*/*BAC*

According to daily data for wind speed and solar radiation, the air stability classes have been determined using Table 1. All of observations (50 runs) were mostly found to be in two major classifications that are unstable (37 runs) and neutral (13 runs) conditions as shown in Table 5. Here, only two runs with ratio 4% at class A cannot be reliable, so they were not discussed. Most runs were in moderate unstable classes (23 runs with 46%), slight unstable classes (12 runs with 24%). Meanwhile only 13 runs with ratio 26% were obtained under neutral conditions class D.

The mean values for both *AAC* and *BAC* at each class were calculated with their standard deviations, as reported also in Table 5. The large values for *AAC* (> 2 Bq·m^{-3}) were found at classes B and B–C and also the same result was for ABC but with a large value (~ 4.5 Bq·m^{-3}). At class C, the smallest values for both *AAC* and *BAC* were 1.27 ±0.7 Bq·m^{-3} and 2.83 ±1.5 Bq·m^{-3}. As an overall result, mean *AAC* in stable air has a value of 1.67 Bq·m^{-3} which are slightly less than 1.71 Bq·m^{-3} for neutral air. This result was changed for ABC, where its mean value is 3.78 Bq·m^{-3} in unstable air that is slightly larger than the value 3.71 Bq·m^{-3} in neutral conditions.

Conclusions

This study detects the effects of daily meteorological variables of air temperature, wind speed and its direction, air pressure, relative humidity, and solar radiation on gross alpha and beta activity concentration at Al-Tuwaitha nuclear site for period from 28 January 2016 to 13 April 2017. In general, although *AAC* values are less than *BAC*, they have often the same behavior over all ranges of these variables. Both wind speed, temperature, and solar radiation negatively correlated with *AAC* (R = –0.72, –0.58 and –0.33) and *BAC* (R = –0.76, –0.58, –0.33, respectively). Meanwhile, air pressure and relative humidity were positively correlated with *AAC* (R = 0.58 and 0.21) and *BAC* (R = 0.58 and 0.22). All these relations were found to obey nonlinear regression equations, except for *AAC*/*BAC*

TABLE 5. Frequencies of stability classes and mean values of *AAC* and *BAC*

Stability classes	Frequency	Ratio [%]	*AAC* [Bq·m^{-3}]		*BAC* [Bq·m^{-3}]	
			mean	*SD*	mean	*SD*
A	2	4	1.39	0.49	3.28	0.99
B	17	34	2.1	0.93	4.71	2.09
B–C	6	12	1.92	1.0	4.32	2.28
C	12	24	1.27	0.72	2.83	1.57
D	13	26	1.71	0.63	3.71	1.2

with air pressure and relative humidity, which follow the linear equation. Lastly, wind direction has significant effect on *AAC* and *BAC* whereas their mean values were found to be large in prevailing wind (northwest) compared to other direction (north).

Acknowledgements

The authors are grateful to Mustansiriyah University for acceptance this work. Also many thanks are to anonymous reviewers for constructive comments for improvement of the paper.

References

Al-Jiboori, M.H. (2015). *Atmospheric pollution*. Baghdad: Al-Semaa Press.

Arkian, F., Salahinejad, M., Bidokhti, A.A. & Meshkatee, A. (2008). Analysis of gross alpha, gross beta activities and beryllium-7 concentrations in surface air: their variations and statistical prediction model. *Environmental Monitoring and Assessment*, *140*(1), 325-330.

Chesser, R.K., Rodgers, B.E., Bondarkov, M., Shubber, E. & Phillips, C.J. (2009). Piecing together Iraq's nuclear legacy. *Bulletin of the Atomic Scientists*, *65*(3), 19-33.

Dueñas, C., Fernández, M.C., Liger, E. & Carretero, J. (1999). Gross alpha, gross beta activities and 7 Be concentrations in surface air: analysis of their variations and prediction model. *Atmospheric Environment*, *33*(22), 3705-3715.

International Atomic Energy Agency [IAEA] (2012). *Terminology used in nuclear safety and radiation protection*. Vienna: International Atomic Energy Agency.

Jarjies, A., Abbas, M., Fernandes, H.M., Wong, M. & Coates, R. (2013). Prioritization methodology for the decommissioning of nuclear facilities: a study case on the Iraq former nuclear complex. *Journal of Environmental Radioactivity*, *119*, 70-78.

Lazaridis, M. (2011). *First principles of meteorology and air pollution*. Berlin: Springer.

Ludlum Measurements (2017, June). *Ludlum Model 3030P alpha-beta sample counter. Technical manual* (software version 1.6.4). Retrieved from: https://ludlums.com/images/product_manuals/M3030P.pdf

Mansour, H.L., Al-Bakhat, Y.M. & Karkosh, H.N. (2017). Measurement of radioactivity levels and assessment of radiation hazards for plants species grown at scrap yard (B) at Al-Tuwaitha nuclear site (Iraq). *Nuclear*, *2*(4), 94-98.

Nassif, W.G., Wahab, B.I., Al-Jiboori, M.H. & Ali, A.B. (2020). Temporal and spatial analysis of alpha and beta activity concentration at Al-Tuwaitha Site, Baghdad. *Nature Environment and Pollution Technology*, *19*(4), 1499-1505.

Reiman, R. (2002). *Introduction to radiation physcics, quantites and units*. Durham (NC, USA): Duke University Medical Center Against Radiation.

Salih, N.A.M., Al-Bakhat, Y.M.Z., Abd ulmajeed Al-Rahmani, A., Murbat, O.M., Ameen, N.H. & Majed, N.A. (2018). Assessment of radiological air contamination for selected places at Al-Tawaitha nuclear site during winter and spring. *Baghdad Science Journal*, *15*(3), 278-286.

Shahbazi-Gahrouei, D., Gholami, M. & Setayandeh, S. (2013). A review on natural background radiation. *Advanced Biomedical Research*, *2*(3), 1-3.

Zaboon, A.R.T., Al Obaidy, A.H.M.J. & Al Sharaa, H.M. (2013). Radioactive doses contamination in Al-Tuwaitha nuclear site, using GIS techniques. *Engineering & Technology Journal*, *31*, 1612-1615.

Summary

Detecting the relations between meteorological elements and alpha and beta activity concentration at Al-Tuwaitha site, Baghdad. In this study, 50 samples of air particulates collected from different places in- and outside the Al-Tuwaitha nuclear site, south of Baghdad were used to measure daily

gross alpha and beta activity concentrations (*AAC* and *BAC*) for the period from 28 January 2015 to 13 April 2017. At the same time, several meteorological factors such as air temperature, wind speed, wind direction, air pressure, relative humidity, and solar radiation, were also measured. Air stability classes were also derived from wind speed and solar radiation. *AAC*/*BAC* variations in the surface air layer were discussed in relation to these factors. The results show that there are inverse relations between *AAC*/*BAC* and wind speed and temperature, linear relations between *AAC*/*ABC* and air pressure and weak relations between *AAC*/*BAC* and relative humidity and solar radiation. Lastly, *AAC*/*BAC* measurements in unstable air are as large as in neutral air.

Authors' address:
Salwa S. Naif
Mustansiriyah University
College of Science
Atmospheric Sciences Department
e-mail: naif.salwa2016@gmail.com

Thoalfaqar Al-Rbayee
Mustansiriyah University
College of Science
Atmospheric Sciences Department
e-mail: thoalfaqarfalehalrubayee@gmail.com

Monim H. Al-Jiboori – corresponding author
Mustansiriyah University
College of Science
Atmospheric Sciences Department
e-mail: mhaljiboori@gmail.com

Scientific Review – Engineering and Environmental Sciences (2021), 30 (3), 400–410
Sci. Rev. Eng. Env. Sci. (2021), 30 (3)
Przegląd Naukowy – Inżynieria i Kształtowanie Środowiska (2021), 30 (3), 400–410
Prz. Nauk. Inż. Kszt. Środ. (2021), 30 (3)
http://iks.pn.sggw.pl
DOI 10.22630/PNIKS.2021.30.3.34

Sara Ali MUTER, Jasim H. KADHUM, Ahmed S. HASSAN

Mustansiriyah University, College of Science

Approaching of May maximum surface air temperature to characteristic summer season for Baghdad city

Key words: maximum air temperature, summer season, May, Baghdad

Introduction

Surface air temperature is change related to change for seasons. These changes happen in the seasons themselves, that is winter became warmer, spring becomes early and leaves quickly, and summer becomes longer and hotter. According to meteorologist research for many countries, these changes were used in reference to atmospheric variability on timescale longer than the two weeks limit of most deterministic atmospheric predictability (Bilal, Kais & Enas, 2013). That also point to climate variability, which are the variations in the mean state and other statistics of the climate spatially and temporally, usually beyond individual weather statistics. This term "climate variability" cannot deviations of climatic statistics over a given period of time (e.g. a month, season or year), some scientist are of the opinion that this period can transcend to decades (30 years). Climate variability assessed by these deviations, which are usually termed anomalies. The variability may be due to natural internal processes within the climate system (internal variability), or to variations in natural or anthropogenic external factors (external variability), but climate variability is more affiliated to the internal variability unlike climate change (Zeki, 2017). One of the climatic elements that sensitive to climate variability is air temperature and that play significant role on the human life style. Beside that it is evidence of changing in the climate system because of the possibility of calculation this variable for both cases; temporal and spatial. Air temperature interacts with other climate elements such as atmospheric pressure, wind, evaporation, and relative humidity (Muter, 2014).

Attributes of the seasons may vary by location, but there are still broad definitions that cross most of the boundaries. The timing and characteristics of the seasons depends upon the location on Earth. Summer, season extending from the summer solstice to the autumnal equinox, is one of the four Earth's seasons that goes after spring and foreshadows autumn. In winter, days become warm than before hot and really long, while nights in this season are the shortest. Sun shines so bright and most active, it means that everything in the nature gets a lot of energy form the sun, to support life, breeding and feeding. Summer, long days, and become hotter creates a special lifelong conditions for animals and plants activities (Chitu, Giosanu & Matescu, 2015). Northern hemisphere is a part of the Earth that is located north to equator. Summer is the warmest season of the year occurring between spring and autumn and constituting June, July, and August. The hottest month is July, because in this time Earth gets more straight sun lights (Wang, Li & Li, 2019).

Most previous work has focused on the spring-to-summer transition, this transition period is distinct from the winter and summer seasons and warrants further investigation. An analysis of this transition period is also expected to improve our understanding of conditions in winter and summer. Many studies have explored anomalies in temperature especially in summer. These studies have greatly enhanced our understanding of surface air temperature anomalies during summer. Recently study found out the mean air temperature increased for all months and for four seasons because of global climate change, while disagree with opinion that refer to overlap in month or season. The maximum air temperature were increased more than 1°C for spring and summer, while less than 1°C for winter and autumn middle and southern Iraq (Hassan & Alhashimi, 2018). The monthly air temperatures

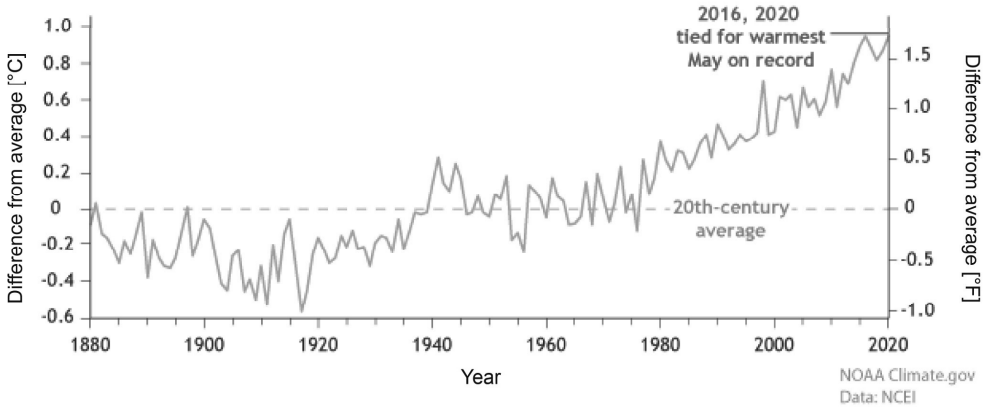

FIGURE 1. The global temperature differences from average for all Mays from 1895–2020. May 2020 tied for the warmest May on record with May 2016 (National Centers for Environmental Information NOAA National Centers for Environmental Information [NCEI], 2020)

(maximum and minimum) recorded high increased of temperature which happened in summer, but with less force for transitional months nearby (May and September), so that May is approaching summer features for maximum temperatures (Fig. 1), and September is approaching summer features but for minimum temperatures (Muter, 2014).

The estimation of increased air temperature in the center Baghdad city and rural side beside effect of increasing population density that there was a strong tendency for a temperature increasing during July and October (Ahmed & Hassan, 2018). Daily maximum air temperature studied for long time (2006–2017) that found 70 extreme events happen 60 of them happen in Basra. The extreme events in the end studied period were four more time than beginning studies. That found evidence for summer extended to September more than May whereas both of these months have summer characteristics (Vicente-Serrano et al., 2018). Trends of maximum air temperature exhibited a clear elevation-warming dependency, with the strongest warming recorded at highly elevated sites. For mean air temperature trends, there are no clear spatial and temporal seasonal differences across Peru (Liu, Yin, Shao & Qin, 2006). Analysis of mean summer maximum temperature changes in frequency and intensity of daily temperature extreme temperature variability and trends over Romania which was found of maximum temperature rate 21.0% per decade. It was noted that the level of statistical significance of maximum and minimum temperature linear trends per decade was low during winter, spring and autumn. But this level of significance was very high for June, July and August months (Chitu et al. 2015).

The length of the season has been increased about 17 days during the 43-year study period. The monthly record-setting for cold events were found in the earlier part of the study period, while the warm events occurred mostly in the later half, especially since the 1990s (Wu & He, 2017). The anomalies in the accelerated transition years display a relatively quick month-to-month change. This suggests a plausible contribution of inter-seasonal variations to the accelerated transitions (Zarenistanak, Dhorde & Kripalani, 2014). Temperature tendencies indicated positive change in temperature, particularly in summer and spring over most of the stations. Moreover, temperature increment in winter is less in comparison with other seasons. Increasing tendencies in T_{min} were more than T_{max} in all the seasons. Therefore, the increase in annual and seasonal TM can be attributed to higher increase in T_{min}. The results showed that most of the positive significant mutation points began in 1990s in the study area (World Atlas, 2021).

These work focus on provide a comprehensive picture of spring-to-summer climate variability for partially areas, and then do an investigation of the factors and processes involved in anomalies during the transition season is warranted. This study, describe monthly air temperatures for Baghdad's hot season using statistical method for maximum temperatures and understand the behavior of begin early summer and check changes in the length and the strength of Baghdad's hot season between 1970 and 2017, especially the changes that change in May.

Data and methods

The study area is Iraq, specifically Baghdad, where Iraq geographically located in the range of sub-tropical displays in the northern hemisphere between the two latitudes 29.5–37.5 north of the equator and longitudes 38.45–48.45 east of the Greenwich line. Baghdad is the capital of the Republic of Iraq, shown in Figure 2. It is one of its largest cities and the second largest city in the Arab world and the second largest city in Western Asia. It is also considered the economic and administrative center in the country. Baghdad occupies a geographical position at the latitude 33.3 north of the equator and the longitude 44.4 east of the Greenwich line, this is from a spatial point of view. As for time, the study was determined by the duration of 1970–2017 (Iraqi Meteorological Organization and Seismology [IMOS], 2017).

There is in Baghdad governorate a monitoring station located in Baghdad International Airport, established since the airport's foundation and holds the global code 650 within the codes registered in the World Meteorological Organization where it works on surface monitoring, called Iraqi Meteorological Organization and Seismology (IMOS). Using the monthly data for maximum temperatures that adopted from for 47 years from 1970 to 2017 for Baghdad city. The study period was divided into two periods, the first

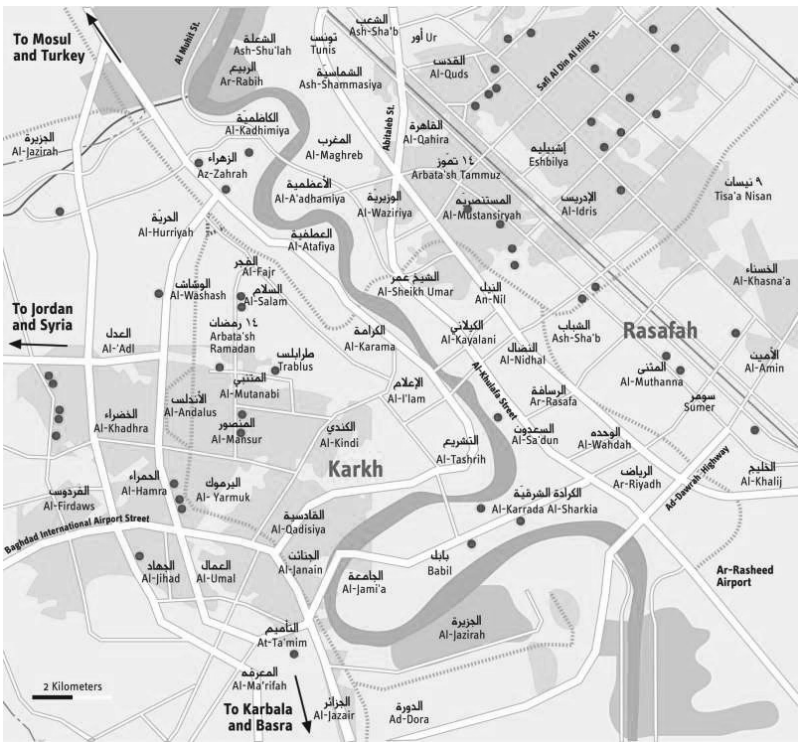

FIGURE 2. Map of the study area (Baghdad governorate) (IMOS, 2017)

period from 1970–1991 and the second period from 1992–2017. Thirty years of data is long enough to calculate an average that is not influenced by year-to-year variability. The reason for choosing is the availability of its data and a continuation of previous research on this topic that touched on the overlap of the seasons, knowing that there are research studies of temperatures and their general direction.

Results and discussion

Objective study of observation seasonal variation to understand changes that happen in monthly air temperature with increasing daily length related with latitude more than balancing 108 the increasing solar zenith angle so that saturation increases slightly with latitude. In the case for specific region (Baghdad), this study focused on the variation for maximum air temperature in May during approaching summer properties for limit period (1970–2017). The study period was divided into two periods: the first begin in 1970, while the 1991 was the end year, and the second (1992–2017).

Due to climatic changes, all months of the year will increase in temperature, but this increase depends on two main points, which are climate variation and climate changes. When we compare the distinguished cases (the increase over the average) for the month of May and convert them into ratios compared to the months (June and July), the result indicated that the rate of increase for the month of May was 54%, while the rate of increase for the months of June and July was 50% and 48%, respectively. We conclude from this that May is qualified to acquire the characteristics of the summer season due to this high percentage. In addition, there should be a difference in the rates, since May approaches the characteristics of summer season, June of the beginning of the season and July the climax of the summer season.

Temperature tendencies indicated positive change in temperature, particularly in summer. Figure 3 shown time series of variation $T_{\max}$ in May, where

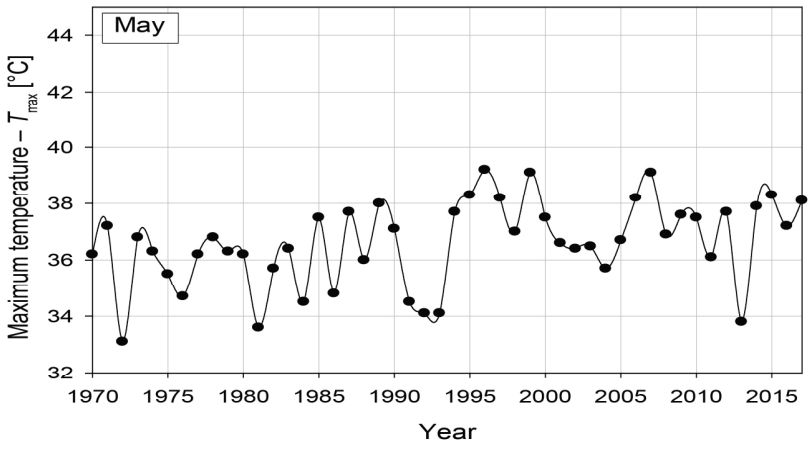

FIGURE 3. Time series for temperature maximum values in May during 1970–2017 for Baghdad city

minimum T_{max} was 33°C in 1972, and high value was 39°C in 2007; that is, the different for transfer season for May (6°C). Therefore, this split came to two periods from this point and because of the T_{max}. Below 38°C in the first period, while in the second more than seven years (1995, 1996, 1997, 1999, 2005, 2006, and 2015) were above 38°C. These results show different inter-seasonal variation between these two periods, meaning that each period has its own inter-seasonal variation. The pattern of T_{max} for each period was different too, in the first period more regular fluctuation than second period that represent each three years maximum peak.

June represented first month for summer season, and the minimum value of T_{max} was 39°C, that is the maximum temperature for May as shown in Figure 4, where the maximum of T_{max} was 44°C. The inter-seasonal variation for this month was about 6°C, although the second period has more wide variance than first period, but less than May, and this result confirms the trend in the previous paragraph, which was split the period study into two parts.

The T_{max} for July behavior similar to June, which represent summer's characteristics. The minimum T_{max} was 42°C that the same temperature for maximum temperature for June, while the maximum temperature was 48°C as shown in Figure 5. The inter-seasonal variation for this month was about 6°C. The maximum peak of T_{max} for first period was less than 46°C, while in the second period five years was above 46°C (1996, 2000, 2012, 2015, and 2017). This refer to general trends tends to increased T_{max}.

The results that carried out when find the difference between T_{max} for June––May are shown in Figure 6. The first period characteristic of the summer season was the large number of fluctuations with same wave cycle, while the second periods have less fluctuation with short amplitude. Generally the high difference for T_{max} (June–May) was 8°C.

The difference between July and May is shown in Figure 7. The fluctua-

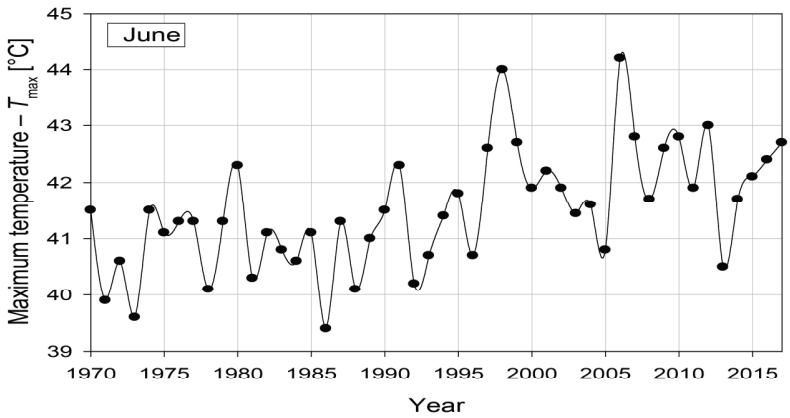

FIGURE 4. Time series for temperature maximum values in June during 1970–2017 for Baghdad city

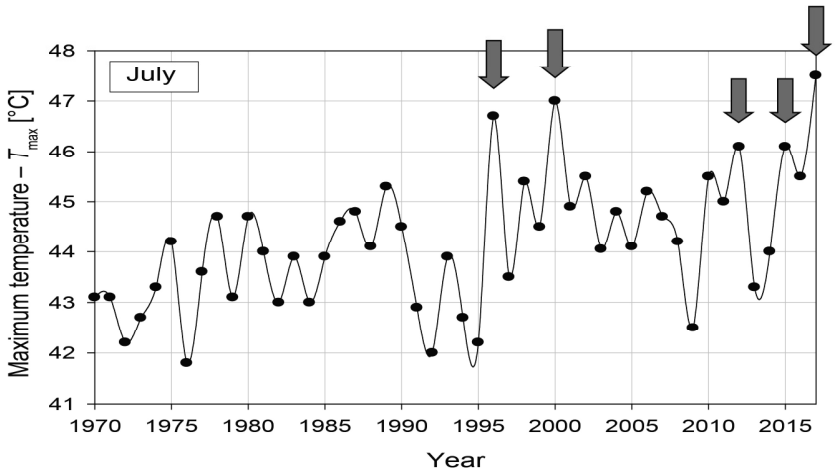

FIGURE 5. Time series for temperature maximum values in July during 1970–2017 for Baghdad city

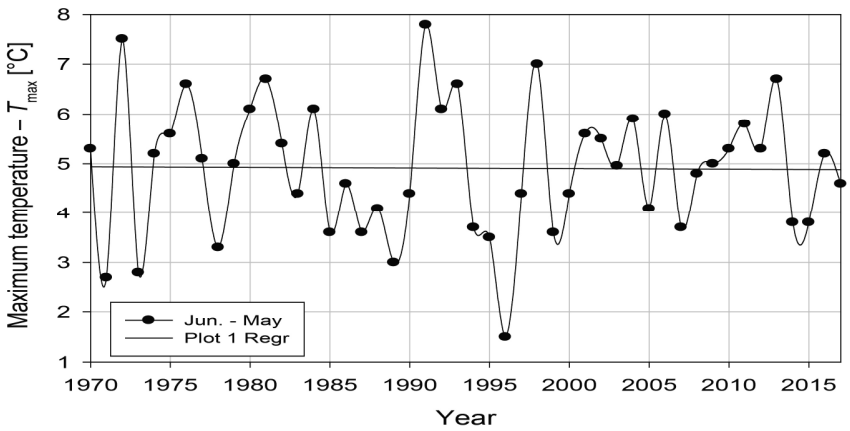

FIGURE 6. Time series for differences between temperature maximum values in June–May during 1970–2017 for Baghdad city

tion was irregular, and the variance was about 2°C than average with short amplitude except a few years (i.e. 1995) to represented one of the most important properties of summer, with high variance was about 6°C.

When find the difference between two months in the same season as noted in Figure 8, the variance in the begging was 1–2°C then reach to 5°C in 1995 that were compatible with previous cases, so that May was approaching to summer.

When compare between summer's months with May in the dataset that draw in Figures 6, 7 and 8. These three cases for difference of T_{max}. The significant increase appear in the T_{max} during May and summer months (June, July, and August) during the study period as follows

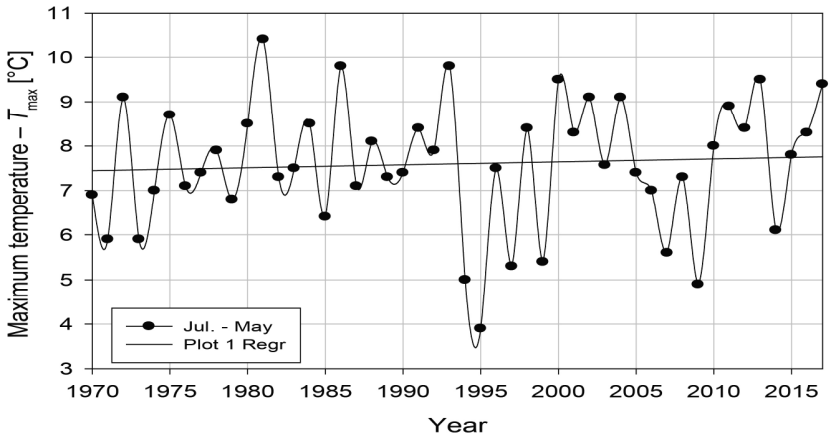

FIGURE 7. Time series for differences between temperature maximum values in July–May during 1970–2017 for Baghdad city

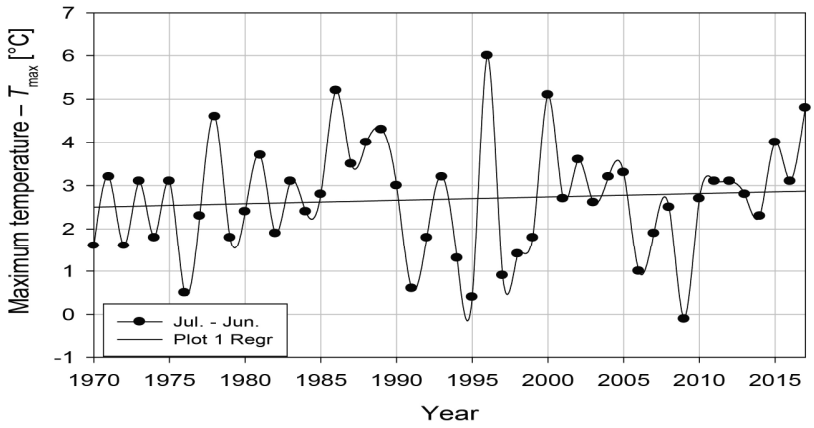

FIGURE 8. Time series for differences between temperature maximum values in July–June during 1970–2017 for Baghdad city

(1.9 for May, 1.2 for June, 4.4 for July, 4.9 for August). There is also a significant T_{max} for Baghdad with similar behavior of T_{max} in May to June and July during the second period of the study period (1992–2017), unlike the first period (1970–1991). Two phases in second period found out, the positive phase happened in 1995, 1999, and 2006, four cases were negative (1992, 2004, 2013, and 2016), while a few cases recorded in first period.

For the purpose of comparing the change for the study periods, Table 1 was adopted from Figure 7, which shows a comparison between the two periods. It is clear that the amount of difference for the first period is greater than the second period, and this indicates that the maximum temperatures are close to their

TABLE 1. The statistics, mean for two periods of study for Baghdad

Period	Start deviation at 8°C	End deviation at 8°C	Mean
1970–1991	0.6	0.5	0.55
1992–2017	0.2	0.5	0.35

characteristics in the summer season. Accordingly, the ratio of the difference between the temperatures of the two periods is 63%.

The amplitudes of monthly variability had same distance from leaner correlation especially in 1999, and 2013, that represent coherent wave with summer seasons. The variance difference for T_{max} between May and June approximately was 2°C for second study's period, while exceed this range in first period. This variance change to 7.5°C when find difference between July and May. There is a slight geographic variation in the beginning and end of the season, so that May had characters approaching to strong summer features for the maximum temperature. The 1992 was the beginning of climate change, before 1992 May had different behavior to the summer months, but after the 1992 May was closed to the summer characteristics months through behavior point.

Standard deviation is used to find the dispersion error and standard deviation for both May and summer as shown in Table 2. Be confirmed again that May was near to summer than spring in light of seasonal variation and climate change.

Conclusions

A surface temperature data set for Baghdad have been used to study changes in Baghdad in order to examine the seasons temperature over five decades. Objective study of observation seasonal variation to understand that changes happen in monthly air temperature refer to extended daily length in summer season beside the effect of latitude. This lead to change in solar zenith angle that slightly increased. Another less effect was geographic variation in the beginning and end of the season. Significant point was summer season had extend in Baghdad to May instead of June. Since May 1992 the approaching of May was very clear because May is the first month of year when summer extend, beside May was found in spring season before 1992 according to properties of maximum temperature. The effect of Baghdad location, climate change, increased air temperature, and variation of surface air temperature lead to increased maximum air temperature for all season particularly in spring make may approaching to summer season. Before 1992 these factors

TABLE 2. Statistics characteristics for May, June, and July and the difference for Baghdad city

Statistics	May	June	July	June–May	July–May	July–June
Standard deviation	1.5009	1.0466	1.3121	1.3310	1.4357	1.3138
Standard error	0.2166	0.1511	0.1894	0.1921	0.2072	0.1896
Confidence	0.5816	0.4056	0.5084	0.5158	0.5564	0.5091

have less effect on maximum for Baghdad city. The inter-seasonal variation for May, June and July was about 6°C, this mean the three months are similar in terms of the variation in maximum temperatures, and this refer to that general trends tend to increased T_{max}.

The behavior of air temperature for Baghdad city during the summer months tends to increase despite the fluctuations between the increase and decrease. Such observations are consistent with global trends in temperature. The results indicate the possibility of confirming the overlap of May within the summer season through the minimum temperatures of Baghdad city and the rest of the Iraqi cities. After 1992 results revealed a significant T_{max} for Baghdad during period of 1992–2017 shown that the similar behavior of T_{max} in May to June and July; on the contrary that first period (1970–1991). The variance difference for T_{max} between May and June approximately was 2°C for second study's period, while exceed this range in first period. This variance change to 7.5°C when find difference between July and May. Standard deviation is used to find the dispersion error and standard deviation for both May and summer. Be confirmed again that May was near to summer than spring in light of seasonal variation and climate change.

Acknowledgements

The authors would like to thank Mustansiriyah University (www.uomustansiriyah.edu.iq) Baghdad- Iraq for its support in the present work and Iraqi Meteorological Organization and Seismology (IMOS) for providing observed data.

References

Ahmed, E.S. & Hassan, A.S. (2018). The impact of the extreme air temperatures on the characteristics of Iraq weather. *Iraqi Journal of Agriculture Sciences*, *59*(2), 1139-1145.

Bilal, D.A., Kais, J.A. & Enas, A.H. (2013). Air temperature Trends in Baghdad, Iraq for the Period 1941–2000. *International Journal of Scientific and Research Publications*, *3*(9), 1-5.

Chitu, E., Giosanu, D. & Mateescu, E. (2015). The variability of seasonal and annual extreme temperature trends of the latest three decades in Romania. *Agriculture and Agricultural Science Procedia*, *6*, 429-437.

Hassan, A.S. & Alhashimi, A.K. (2018). Effect of increasing population density on air temperature for Baghdad City. *Al-Mustansiriyah Journal of Science*, *29*(1), 9-14.

Iraqi Meteorological Organization and Seismology [IMOS] (2017). Climate data for Baghdad Governorate Ministry of Transport 1970–2017. IMOS Climate Section [unpublished data].

Liu, X., Yin, Z.Y., Shao, X. & Qin, N. (2006). Temporal trends and variability of daily maximum and minimum, extreme temperature events, and growing season length over the eastern and central Tibetan Plateau during 1961–2003. *Journal of Geophysical Research: Atmospheres*, *111*(D19). https://doi.org/10.1029/2005JD006915

Muter, S.A. (2014). *Variability of daily maximum and minimum temperature for summer seasons in Baghdad City* (master thesis). Mustansiriyah University, Baghdad.

National Centers for Environmental Information [NCEI] (2020). Climate at a Glance: Global Time Series [database]. Retrieved form: https://www.ncdc.noaa.gov/cag

Vicente-Serrano, S.M., López-Moreno, J.I., Correa, K., Avalos, G., Bazo, J., Azorin-Molina, C., Dominguez-Castro, F., El Kenawy, A., Gimeno, L. & Nieto, R. (2018). Recent changes in monthly surface air temperature over Peru, 1964–2014. *International Journal of Climatology*, *38*(1), 283-306.

Wang, F., Li, Y. & Li, J. (2019). Spatiotemporal characteristics of the dominant modes of surface air temperature interannual varia-

tions over south China during the spring-to--summer transition. *Atmosphere*, *10*(2), 65. https://doi.org/10.3390/atmos10020065
World Atlas (2021). Free download printable political and physical maps of the world, world map satellite. Satellite 3rd Interative World map, Baghdad City map. Retrieved from: http://world-map1.org
Wu, R. & He, Z. (2017). Two distinctive processes for abnormal spring to summer transition over the South China Sea. *Journal of Climate*, *30*(23), 9665-9678.
Zarenistanak, M., Dhorde, A.G. & Kripalani, R.H. (2014). Trend analysis and change point detection of annual and seasonal precipitation and temperature series over southwest Iran. *Journal of Earth System Science*, *123*(2), 281-295.
Zeki, Kh.N. (2017). Effect of maximum air temperature on the monthly average temperature and the comfortable of human in Baghdad Station. *College of Education Journal*, *2*(2), 389-407.

Summary

Approaching of May maximum surface air temperature to characteristic summer season for Baghdad city. Seasonal variability is the complex non-linear response of the physical climate system. There are two types of natural variability: those external and internal to the climate system. In any given season, natural variability may cause the climate to be different than its long-term average. This study examines with the seasonal variation of the maximum temperatures during the summer season. In addition, the maximum temperatures in May become close to the characteristics of the summer season. The monthly data for maximum temperature of May, June and July were used from Iraqi Meteorological Organization and Seismology (IMOS) for 47 years from 1970 to 2017 for Baghdad city. This period was long enough to estimate the range of approaching maximum temperature (T_{max}) May to summer. Results revealed a significant T_{max} for Baghdad during the second period (1992–2017) and shown similar behavior of T_{max} in May to June and July; on the contrary that first period (1970–1991). In second period, two phases have been found out, positive phase and negative phase. The positive phase were happened in 1995, 1999, and 2006, and the negative phase was four cases (1992, 2004, 2013, and 2016), while a few cases recorded in first period. The amplitudes of monthly variability had same distance of leaner correlation especially in 1999 and 2013 that represent coherent wave with summer seasons. The variance difference for T_{max} between May and June approximately was 2°C for second study's period, while exceed this range in first period. This variance change to 7.5°C when found difference between July and May.

Authors' address:
Sara Ali Muter – corresponding author
(https://orcid.org/0000-0002-6728-9609)
Mustansiriyah University
College of Science
Department of Atmospheric Sciences
Palestine Street, 14022 Baghdad
Iraq
e-mail: sara.a.atmsc@uomustansiriyah.edu.iq

Jasim H. Kadhum
Ahmed S. Hassan
Mustansiriyah University
College of Science
Department of Atmospheric Sciences
Palestine Street, 14022 Baghdad
Iraq

Scientific Review – Engineering and Environmental Sciences (2021), 30 (3), 411–423
Sci. Rev. Eng. Env. Sci. (2021), 30 (3)
Przegląd Naukowy – Inżynieria i Kształtowanie Środowiska (2021), 30 (3), 411–423
Prz. Nauk. Inż. Kszt. Środ. (2021), 30 (3)
http://iks.pn.sggw.pl
DOI 10.22630/PNIKS.2021.30.3.35

Hakim Saeed M. ALKURAYSHI[1], Adnan Kadhim JAWAD[1], Alaa Mohsin DAWOOD[1], Ahmed HAKIM S.[2]

[1] Alfurat Alawsat Technical University, Najaf Technical College
[2] Civil engineer private sector, Najaf, Iraq

Longitudinal shear in composite deck slabs using corrugated steel sheets

Key words: corrugated sheets, shear transfer, shear span, slip, deflection

Introduction

Composite deck slabs can be defined as that slabs in which a profiled deck sheets are used as a base on which reinforced concrete is poured to make composite action. This composite phenomenon mentioned can be between this mass (corrugated sheets and concrete) and the supported steel beams through the use of shear connectors. A cold-formed steel deck sections are not only used as supporting form (mold) before hardening of concrete but also as a principal tensile reinforcement for the bottom fibers of the composite slab. Porter and Ekberg (1975) carried out full-scale tests on composite slabs to establish shear-bond failure mechanism. The steps of construction of such slabs can be seen in Figures 1 and 2.

The composite action is achieved by means of positive interlocking between corrugated steel sheets (deck) and the concrete by may be embossments, indentations, transverse wires attached to the deck corrugations, holes in corrugations or interface bonding between deck and steel.

Two types of steel sheets were used in trapezoidal and re-entrant shapes in bending and pushed out tests to find *m–k* parameters. The loads were applied longitudinally and transversely. That work was done by Wright et al. (1987). They concluded that increase in height of embossments will improve the load carrying capacity of the composite structure. A new method to determine the strength and stiffness of the composite slabs was developed by Easterling and Young (1992). A six slabs were cast and the

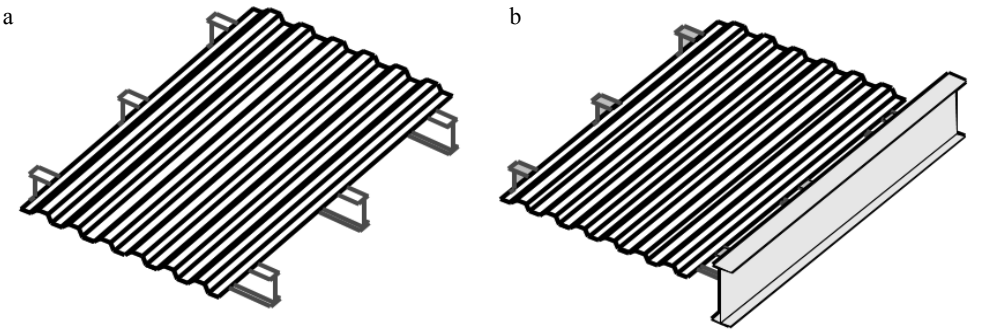

FIGURE 1. a – Steel beams supporting corrugated steel sheets; b – supporting beams rested on steel girders

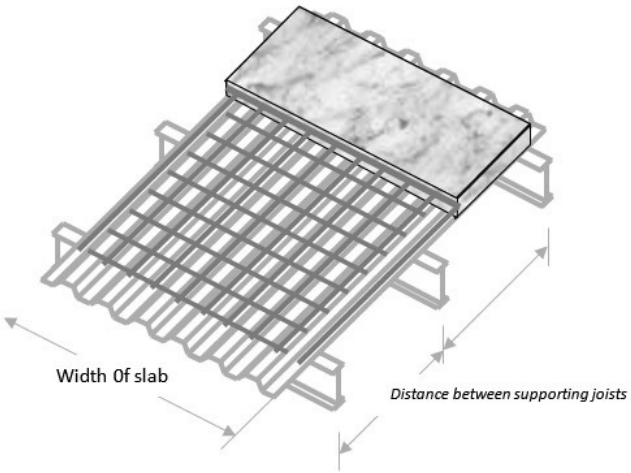

FIGURE 2. Erection of steel reinforcement and pouring of concrete

results of the analytical and experimental results were compared to reach the criteria in which a proper anchorage at the ends of the slabs should be provided.

Mäkeläinen and Sun (1999) studied the phenomena of shear connection in composite slabs using profiled steel sheets. A push-out tests were carried out on 27 samples. The parameters which were studied include different geometrical shapes, sizes, thickness of sheets and location of embossments. As a conclusion recorded was that the embossment depth plays a vital role in increasing shear stress. As a continuation of the previous work, Burnet and Oehlers (2001) developed a simulation of the bond between profiled sheets and concrete more accurate in push tests as a results of testing 33 specimens. Dove-tailed and trapezoidal rib shear connections were used to study chemical bond and mechanical bond strengths. A higher shear bond strength was governed in composite slabs that have end anchorage compared to that without end anchorage. That were the concluded remarks drawn by Chen (2003) in testing seven simply supported one span composite slabs.

Marčiukaitis, Jonaitis and Valivonis (2006) mentioned that the application of load on composite slabs using profiled

steel sheets will lead to the truth that the connection between these sheets and concrete is not absolutely stiff and cracks shall appear in tension zone of the concrete. A new effort was recorded by Marimuthu et al. (2007) that the shear span is an effective parameter in composite slab uses embossed profiled steel sheets. If the shear span is short, the slab strength is governed by shear bond failure and by flexural failure in large shear spans. The partial interaction between the two materials of such composite structure was studied by Jeong (2008) making use of the push out tests. His work was coincided with the results governed from *m–k* method. The state of art recommends that this is a useful way to treat with partial interaction. The shear bond in composite slabs can be found from bending test data. This bond can be calculated through a procedure called force equilibrium method which is the effort produced by Abdullah and Easterling (2009).

Hedaoo, Gupta and Ronghe (2012) casted 18 full-scale composite slabs specimens to know their structural behaviour and load carrying capacity. He reached that the *m–k* method results are weaker than the experimental method by about 43%. One of the famous works to overcome slip in composite slabs was done by Lakshmikandhan, Sivakumar, Ravichandran and Jayachandran (2013) through using three types of mechanical connector schemes. During the tests of full-scale specimens, no any visible delamination and slip had been shown. The effect of thickness of the profiled steel sheets was studied by Cifuentes and Medina (2013) when three different thicknesses were tested. Thickness of these sheets show very important parameter in considering longitudinal shear strength especially in long-span specimens.

The effect of shear span was studied in Australia through testing four types of profiled decking, two of them trapezoidal and other two were re-entrant by Gholamhoseini, Gilbert, Bradford and Chang (2014). They studied two types of shear spans $L/6$ and $L/4$. The ultimate shear stress for $L/6$ is greater than that for $L/4$. Japan and Vakil (2014) studied theoretically the effect of varying profiled thickness with and without embossments by modeling that in ANSYS-15. The deflection and stress of the composite slabs were affected directly by thickness variation. The relation was found to be linearly proportional to some extent.

Experimental work

The experimental investigation of composite profiled slabs comprises the following activities:

- materials used;
- casting of slabs;
- testing of slab specimens and instrumentation.

The materials, which were used to prepare concrete, were confirmed with Iraqi specifications including cement, i.e. IQS 5/1984 standard (Central Organization for Standardization and Quality Control [COSQC], 1984b), gravel and sand, i.e. IQS 45/1984 standard (COSQC, 1984a). The mix design for concrete compressive strength was done in the lab to get concrete of 25 MPa. Steel reinforcement used were mesh fabric of 6 mm diameter bars and 150 mm C/C distance in two directions. The

yield stress of the steel was 410 MPa. The steel sheets used were galvanized and their properties are listed in Table 1 and a part of the corrugation can be seen in Figure 3. These sheets are without embossments.

The slabs were casted after pouring the concrete on the steel sheets which will work as form before hardening of concrete. Concrete cubes, cylinders and prisms were taken to test them until the actual compressive and tensile strengths of concrete were governed. The profile steel sheets used has dimensions of 2.5 × 0.9 m. Wooden form was used to keep concrete in its position at the above boundaries of the slab. A mesh of 6 mm diameter bars at 150 mm C/C in both directions was used and suited at 25 mm above top of profile sheet.

The instrumentation was arranged and set up as shown in Figure 4 to test the hardened slab in accordance with the Eurocode 4. Part 1-1 (European Committee for Standardization [CEN], 2004). Linear variable differential transformers (LVDTs) were used to measure the horizontal slip as shown in Figure 4. They were installed in such a manner that two of them were used to measure slab slip and another two for measuring slip in profiled sheet to find out the relative slip between the concrete and the used corrugated steel sheet. A two dial gauges were fixed at the lower part of the mid-span length to read the mid deflection of the slab. The load was applied gradually through two-line loads across the transverse dimension of the slab at a rate of 1 kN in a start of the test. Afterwards it

TABLE 1. Properties of corrugated sheet

Property	Value
Width of corrugated sheet	0.9 m
Length of corrugated sheet	2.5 m
Thickness of the sheet	0.7 mm
Weight of the sheet	14.37 kg
Number of pieces in 0.9 m width of sheet	4.615
Length of each piece	215 mm
Total length in 0.9 m width of corrugated plate	992.23 mm
Gross area	694.56 mm^2
Distance from center of gravity to the base "y"	6.57 mm
Moment of inertia (I) about the centroidal axis	46 608 mm^4
Z_U (for upper position)	2 529 mm^3
Z_L (for lower position)	7 094 mm^3
Shear capacity of the profile sheet	25.25 $kN \cdot m^{-1}$
Moment capacity of the profile sheet	2.4 kN·m
Yield stress of the sheet (use coupons samples)	215 $N \cdot mm^{-2}$

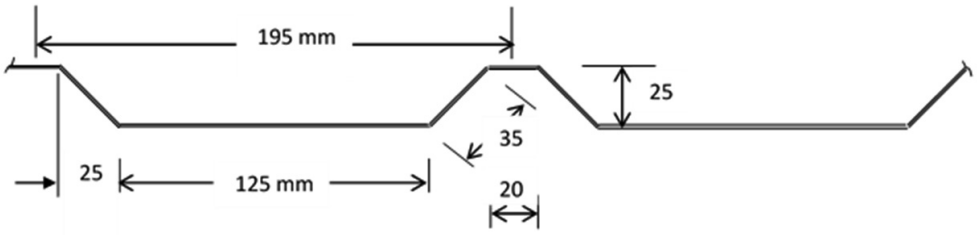

FIGURE 3. Profiled corrugated steel sheets

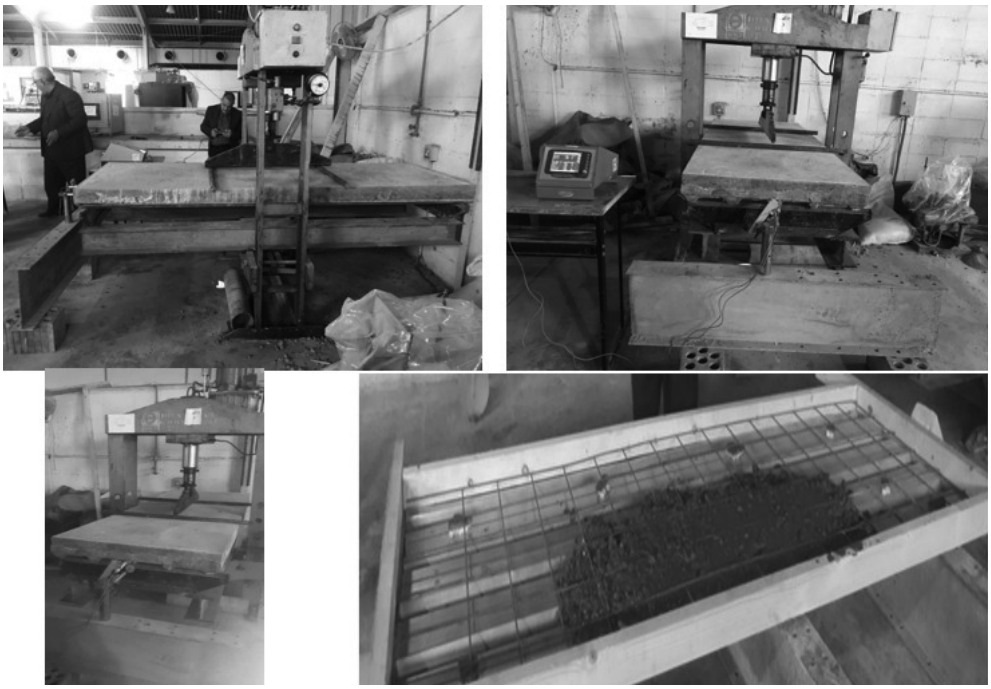

FIGURE 4. Test set up of the composite slab and casting concrete

is increased to 2 kN in a way that was shown in Figure 5.

The shear span is taken in a way that verified the provisions of the Eurocode 4. Part 1-1. It was taken in two ways short and long shear spans. The shorter shear spans must not be less than three times the composite deck depth

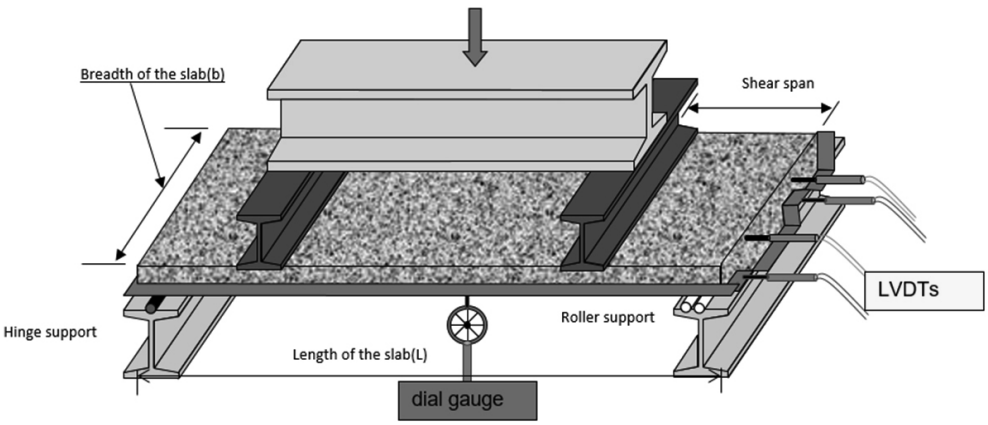

FIGURE 5. Arrangement of the slab test

and not more than 1,250 mm therefore they were taken as 600, 500 and 400 mm respectively in this study. The provision of the longer shear span is not less than 1/4 the slab length. So, they were selected as 800, 750 and 700 mm. According to Eurocode 4. Part 1-1, Clause 9.2.1, the following conditions were fulfilled:

1. The overall depth of the composite slab (h) shall be not less than 80 mm. The thickness of concrete (h_c) above the main flat surface of the top of the ribs of the sheeting shall be not less than 40 mm.
2. Transverse and longitudinal reinforcement shall be provided within the depth of the concrete (h_c).
3. The amount of reinforcement in both directions should be not less than 80 $mm^2 \cdot m^{-1}$.
4. The spacing of the reinforcement bars should not exceed 2h and 350 mm, whichever is the lesser.

For each shear span a static testing was done by applying loading till a mid-span deflection is reached a limit of 1/50 times span length. Cyclic testing was not done because most of literature studies recommended that it has no effect in shear transfer study.

Results and discussion

The results which were recorded include testing the slabs to find out the mid-span deflection and the longitudinal slip to build the equation mentioned by Porter and Ekberg (1975), through the investigation of finding m and k. This needs the results of testing three shorter shear spans besides three longer shear spans. The results of mid-span deflection of the shorter shear spans can be shown in Figure 6. As shown from the graphs they are taking same trend and deflections recorded are so small in the first stage in which higher values of loads are applied. As slip occurs the deflection is increased rapidly due to the appearance of shear cracks and separation of corrugated sheets from the concrete. This is really a new stage because a fluctuation is seen in the load applied. Afterwards a flexural crack had been started in the middle part of the slab till failure as shown in Figure 7. The appearance of these cracks facilitates the deflection to be increased. As shear span value increased, a higher deflection is registered and that is clear in results of 800 mm shear span in which the deflection was 60 mm compared to other shear spans.The maximum load was recorded in the minimum shear span (700 mm) where it was 21 kN and that is because the shear span is the arm of the applied load affecting on the nearest support. The same graphs trend was seen in testing and drawing the load deflection curves of shorter spans as seen in Figure 8 except that the values recorded of the loads and deflections are higher compared to the longer shear spans. This fact due to decreasing in the force arm and the delay in slip between sheets and concrete.

Figure 9 shows the relationships between load applied and slip for longer shear spans. The shape of these relationships like that of the deflection relations. The most important phenomenon seen in these relations including the shorter shear spans shown in Figure 10 that, very small values of slip are recorded at the start of the test while the loads reach higher values near or equal to ultimate or

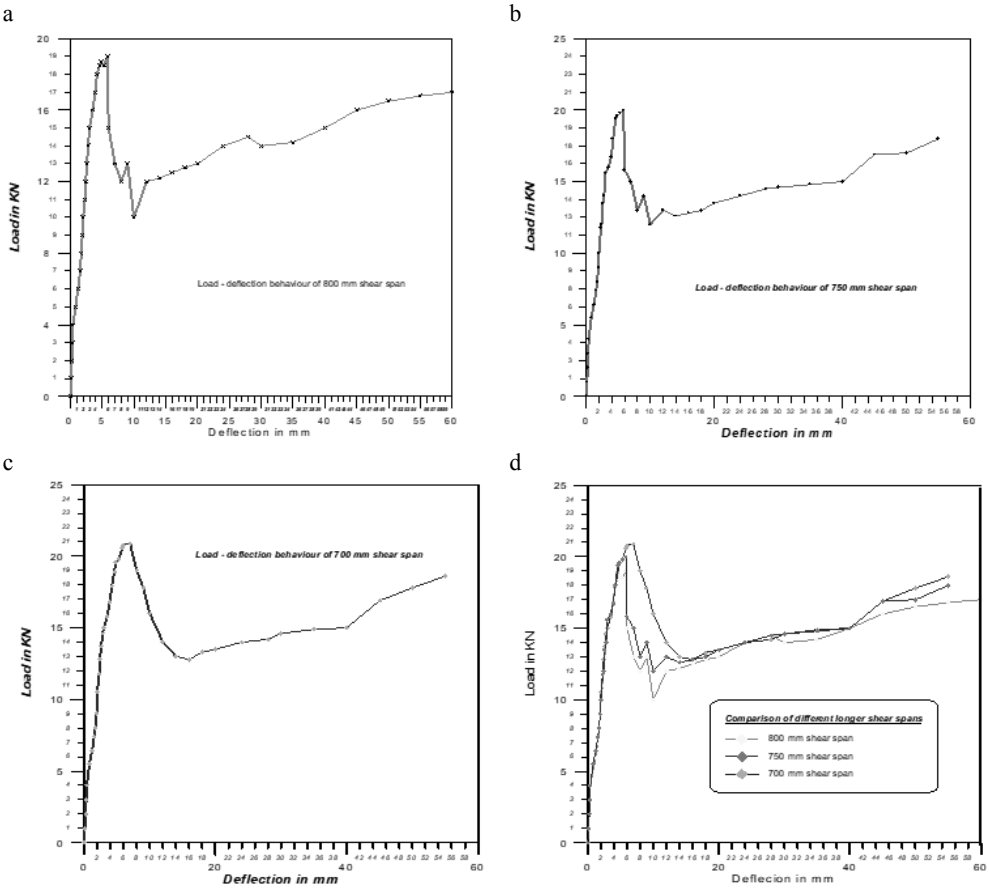

FIGURE 6. Mid-span deflections of shear spans: a – 800 mm; b – 750 mm; c – 700 mm; d – comparison among the three shear spans

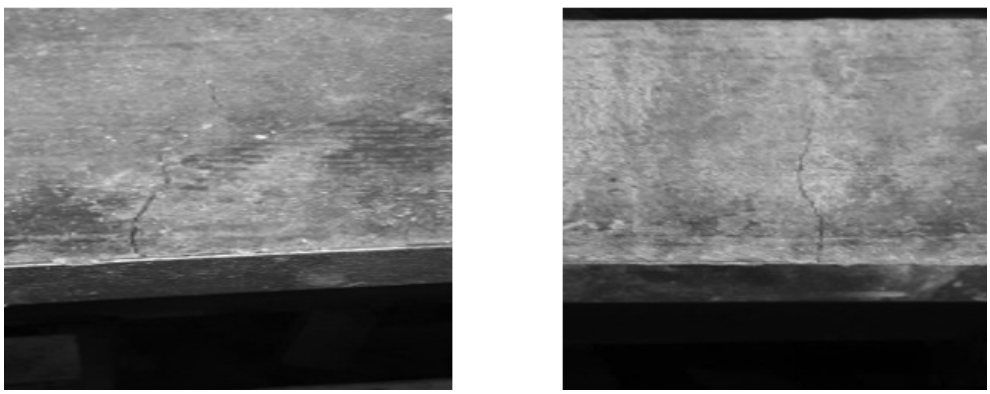

FIGURE 7. Shear and flexural cracks appeared during tests of the composite slabs

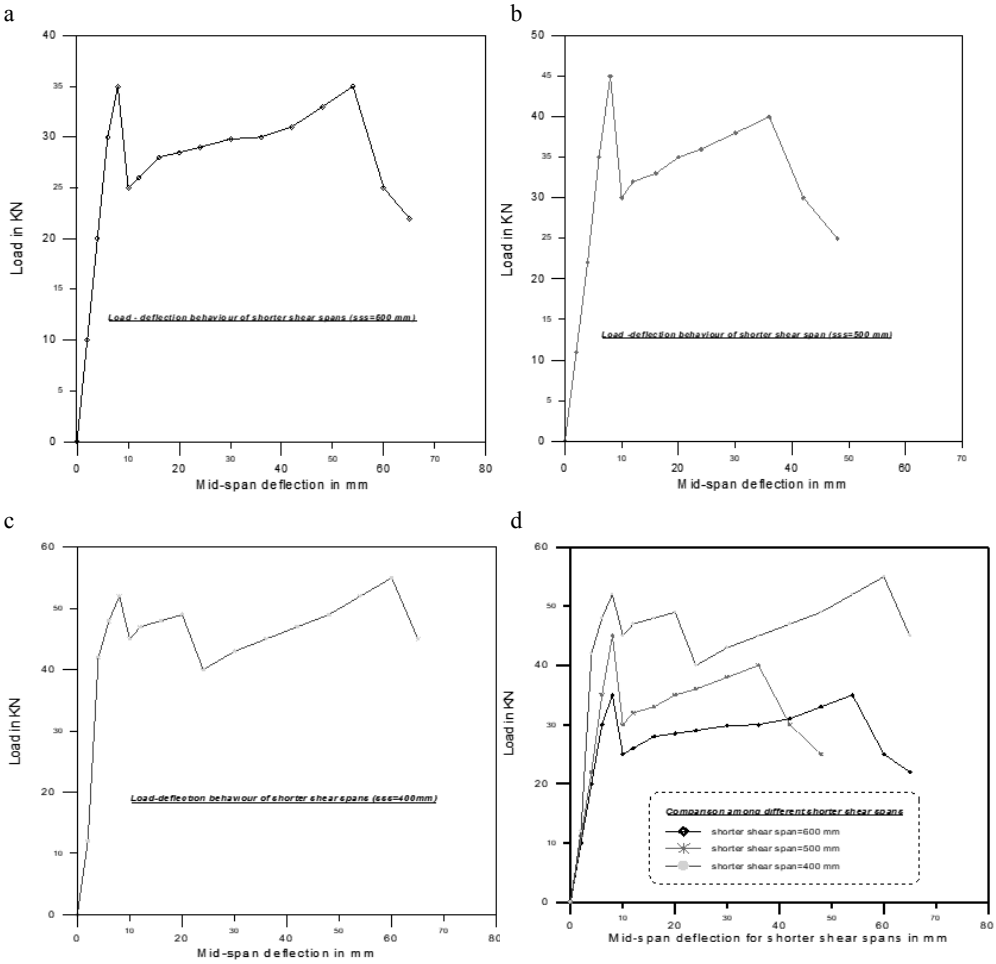

FIGURE 8. Mid-span deflections of shear spans: a – 600 mm; b – 500 mm; c – 400 mm; d – comparison among the three shear spans

failure load. The explanation of this matter is that as load increased deflection in the middle region of the slab increased. This condition try to break the bonds between the concrete and sheets at the end edges of the slab and ignores the monolithic action therefore slip increased as deflection increased and that is clear from whole curves. In the two types of spans the slab material behaves as brittle under the applied load and as deflection and slip increased it will behave as ductile as it was shown in all relations that all failure loads are less than the maximum load registered at very small slips.

In Eurocode 4. Part 1-1, Clause 9.7.3, Point 3 states that "the longitudinal shear behaviour may be considered as ductile if the failure load exceeds the load causing a recorded end slip of 0.1 mm by

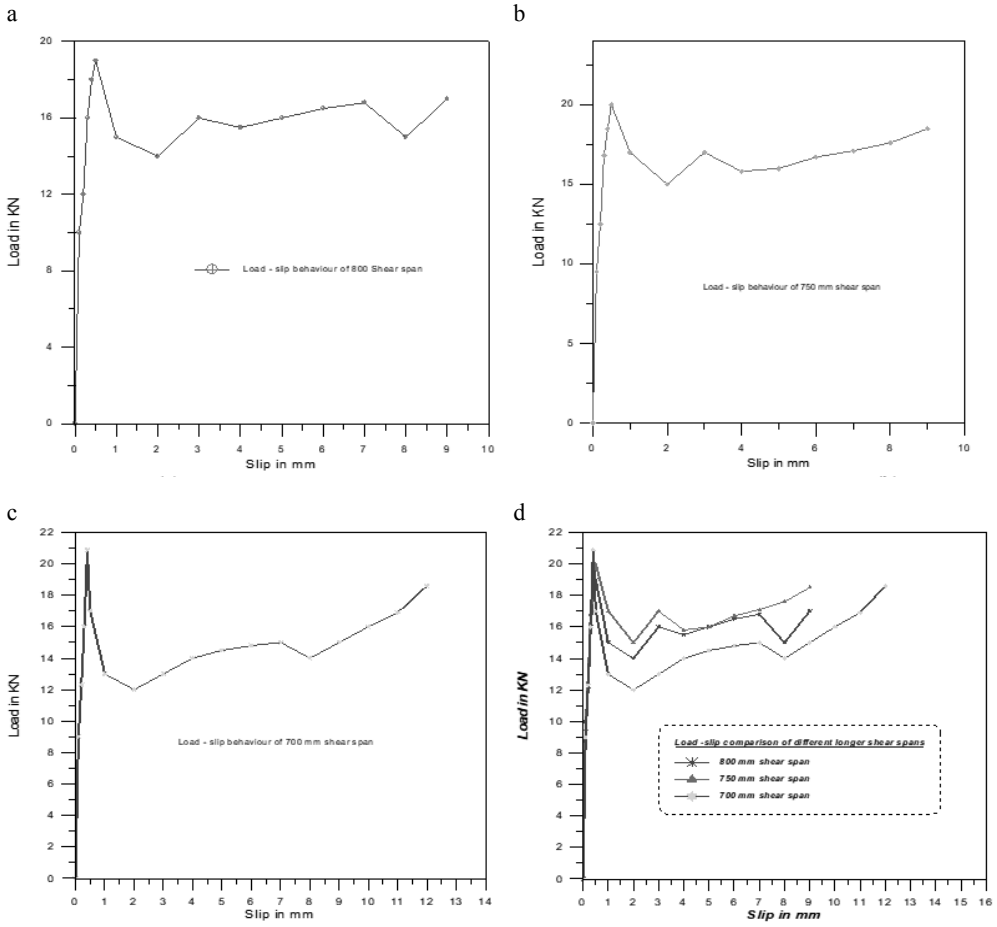

FIGURE 9. Slip of shear spans: a – 800 mm; b – 750 mm; c – 700 mm; d – comparison among the three shear spans

more than 10%. If the maximum load is reached at a midspan deflection exceeding $L/50$, the failure load should be taken as the load at the midspan deflection of $L/50$" (CEN, 2004, p. 102). The results of the present study are coincided with this clause for shorter and longer shear spans. Point 4 in the same clause recommended the equation of the design for shear bond capacity of composite deck slabs as:

$$\frac{V_u}{bd_p} = m\frac{A_p}{bL_s} + k \quad (1)$$

So, this equation is a linear equation in which the slope of the straight-line m must be determined and the intercept k also to evaluate the shear transferring capacity of the profiled sheet. The evaluation of these two parameters needs an

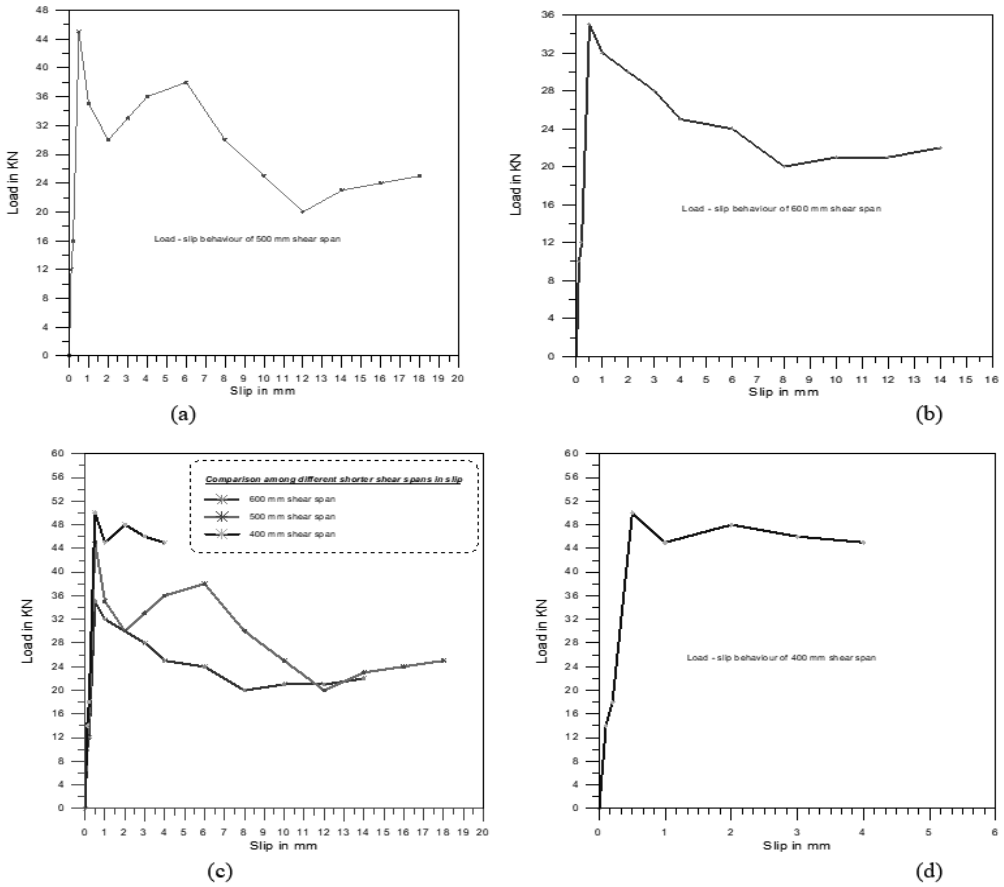

FIGURE 10. Slip of shear spans: a – 600 mm; b – 500 mm; c – 400 mm; d – comparison among the three shear spans

experimental test for each new type of profiled steel sheets and that is the main aim of the present study. In drawing the results of the shorter and longer shear spans where V_t is taken to be 0.5 the failure load including the own weight of the slab and corrugated sheet, the straight line will be governed as shown in Figure 11. The slope of this line represents m and k is represented by the intercept. The values of these parameters determined from this study are m = 65 and k = 0.094.

The design equation for this corrugated steel sheets will be:

$$\frac{V_u}{bd_p} = 65 \cdot \frac{A_p}{bL_s} + 0.094 \qquad (2)$$

To make comparison with other profiled sheets, the values evaluated for this new corrugated sheet can be seen in Table 2.

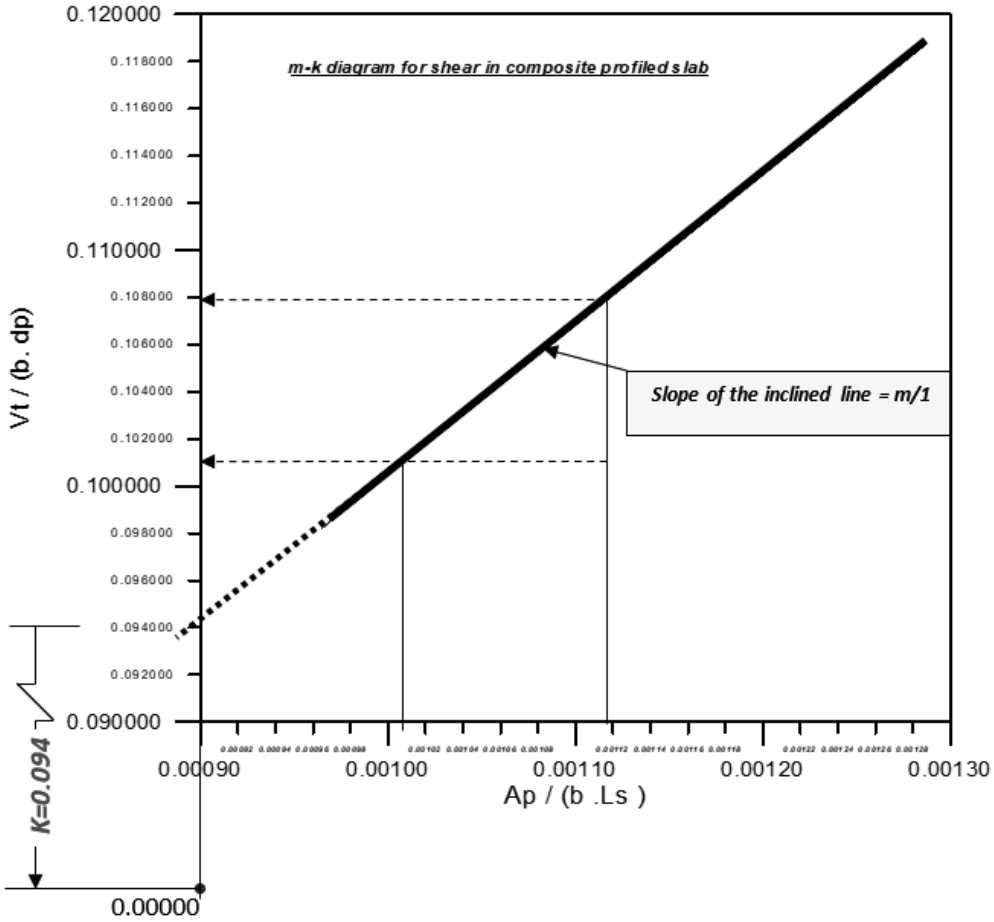

FIGURE 11. Graph of *m–k*

TABLE 2. Comparison among available profile steel sheets

Reference or author	Profile type	Embossment type	*m*	*k*
Wright, Evans & Harding (1987)	trapezoidal	Chevron embossments @90°	107.527*	0.0401
Chen (2003)	trapezoidal	Chevron embossments @0°	84.665*	0.0221
Marimuthu et al. (2007)	trapezoidal	rectangular dishing type of embossments	87.956*	0.0322
Saravanan, Marimuthu, Prabha, Arul Jayachandran & Datta (2012)	trapezoidal	rectangular embossments in web and flange	96.95*	0.043
Present work	trapezoidal	without embossments	65	0.094

*Saravanan et al. (2012).

Conclusions

As a result of the use of different longer and shorter shear spans to investigate the effect of using this type of profiled steel sheets, the following conclusions can be mentioned:

- The value of *m* is the predominant factor in the shear design transfer equation, therefore increasing it means increasing the value of shear transferred and yet slip will occur. In the present study the value of *m* is the smallest among others while *k* is the largest value recorded. The evaluated values of *m* and *k* are 65 and 0.094 respectively.
- The present type of sheets is used here in wide range, therefore need to study shear transfer becomes a pressurized matter. A recommendation here can be drawn that if a shear connector can be added to the action of using such sheets in composite slabs.
- All samples tested pass through two stages brittle and ductile. No sample failed in sudden or catastrophic failure.

References

Abdullah, R. & Easterling, W.S. (2009). New evaluation and modeling procedure for horizontal shear bond in composite slabs. *Journal of Constructional Steel Research*, *65*(4), 891-899.

Burnet, M.J. & Oehlers, D.J. (2001). Rib shear connectors in composite profiled slabs. *Journal of Constructional Steel Research*, *57*(12), 1267-1287.

Central Organization for Standardization and Quality Control [COSQC] (1984a). *Fine and coarse aggregates* (IQS 45/1984). Baghdad: Iraqi Central Agency for Standardization and Quality Control (translated from Arabic edition).

Central Organization for Standardization and Quality Control [COSQC] (1984b). *Portland cement* (IQS 5/1984). Baghdad: Iraqi Central Agency for Standardization and Quality Control (translated from Arabic edition).

Chen, S. (2003). Load carrying capacity of composite slabs with various end constraints. *Journal of Constructional Steel Research*, *59*(3), 385-403.

Cifuentes, H. & Medina, F. (2013). Experimental study on shear bond behavior of composite slabs according to Eurocode 4. *Journal of Constructional Steel Research*, *82*, 99-110.

Easterling, S.W. & Young, C.S. (1992). Strength of composite slabs. *Journal of Structural Engineering*, *118*(9), 2370-2389.

European Committee for Standardization [CEN] (2004). *Eurocode 4: Design of composite steel and concrete structures*. *Part 1-1: General rules and rules for buildings* (EN 1994-1-1:2004). Brussels.

Gholamhoseini, A., Gilbert, R.I., Bradford, M.A. & Chang, Z.T. (2014). Longitudinal shear stress and bond–slip relationships in composite concrete slabs. *Engineering Structures*, *69*, 37-48.

Hedaoo, N.A., Gupta, L.M. & Ronghe, G.N. (2012). Design of composite slabs with profiled steel decking: a comparison between experimental and analytical studies. *International Journal of Advanced Structural Engineering*, *4*(1), 1-15.

Japan, U.S. & Vakil, M.D. (2014). Parametric study of composite slab using finite element analysis. *International Journal of Futuristic Trends in Engineering and Technology*, *1*(03), 133-136.

Jeong, Y.J. (2008). Simplified model to predict partial-interactive structural performance of steel–concrete composite slabs. *Journal of Constructional Steel Research*, *64*(2), 238-246.

Lakshmikandhan, K.N., Sivakumar, P., Ravichandran, R. & Jayachandran, S.A. (2013). Investigations on efficiently interfaced steel concrete composite deck slabs. *Journal*

of Structures, *2013*, 628759. https://doi.org/10.1155/2013/628759

Mäkeläinen, P. & Sun, Y. (1999). The longitudinal shear behaviour of a new steel sheeting profile for composite floor slabs. *Journal of Constructional Steel Research*, *49*(2), 117-128.

Marčiukaitis, G., Jonaitis, B. & Valivonis, J. (2006). Analysis of deflections of composite slabs with profiled sheeting up to the ultimate moment. *Journal of Constructional Steel Research*, *62*(8), 820-830.

Marimuthu, V., Seetharaman, S., Jayachandran, S.A., Chellappan, A., Bandyopadhyay, T.K. & Dutta, D. (2007). Experimental studies on composite deck slabs to determine the shear-bond characteristic (m–k) values of the embossed profiled sheet. *Journal of Constructional Steel Research*, *63*(6), 791-803.

Porter, M.L. & Ekberg, C.E. Jr. (1975). Design recommendations for steel deck floor slabs. In *3-rd International Specialty Conference on Cold-Formed Steel Structures.* Columbia (MO): University of Missouri.

Saravanan, M., Marimuthu, V., Prabha, P., Arul Jayachandran, S. & Datta, D. (2012). Experimental investigations on composite slabs to evaluate longitudinal shear strength. *Steel & Composite Structures*, *13*(5), 489-500.

Wright, H.D., Evans, H.R. & Harding, P.W. (1987). The use of profiled steel sheeting in floor construction. *Journal of Constructional Steel Research*, *7*(4), 279-295.

Summary

Longitudinal shear in composite deck slabs using corrugated steel sheets. Profile deck steel sheets are used in composite deck slabs. These sheets are standard in dimensions and shapes besides they are supplied with embossments and indentations. Such sheets are not available in Iraqi markets nowadays therefore people used another type of sheets which are corrugated without embossments or indentations in very wide range. This study covers the use of such sheets in composite slabs as decks instead of standard profiled steel sheets. The study comprises testing slabs of dimensions 0.9 × 2.5 m reinforced by steel fabric mesh and rested on corrugated sheets. Two types of shear spans are selected shorter and longer to study the longitudinal shear force transmitted due to the applied loads according to the Eurocode 4. The shorter shear spans are 600, 500 and 400 mm while longer one is 800, 750 and 700 mm. The study extended to support the requirements of design equation of the Eurocode by shear bond method also known as *m–k* method. The evaluated values of *m* and *k* are 0.094 and 65 respectively. The result of *k* which plays a very important role in shear transfer is small compared to what available in literature, therefore it is recommended to make use of shear connectors in such construction or any else method.

Authors' address:
Hakim Saeed M. Alkurayshi – corresponding author
(https://orcid.org/0000-0002-2805-5260)
Alfurat Alawsat Technical University
Najaf Technical College
Babylon-najaf street, 54003, Najaf
Iraq
e-mail: t.kadum@yahoo.com

Scientific Review – Engineering and Environmental Sciences (2021), 30 (3), 424–438
Sci. Rev. Eng. Env. Sci. (2021), 30 (3)
Przegląd Naukowy – Inżynieria i Kształtowanie Środowiska (2021), 30 (3), 424–438
Prz. Nauk. Inż. Kszt. Środ. (2021), 30 (3)
http://iks.pn.sggw.pl
DOI 10.22630/PNIKS.2021.30.3.36

Yevhen DMYTRENKO[1], Ihor YAKOVENKO[1], Oleg FESENKO[2]

[1] National University of Life and Environmental Sciences of Ukraine, Faculty of Construction and Design
[2] The State Research Institute of Building Constructions

Strength of eccentrically tensioned reinforced concrete structures with small eccentricities by normal sections

Key words: reinforced concrete structures, deformation model, two-line stress-strain diagram, non-eccentric tension with small eccentricities, normal cross sections

Introduction

Experimental-theoretical researches and improvement of the calculation theory of reinforced concrete structures by the action of diverse influences, such as strength, rigidity and crack resistance is a very important scientific problem in civil engineering.

New concepts for the calculation of reinforced concrete structures are being developed (Pavlikov, Kochkarev & Harkara, 2019), existing methods are being improved (Kolchunov & Yakovenko, 2016; Karpyuk, Kostyuk & Semina, 2018; Karpiuk, Somina & Antonova, 2019), including with the involvement of the calculation apparatus of fracture mechanics (Iakovenko, Kolchunov & Lymar, 2017). In accordance with the current building codes of Ukraine in the field of design of reinforced concrete structures, i.e. the DBN V.2.6-98:2009 standard (Ukrayinskyy naukovo-doslidnyy i navchalnyy tsentr problem standartyzatsiyi, sertyfikatsiyi ta yakosti [SE UkrNDNC], 2011a) and the DSTU B.V.2.6-156:2010 standard (SE UkrNDNC, 2011b), normal cross sections of reinforced concrete elements are calculated according to the boundary conditions of the first and second groups using the deformation method.

The main feature of this method is the solution of a system of non-linear equations. Therefore, the use of numerical calculation methods, modern software packages for their implementation is an integral part of this process. A characteristic feature of the above normative

documents is that they practically do not consider cases of stress-strain state (SSS) of normal sections with off-center tension. In particular, this applies to the case of small eccentricities, there are no practical recommendations for the use of the deformation method. In practical manuals for building codes (Babayev, Bambura & Pustovoitova, 2015; Bambura, Pavlikov, Kolchunov, Kochkarev & Yakovenko, 2017; Wojciechowski & Zhuravsky, 2017) this issue is also insufficiently covered. The appearance of the first cracks (Bambura et al., 2017; Iakovenko & Kolchunov, 2017) in reinforced concrete structures significantly affects their rigidity. This further significantly reduces the load-bearing capacity of both normal and inclined sections. A special influence on the appearance and spread of cracks has a complex resistance – torsion with bending (Dem'Yanov, Yakovenko, Kolchunov, 2017; Dem'Yanov, Kolchunov, Iakovenko & Kozarez, 2019).

Topicality

Eccentrically stretched elements are quite common among reinforced concrete structures. These types include a fairly wide class of reinforced concrete structures – monolithic walls of tanks and hoppers rectangular in plan, the lower belts of non-skeletal trusses, pipeline structures, walls of cylindrical silos, granaries, arched structures, and so on.

When determining the SSS of normal cross sections of such elements due to the lower height of the compressed zone of concrete, its compressive strength is not fully used, as is the case with off-center compression or bending.

Execution of modern calculations of reinforced concrete structures in computer-aided design systems (Kolchunov, Yakovenko & Dmitrenko, 2016; Iakovenko et al., 2017) is based on the construction of finite-element models of rod (which simulate the work of beams, columns) and plate shell finite elements (which simulate the work of plates, diaphragms, walls).

Therefore, the search for a rational design on the basis of real research and the results of the SSS calculation of normal cross-sections of eccentrically stretched reinforced concrete structures by the deformation method is an actual task. The obtained results (Bambura et al., 2017; Kolchunov, Dem'yanov, Iakovenko & Garba, 2018) are of practical importance in the implementation of the proposed algorithms for calculations of reinforced concrete structures in modern software packages, based on the deformation model of reinforced concrete (Bambura et al., 2017) and conducting a more accurate, reliable analysis of such structures (Kolchunov et al., 2018).

Material and methods

Study area. Output data. To conduct a numerical study, the authors chose a rectangular reinforced concrete normal section of the slab fragment with double reinforcement with rod reinforcement (Fig. 1). The class of heavy concrete – C16/20, the class of longitudinal working reinforcement – A400C.

The following parameters were varied: the height of the section h and the coefficient of the accepted reinforcement ρ.

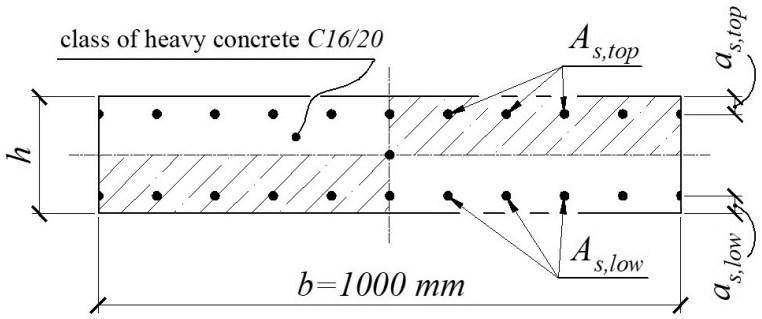

FIGURE 1. Geometric dimensions and normal section reinforcement scheme of reinforced concrete slab

This type of section is chosen due to the wide application in the modeling of both rod and plate (shell) types of finite elements. These types of finite elements make up the calculation models of buildings and structures when performing their calculation in modern software packages (for example, the PC family "Lira-CAD"). The initial data of the task are presented in Table 1.

Reinforcement of the section is taken symmetrical to prevent the impact on the external eccentricity (from external forces relative to the geometric center of gravity of the section) additional eccentricity (from the displacement of the center of gravity of the section due to asymmetric reinforcement). It should be noted that with small external eccentricities, this effect is quite significant and can in some cases lead to a change in the SSS cross section.

The calculated diagrams for concrete (Fig. 2a) and reinforcement (Fig. 2b) are accepted as bilinear with the corresponding parameters specified in the current building codes, i.e. the DBN V.2.6--98:2009 standard.

TABLE 1. Physico-mechanical characteristics and initial data for calculation of reinforced concrete cross section

Characteristics of reinforced concrete section	Value		
– sectional height – h [cm]	20	16	12
– sectional width – b [cm]	100		
– area of the longitudinal reinforcement at the top of the section – $A_{s,top}$ [cm^2]	11.31	6.5	2.25
– the area of the longitudinal reinforcement at the bottom of the section – $A_{s,low}$ [cm^2]	11.31	6.5	2.25
– the distance from the upper face of the slab to the reinforcement axis at the top of the section – $a_{s,top}$ [cm]	3		
– the distance from the lower face of the slab to the reinforcement axis at the bottom of the section – $a_{s,low}$ [cm]	3		
– section reinforcement coefficient – ρ [%]	1.33	1.0	0.5
– the coefficient of reinforcement to concrete reduction – α_s	7.407		

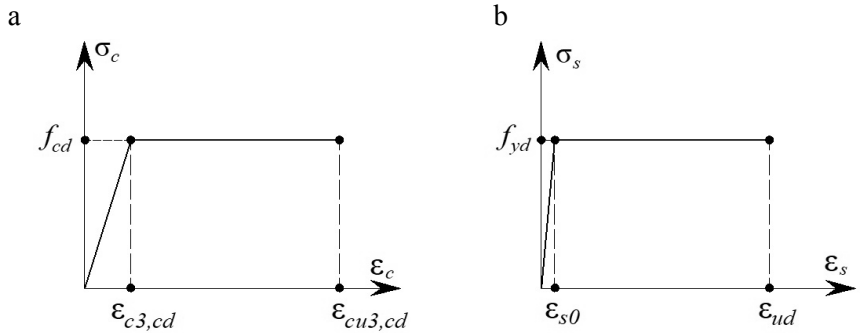

FIGURE 2. Bilinear diagrams of the stress-strain state of materials "σ – ε" are accepted at modeling: a – for concrete; b – for reinforcement

Research methodology

Stress-strain state of reinforced concrete rectangular section is flat non--eccentric tension.

This type of SSS is quite common in determining the required area of reinforcement in shell reinforced concrete elements. In the implementation of such calculations by the method of Wood–Armer (Shin, Bommer, Deaton & Alemdar, 2009) there is a problem of significant duration of their implementation due to the large number of calculated combinations of efforts in comparison with the method of Prof. N.I. Karpenko (Karpenko, 1996). That is why the developers of computerized algorithms for calculating reinforced concrete structures by the Wood–Armer method is also an important task to reduce the time of calculations and their high accuracy.

The system of non-linear equilibrium equations (in general case), which describes the operation of a normal reinforced concrete section under load (the second form of equilibrium), with a triangular diagram of the compressed zone of concrete (Fig. 3a), has the following form:

$$\begin{cases} \dfrac{b \cdot E_{cd} \cdot \varepsilon_{c(1)}^2}{2 \cdot \chi} + \sum\limits_{i=1}^{n} A_{si} \cdot \sigma_{si} - N = 0 \\ \dfrac{b \cdot E_{cd} \cdot \varepsilon_{c(1)}^3}{3 \cdot \chi^2} + \sum\limits_{i=1}^{n} A_{si} \cdot \sigma_{si} \cdot \\ \cdot \dfrac{\varepsilon_{c(1)} - \chi \cdot z_{si}}{\chi} - M = 0 \end{cases} \quad (1)$$

where:

E_{cd} – calculated modulus of elasticity of concrete in compression [MPa],

N – longitudinal force acting on the section under consideration,

M – external moment and longitudinal force acting on the section under consideration.

The external moment is dependent by next formula:

$$M = N \cdot (y + e_0 - x_1) \quad (2)$$

where:

y – distance from the extreme stretched edge of concrete to the center of section gravity [cm],

e_0 – eccentricity of external force application of relative to the center of section gravity [cm],
b – section width [cm],
χ – curvature of the bend axis in cross section is determined by the formula:

$$\chi = \frac{1}{r} = \frac{(\varepsilon_{c(1)} - \varepsilon_{c(2)})}{h} \tag{3}$$

In Eq. (3) the following notation is accepted:
$\varepsilon_{c(1)}$ – deformation of compressed fiber concrete,
$\varepsilon_{c(2)}$ – average deformations of stretched concrete fiber,
z_{si} – the distance of the i-th rod or layer of reinforcement from the most compressed edge of the section [cm],
z_{si} – the area of the i-th rod or layer of reinforcement [cm^2],
A_{si} – stresses in the i-th layer of rods or reinforcement [MPa], are determined by the deformation diagram of the reinforcement (Fig. 2b) depending on the corresponding strains ε_{si}, which are determined by the following dependence:

$$\varepsilon_{si} = \chi \cdot (x_1 - z_{si}) \tag{4}$$

where the height of the compressed zone of concrete – x_1 [cm] is defined as follows:

$$x_1 = \frac{\varepsilon_{c(1)}}{\chi} \tag{5}$$

In the case, when compressed zone of concrete has a trapezoidal diagram, the system of non-linear equations of the section equilibrium (Fig. 3b) has the following form:

$$\begin{cases} \dfrac{b \cdot f_{cd}}{2 \cdot \chi} \cdot (2 \cdot \varepsilon_{c(1)} - \varepsilon_{c3,cd}) + \\ + \sum\limits_{i=1}^{n} A_{si} \cdot \sigma_{si} - N = 0 \\ \dfrac{b \cdot f_{cd}}{3 \cdot \chi^2} \cdot (3 \cdot \varepsilon_{c(1)} \cdot \varepsilon_{c3,cd} - 2 \cdot \varepsilon_{c3,cd}^2) + \\ + \sum\limits_{i=1}^{n} A_{si} \cdot \sigma_{si} \cdot \dfrac{\varepsilon_{c(1)} - \chi \cdot z_{si}}{\chi} - M = 0 \end{cases} \tag{6}$$

where:
f_{cd} – the calculated compressive strength of concrete [MPa],
$\varepsilon_{c3,cd}$ – ultimate elastic deformations of concrete compression (Fig. 2a).

The tensile performance of concrete was not taken into account in accordance with Chapter 4.1.1 the DSTU B V.2.6--156:2010 standard.

The solution of the equations system (6) was performed according to the method presented in Appendix A of the DSTU B V.2.6-156:2010 standard for one section repeatedly by finding a balance between external forces M and N and forces arising in concrete and reinforcement. The implementation of the above algorithm was performed by selecting to the fixed value of the strains of the more compressed face of concrete $\varepsilon_{c(1)}$ the corresponding strains of the

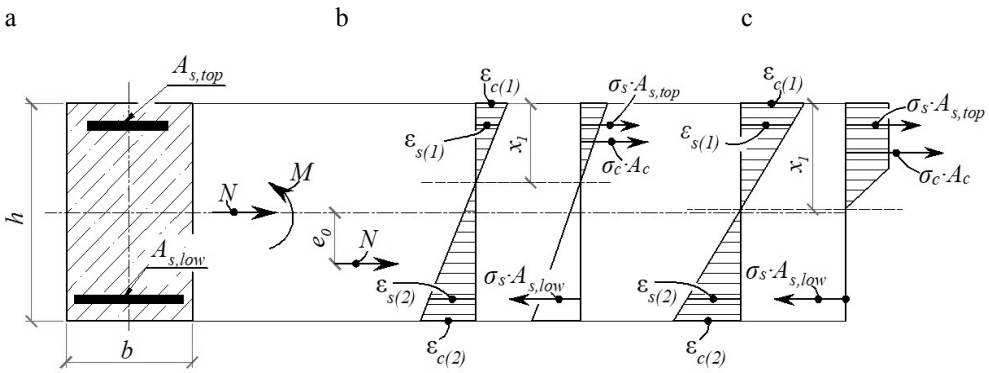

FIGURE 3. The scheme of efforts and the calculated schemes of stresses and strains at eccentric stretching of a reinforced concrete rod: a – cross section of the rod; b – with a triangular diagram of the compressed zone; c – with a trapezoidal diagram of the compressed zone

stretched face $\varepsilon_{c(2)}$, at which equilibrium occurs.

Selection is performed using a combination of numerical methods – methods of successive approximations, half division, secant. The selection step is accepted $0.01 \cdot \varepsilon_{c(1)}$ (in contrast to the step recommended $0.1 \cdot \varepsilon_{c(1)}$ in Appendix A of the DSTU B V.2.6-156:2010 standard). To determine the strength of the cross section, a state diagram "$N - \varepsilon_{c(1)}$" was constructed at characteristic points $\varepsilon_{c(1)}$, the maximum of which was equal to the maximum value of the longitudinal force N, perceived by the cross section.

The maximum value of the bending moment, which perceives the cross section at a given combination of external forces is determined by the formula:

$$M = N \cdot e_0 \tag{7}$$

At the above value of the strain step $\varepsilon_{c(1)}$, the diagram "$N - \varepsilon_{c(1)}$" must have 100 points. At each step $\varepsilon_{c(1)}$ in the selection of strains $\varepsilon_{c(2)}$, all other parameters of the SSS cross section (χ, x_1, σ_{si}) were calculated and then substituted into the first equation of the system – Eq. (1) or (6), while N assumed to be zero.

Next, the obtained value of the internal force N, which perceives the cross section, was multiplied by the eccentricity of external forces e_0. The resulting bending moment M was substituted into the second equation of the system – Eq. (1) or (6) and when the above SSS parameters of the cross section were calculated, the equilibrium was checked. Thus, in the chosen approach, the criterion for finding the equilibrium of the equations system (1) and (6) is the proximity to zero of the result of the second equation (equation of moments), namely the condition:

$$\sum M \le \Delta M \tag{8}$$

where ΔM is an error in solving a system of equations [kN·m].

Results and discussion

The authors consider two possible forms of equilibrium of reinforced concrete section under the action flat non-eccentric tension:

– non-eccentric tension with large eccentricities, the strains diagram is ambiguous, the work of the section is similar to that which bends (Fig. 4a);
– non-eccentric tension with small eccentricities – the line of action of the external tensile force is between the rods of the longitudinal reinforcement of the section, the section is almost completely stretched with a relatively small height of the compressed zone of concrete (Fig. 4b).

According to the first form of equilibrium of the experimental cross section (Fig. 4a) – under the action of external forces N = –2,000 kN, M = = 600 kN·m, e_0 = 30 cm, e_0/h = 1.5 (the line of action of the external force is outside the cross section) the equilibrium is at the characteristic points $\varepsilon_{c(1)}$ of the state diagram "$N - \varepsilon_{c(1)}$" (Fig. 5). The bearing capacity of the reinforced concrete section is – N_{max} = 169.5 kN, M_{max} = 50.03 kN·m.

If we consider the action of another combination of external forces N = = –2,000 kN, M = 120 kN·m, e_0 = 6.0 cm, e_0/h = 0.3 (under the action of reduced by 5 times M), there is a second form of equilibrium (Fig. 4b) at cross section.

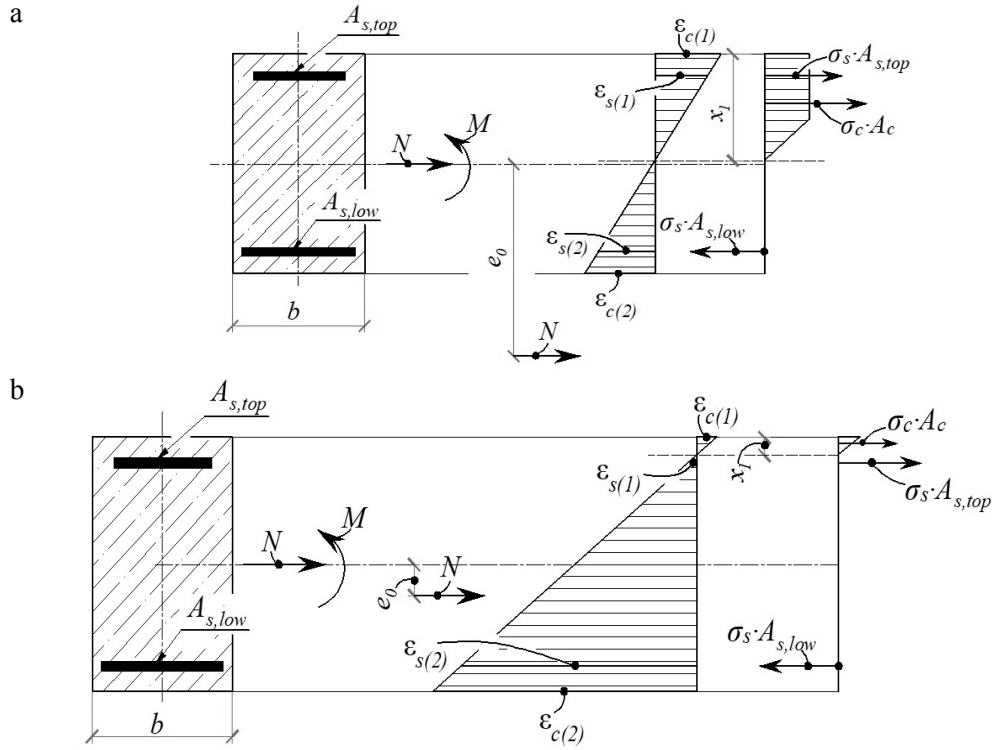

FIGURE 4. The scheme of efforts and forms of equilibrium under the non-eccentric tension of reinforced concrete section: a – with large eccentricities; b – with small eccentricities

To more clearly display the results of calculations using the algorithm under consideration, the graphs of dependence on the values $\sum M$ of strains of the more tension section face $\varepsilon_{c(2)}/\varepsilon_{c,\max}$, which correspond to the values of the more compressed section face $\varepsilon_{c(1)}$, are constructed. The values $\varepsilon_{c,\max}$ correspond to the largest values of tensile strains $\varepsilon_{c(2)}$, at which there is a rupture of the reinforcement in the tensioned zone of concrete.

According to the data obtained with this combination of efforts, the equilibrium is also established (graph $\sum M$ of $\varepsilon_{c(2)}/\varepsilon_{c,\max}$ the intersection of the abscissa) at all 100 characteristic points of the state diagram "$N - \varepsilon_{c(1)}$" (Fig. 7), even at the highest values $\varepsilon_{c(1)} = \varepsilon_{cu,3d}$ (at values $\varepsilon_{c(2)}$ close to the maximum $\varepsilon_{c,\max}$ – Fig. 6, Curve 1).

The bearing capacity of the section is $N_{\max} = 484.3$ kN, $M_{\max} = 29.06$ kN·m.

With a further decrease in the value of the external moment, with a combination of external forces $N = -2{,}000$ kN, $M = 30$ kN·m, $e_0 = 1.5$ cm, $e_0/h = 0.075$ cm, the equilibrium is no longer at all points of the diagram "$N - \varepsilon_{c(1)}$".

In this case, when $\varepsilon_{c(1)} = \varepsilon_{cu,3d}$ and $\varepsilon_{c(1)} = 0.8 \cdot \varepsilon_{cu,3d}$ the graph $\sum M$ of the dependence $\varepsilon_{c(2)}/\varepsilon_{c,\max}$ does not intersect the abscissa axis (Fig. 8, Curves 1, 2). The equilibrium is starting from $\varepsilon_{c(1)} = 0.56 \cdot \varepsilon_{cu}$.

In Figure 9 section of the descending branch of the diagram at values $\varepsilon_{c(1)} > 1.7 \cdot 10^{-3}$ corresponds to the values of strains $\varepsilon_{c(1)}$, in which the search for equilibrium between external and internal forces occurs rupture of the reinforcement in the tensioned zone, i.e. the equations system (1) or (6) has no solution.

Comparing the state diagrams of the cross section "$N - \varepsilon_{c(1)}$" at different eccentricities e_0 of external load application (Figs. 5, 7, 9), it should be noted that when the eccentricity for the experimental reinforced concrete section decreases, the length of the inclined section

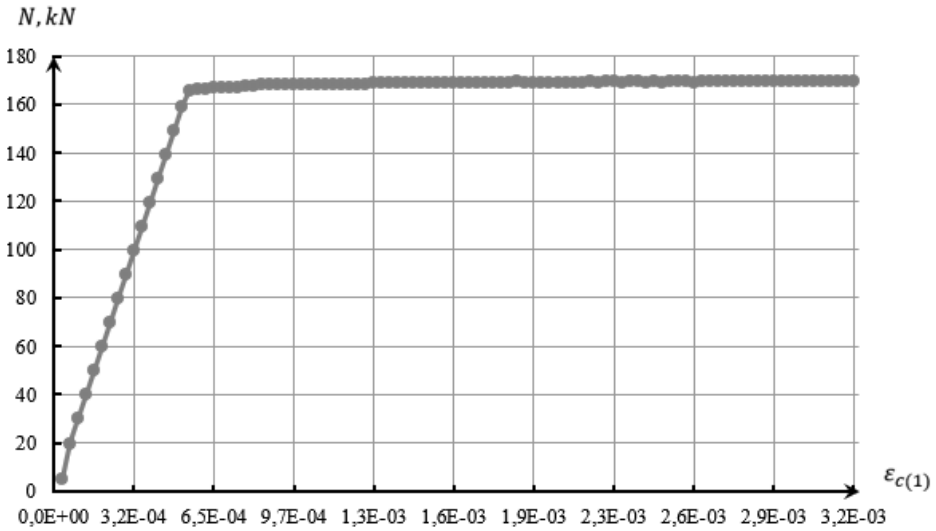

FIGURE 5. State diagram "$N - \varepsilon_{c(1)}$" of the experimental section at $e_0 = 30$ cm

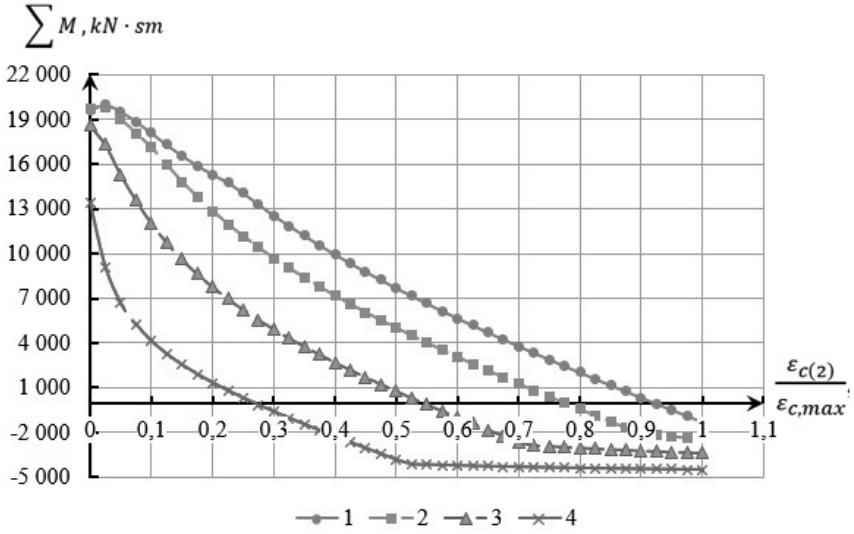

FIGURE 6. Graphs $\sum M$ of dependence on $\varepsilon_{c(2)}/\varepsilon_{c,\max}$ values, when e_0 = 6.0 cm: 1 – at $\varepsilon_{c(1)} = \varepsilon_{cu,3d}$; 2 – at $\varepsilon_{c(1)} = 0.8 \cdot \varepsilon_{cu,3d}$; 3 – at $\varepsilon_{c(1)} = 0.5 \cdot \varepsilon_{cu,3d}$; 4 – at $\varepsilon_{c(1)} = 0.2 \cdot \varepsilon_{cu,3d}$

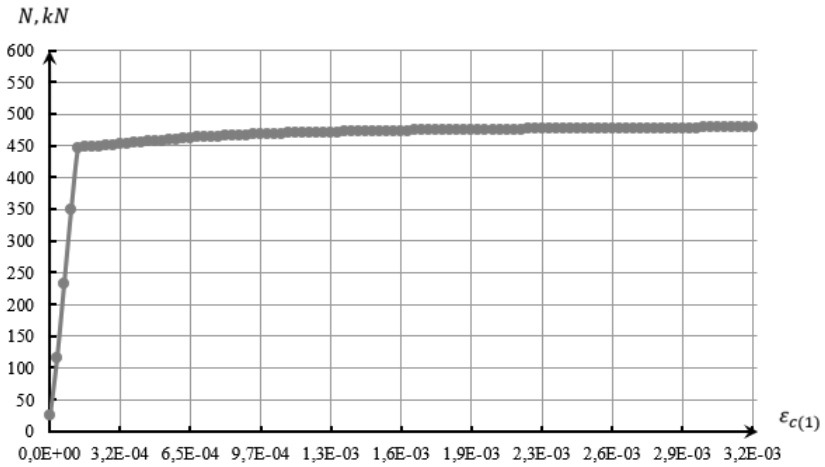

FIGURE 7. State diagram "$N - \varepsilon_{c(1)}$" of the experimental reinforced concrete section at e_0 = 6.0 cm

decreases until its complete disappearance. So at eccentricity e_0 = 30 cm its length makes from $\varepsilon_{c(1)} = 0$ to $\varepsilon_{c(1)} = 5.9 \cdot 10^{-4}$; when e_0 = 6.0 cm – from $\varepsilon_{c(1)} = 0$ to $\varepsilon_{c(1)} = 1.029 \cdot 10^{-4}$. At eccentricity e_0 = = 1.5 cm, it is absent in general.

Also, when the external eccentricity decreases e_0 (reduction of the bending moment M at a constant longitudinal force N), the value $\varepsilon_{c(1)}$ at which the chosen system of equations has a solution decreases, i.e. the maximum relative deformations of compressed concrete $\varepsilon_{c(1)}$ decrease by force. This is fully consistent with the physical picture of the experimental process – with increasing

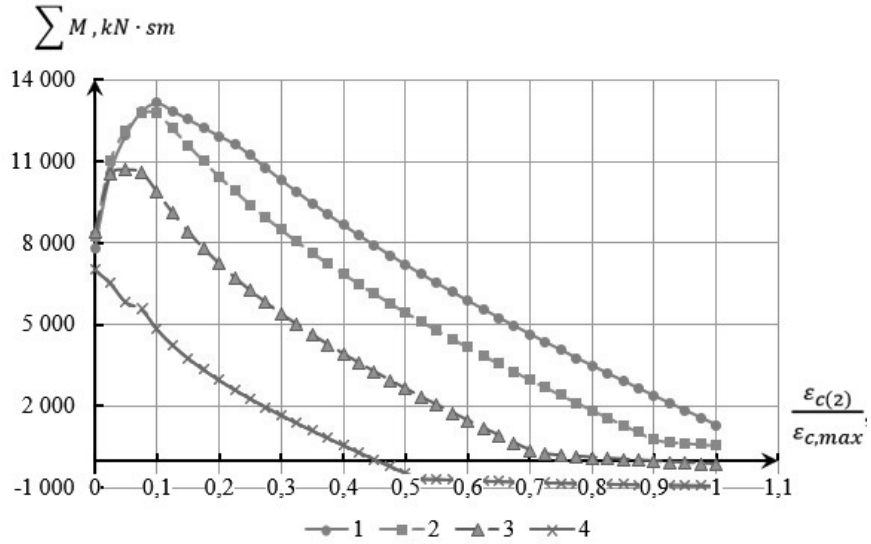

FIGURE 8. Graphs $\sum M$ of dependence on $\varepsilon_{c(2)}/\varepsilon_{c,\max}$ values, when e_0 = 1.5 cm: 1 – at $\varepsilon_{c(1)} = \varepsilon_{cu,3d}$; 2 – at $\varepsilon_{c(1)} = 0.8 \cdot \varepsilon_{cu,3d}$; 3 – at $\varepsilon_{c(1)} = 0.5 \cdot \varepsilon_{cu,3d}$; 4 – at $\varepsilon_{c(1)} = 0.2 \cdot \varepsilon_{cu,3d}$

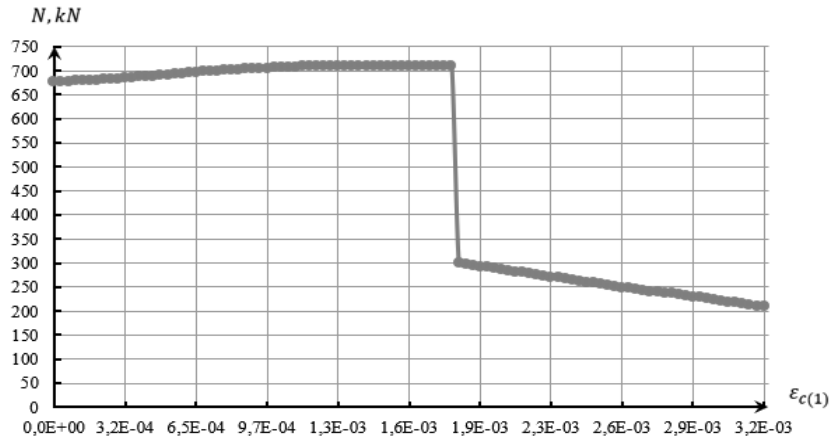

FIGURE 9. State diagram "$N - \varepsilon_{c(1)}$" of the experimental reinforced concrete section at e_0 = 1.5 cm

external tensile force N, the tensioned cross-sectional area increases, the impact of compressed concrete on the overall cross-sectional strength decreases.

If we continue to gradually reduce the eccentricity e_0 of the external forces application, the number of characteristic points $\varepsilon_{c(1)}$ at which the equilibrium will be in the cross section will also decrease. The results of experimental cross sections calculations are presented in Table 2. But even at sufficiently small values e_0, close to the transition limit of SSS cross section from non-eccentric tension with small eccentricities to central tensile using the method presented in Appendix A

TABLE 2. The results of numerical calculations of experimental reinforced concrete sections

Geometric cross-sectional dimensions $b \times h$ [cm]	External efforts			Curvature χ [cm^{-1}]	Strains $\varepsilon_{c(1)}$ (equilibrium)	Compressed cross-sectional area height x [cm]	Upper reinforcement $\sigma_{s,top}$ [MPa]	Lower reinforcement $\sigma_{s,low}$ [MPa]	Bearing capacity of section		ρ [%]
	M [kN·m]	N [kN]	e_0 [cm]						N_{int} [kN]	M_{int} [kN·m]	
20 × 100	600	–2 000	30	1.15E-03	$1.0 \cdot \varepsilon_{cu}$	2.81	–45.8	–364.0	169.5	50.85	1.3
	300	–2 000	15	1.27E-03	$1.0 \cdot \varepsilon_{cu}$	2.54	–122.5	–364.0	284.2	42.63	1.3
	150	–2 000	7.5	1.43E-03	$1.0 \cdot \varepsilon_{cu}$	2.25	–224.4	–364.0	429.5	32.21	1,3
	75	–2 000	3.75	1.60E-03	$1.0 \cdot \varepsilon_{cu}$	2.01	–332.5	–364.0	577.0	21.64	1.3
	50	–2 000	2.5	1.40E-03	$0.86 \cdot \varepsilon_{cu}$	1.73	–364.0	–364.0	647.9	16.20	1.3
	40	–2 000	2	1.59E-03	$0.7 \cdot \varepsilon_{cu}$	1.44	–364.0	–364.0	678.5	13.57	1.3
	30	–2 000	1.5	1.56E-03	$0.56 \cdot \varepsilon_{cu}$	1.16	–364.0	–364.0	711.2	10.67	1.3
	20	–2 000	1	1.54E-03	$0.41 \cdot \varepsilon_{cu}$	0.86	–364.0	–364.0	746.1	7.46	1.3
	10	–2 000	0.5	1.49E-03	$0.25 \cdot \varepsilon_{cu}$	0.54	–364.0	–364.0	783.4	3.92	1.3
	5	–2 000	0.25	1.47E-03	$0.17 \cdot \varepsilon_{cu}$	0.37	–364.0	–364.0	803.0	2.01	1.3
	1	–2 000	0.05	1.23E-03	$0.07 \cdot \varepsilon_{cu}$	0.18	–364.0	–364.0	819.2	0.41	1.3
	0.5	–2 000	0.025	1.25E-03	$0.05 \cdot \varepsilon_{cu}$	0.13	–364.0	–364.0	821.3	0.21	1.3

TABLE 2, cont.

Geometric cross-sectional dimensions $b \times h$ [cm]	External efforts			Curvature χ [cm^{-1}]	Strains $\varepsilon_{c(1)}$ (equilibrium)	Compressed cross-sectional area height x [cm]	Upper reinforcement $\sigma_{s,top}$ [MPa]	Lower reinforcement $\sigma_{s,low}$ [MPa]	Bearing capacity of section		ρ [%]
	M [kN·m]	N [kN]	e_0 [cm]						N_{int} [kN]	M_{int} [kN·m]	
16 × 100	600	–2 000	30	1.32E-03	$1.0 \cdot \varepsilon_{cu}$	2.44	–154.8	–364.0	81.5	24.46	1.0
	300	–2 000	15	1.42E-03	$1.0 \cdot \varepsilon_{cu}$	2.27	–219.0	–364.0	141.6	21.24	1.0
	150	–2 000	7.5	1.57E-03	$1.0 \cdot \varepsilon_{cu}$	2.05	–312.5	–364.0	224.7	16.85	1.0
	75	–2 000	3.75	2.11E-03	$1.0 \cdot \varepsilon_{cu}$	1.53	–364.0	–364.0	312.6	11.72	1.0
	50	–2 000	2.5	2.10E-03	$0.76 \cdot \varepsilon_{cu}$	1.17	–364.0	–364.0	354.7	8.87	1.0
	30	–2 000	1.5	2.01E-03	$0.51 \cdot \varepsilon_{cu}$	0.82	–364.0	–364.0	395.7	5.94	1.0
	20	–2 000	1	2.00E-03	$0.38 \cdot \varepsilon_{cu}$	0.62	–364.0	–364.0	419.2	4.19	1.0
	10	–2 000	0.5	1.97E-03	$0.24 \cdot \varepsilon_{cu}$	0.393	–364.0	–364.0	444.9	2.22	1.0
	5	–2 000	0.25	1.83E-03	$0.16 \cdot \varepsilon_{cu}$	0.283	–364.0	–364.0	458.7	1.15	1.0
	1	–2 000	0.05	1.72E-03	$0.07 \cdot \varepsilon_{cu}$	0.13	–364.0	–364.0	470.2	0.24	1.0
	0.5	–2 000	0.025	1.75E-03	$0.05 \cdot \varepsilon_{cu}$	0.092	–364.0	–364.0	471.72	0.12	1.0
12 × 100	600	–2 000	30	2.44E-03	$1.0 \cdot \varepsilon_{cu}$	1.33	–364.0	–364.0	25.0	7.49	0.5
	300	–2 000	15	2.82E-03	$1.0 \cdot \varepsilon_{cu}$	1.15	–364.0	–364.0	43.8	6.57	0.5
	150	–2 000	7.5	3.05E-03	$0.86 \cdot \varepsilon_{cu}$	0.91	–364.0	–364.0	70.0	5.25	0.5
	75	–2 000	3.75	2.98E-03	$0.61 \cdot \varepsilon_{cu}$	0.66	–364.0	–364.0	98.9	3.71	0.5
	50	–2 000	2.5	2.93E-03	$0.48 \cdot \varepsilon_{cu}$	0.53	–364.0	–364.0	114.3	2.86	0.5
	30	–2 000	1.5	2.82E-03	$0.35 \cdot \varepsilon_{cu}$	0.40	–364.0	–364.0	129.5	1.94	0.5
	20	–2 000	1	2.82E-03	$0.27 \cdot \varepsilon_{cu}$	0.31	–364.0	–364.0	140.0	1.40	0.5
	10	–2 000	0.5	2.63E-03	$0.18 \cdot \varepsilon_{cu}$	0.221	–364.0	–364.0	151.1	0.76	0.5
	5	–2 000	0.25	2.65E-03	$0.13 \cdot \varepsilon_{cu}$	0.159	–364.0	–364.0	157.2	0.39	0.5
	1	–2 000	0.05	2.74E-03	$0.06 \cdot \varepsilon_{cu}$	0.07	–364.0	–364.0	162.4	0.08	0.5
	0.5	–2 000	0.025	2.43E-03	$0.04 \cdot \varepsilon_{cu}$	0.053	–364.0	–364.0	163.118	0.04	0.5

of the DSTU B V.2.6-156:2010 standard, you can find a balance between external and internal forces and estimate the load-bearing capacity of the section, which is completely determined by the area and tensile strength of the reinforcement. But to successfully find a solution to the system of Eq. (1) or (6) you need to reduce the selection step from the recommended $\varepsilon_{c(1)} = 0.1 \cdot \varepsilon_{cu}$ to the smallest, for example, to $\varepsilon_{c(1)} = 0.01 \cdot \varepsilon_{cu}$.

An alternative option in this case may be to calculate the load-bearing capacity of the reinforced concrete section according to the formulas of the algorithm presented in the previous building codes, i.e. the SNiP 2.03.01-84* standard (Gosudarstvennyy stroitelnyy komitet SSSR [Gosstroy SSSR], 1989), which is based on the method of limiting forces. An additional argument in favor of the calculation of this option is its higher speed compared to the iterative algorithm of the deformation method, which may be useful when performing calculations of reinforcement of rectangular sections by the Wood–Armer method (Shin et al., 2009).

Conclusions

During performing calculations on the strength of normal sections by the deformation method of non-eccentrically tensioned elements of reinforced concrete structures with small eccentricities, an equilibrium was found between internal and external forces only with a two-digit diagram of the distribution of relative longitudinal strains (in the presence of a compressed zone availability).

It is established that with a decrease in the eccentricity of the application of force, the compressed zone of concrete in cross section decreases until its complete disappearance. The cross section of the reinforced concrete structure becomes completely tensioned. An equilibrium between external and internal forces cannot be found with the help of the deformation method realization, proposed in Appendix A of the DSTU B V.2.6-156:2010 standard.

Options for solving this task without significant loss of calculation accuracy are proposed, the most appropriate of which is the transition to the method of limiting forces (which was adopted as the main in previous building codes, i.e. the SNiP 2.03.01-84* standard) and further calculation by this method.

References

Babayev, V.M., Bambura, A.M., Pustovoitova, O.M. (2015). *Praktichnij rozrahunok elementiv zalizobetonnih konstrukcij za DBN V.2.6-98:2009 u porivnjanni z rozrahunkami za SNiP 2.03.01-84* i EN 1992-1-1 (Eurocode 2)* [*Practical calculation of elements of reinforced concrete structures according to DBN B.2.6-98: 2009 in comparison with calculations according to SNiP 2.03.01-84* and EN 1992-1-1 (Eurocode 2)*]. Kharkiv: Publishing Golden Pages.

Bambura, A.M., Pavlikov, A.M., Kolchunov, V.I., Kochkarev, D.V. & Yakovenko, I.A. (2017). *Praktichnij posibnik iz rozrahunku zalizobetonnih konstrukcij za dijuchimi normami Ukraïni (DBN V.2.6-98:2009) ta novimi modeljami deformuvannja, shho rozrobleni na ïhnju zaminu* [*Practical guide to the calculation of reinforced concrete structures – according to the current standards of Ukraine (DBN B.2.6-98:2009) and new models of deformation, designed to replace them*]. Kyiv: Publishing Toloka.

Dem'Yanov, A., Kolchunov, V., Iakovenko, I. & Kozarez, A. (2019). Load bearing capacity calculation of the system "reinforced concrete beam – deformable base" under torsion with bending. *E3S Web of Conferences*, *97*, 1-8. https://doi.org/10.1051/e3sconf/20199704059

Dem'Yanov, A.I., Yakovenko, I.A. & Kolchunov, V.I. (2017). The development of universal short dual-console element for resistance of reinforced concrete structures under the action torsion with bending. *Izvestiya Vysshikh Uchebnykh Zavedenii, Seriya Teknologiya Tekstil'noi Promyshlennosti*, *370*(4), 246-251.

Gosudarstvennyy stroitelnyy komitet SSSR [Gosstroy SSSR] (1989). *Betonnye i zhelezobetonnye konstrukcii* (SNiP 2.03.01-84*) [*Concrete and reinforced concrete structures. Building codes and regulations* (SNiP 2.03.01-84*)]. Moskva: CITP Gosstroya SSSR.

Iakovenko, I.A. & Kolchunov, V.I. (2017). The development of fracture mechanics hypotheses applicable to the calculation of reinforced concrete structures for the second group of limit states. *Journal of Applied Engineering Science*, *15*(3), 371-380. https://doi.org/10.5937/jaes15-14662

Iakovenko, I., Kolchunov, V. & Lymar, I. (2017). Rigidity of reinforced concrete structures in the presence of different cracks. *MATEC Web of Conferences*, *116*, 02016. EDP Sciences. https://doi.org/10.1051/matecconf/201711602016

Karpenko, N.I. (1996). *Obshhie modeli mehaniki zhelezobetona* [*General models of reinforced concrete mechanics*]. Moskva: Publishing Stroiizdat.

Karpiuk, V., Somina, Yu. & Antonova, D. (2019). Calculation models of the bearing capacity of span reinforced concrete structures support zones materials. *Science Forum: Actual Problems of Engineering Mechanics*, *968*, 209-226. https://doi.org/10.4028/www.scientific.net/MSF.968.209

Karpyuk, V.M., Kostyuk, A.I. & Semina, Yu.A. (2018). General case of nonlinear deformation-strength model of reinforced concrete structures. *Strength of Materials*, *50*(*3*), 453-464. https://doi.org/10.1007/s11223-018-9990-9

Kolchunov, V.I., Dem'yanov, A., Iakovenko, I. & Garba, M. (2018). Bringing the experimental data of reinforced concrete structures crack resistance in correspondence with their theoretical values. *Science & Construction*, *1*(15), 42-49.

Kolchunov, V.I. & Yakovenko, I.A. (2016). About the violation solid effect of reinforced concrete in reconstruction design of textile industry enterprises. *Izvestiya Vysshikh Uchebnykh Zavedenii. Teknologiya Tekstil'noi Promyshlennosti*, *2016*(3), 258-263.

Kolchunov, V.I., Yakovenko, I.A. & Dmitrenko, E.A. (2016). The analytical core model formation of the nonlinear problem bond armature with concrete. *Academic Journal. Industrial Machine Building, Civil Engineering*, *2*(47), 125-132.

Pavlikov, A., Kochkarev, D. & Harkava, O. (2019). Calculation of reinforced concrete members strength by new concept. In *Proceedings of the fib Symposium 2019: Concrete – Innovations in Materials, Design and Structures* (pp. 820-827). Lausanne: International Federation for Structural Concrete.

Shin, M., Bommer, A., Deaton, J. & Alemdar, B. (2009). Twisting moments in two-way slab. *Concrete International*, *78*, 35-40.

Ukrayinskyy naukovo-doslidnyy i navchalnyy tsentr problem standartyzatsiyi, sertyfikatsiyi ta yakosti [SE UkrNDNC] (2011a). *Betonni ta zalizobetonni konstrukciï. Osnovni polozhennja* (DBN V.2.6-98:2009) [*Concrete and reinforced concrete structures. Basic provisions* (DBN V.2.6-98:2009)]. Kyiv: Minrehionbud Ukrayiny.

Ukrayinskyy naukovo-doslidnyy i navchalnyy tsentr problem standartyzatsiyi, sertyfikatsiyi ta yakosti [SE UkrNDNC] (2011b). *Betonni ta zalizobetonni konstrukciï z vazhkogo betonu. Pravila proektuvannja* (DSTU B V.2.6-156:2010) [*Concrete and reinforced concrete structures with heavy weight structural concrete. Design rules* (DSTU B V.2.6--156:2010)]. Kyiv: Minrehionbud Ukrayiny.

Wojciechowski, O.V., Zhuravsky, O.D. & Baida, D.M. (2017). *Rozrahunok zalizobetonnih konstrukcij z vikoristannjam sproshhenih diagram deformuvannja materialiv (za DSTU B V.2.6-156:2010). Chastina 1. Rozrahunok za I grupoju granichnih staniv* [*Calcu-*

lation of reinforced concrete structures using simplified diagrams of deformation of materials (according to DSTU B V.2.6-156:2010). Part 1. Calculation of the 1st group of limit states]. Kyiv: Publishing KNUBA.

Summary

Strength of eccentrically tensioned reinforced concrete structures with small eccentricities by normal sections. It is implemented the method of normal rectangular sections slab (shell) reinforced concrete elements strength calculating with flat eccentric tensile strength using the deformation method. The results of the calculation are analyzed for the case of eccentric tension with small eccentricities with varying next parameters: the height of the cross section and the reinforcement coefficient. It is investigated the character of diagrams condition change of section "$N - \varepsilon_{c(1)}$" at gradual change of the stress-strain state from eccentric to the central tension. It is revealed that when the eccentricity of external forces decreases, the compressed zone of concrete decreases until its complete disappearance, and at rather small values of eccentricities of force application the balance between external and internal forces cannot be found by the method of current norms. An equilibrium is found between internal and external forces only at a two-digit diagram of the distribution of relative longitudinal deformations (in the case of a compressed zone). Variants of the given problem decision without considerable loss of calculations accuracy are offered, the most expedient of which is transition to algorithm of calculation by a method of limiting efforts. It was accepted as the basic in the previous building norms. The results of numerical calculations performed in the software complex "Lira-CAD" and the corresponding mathematical modeling confirmed the rationality and allowable accuracy of further calculations by this method.

Authors' address:
Yevhen Dmytrenko
(https://orcid.org/0000-0001-9737-943X)
National University of Life and Environmental Sciences of Ukraine
Faculty of Construction and Design
Construction Department
12B Heroiv Oborony Str., building 7, office 29,
03041 Kyiv
Ukraine
e-mail: zdmitrenko26@gmail.com

Ihor Yakovenko
(https://orcid.org/0000-0003-4256-9855)
National University of Life and Environmental Sciences of Ukraine
Faculty of Construction and Design
Construction Department
12B Heroiv Oborony Str., building 7, office 29,
03041 Kyiv
Ukraine
e-mail: i2103@ukr.net

Oleg Fesenko
(https://orcid.org/0000-0001-8154-2239)
The State Research Institute of Building Constructions
e-mail: oleg_for@ukr.net

Scientific Review – Engineering and Environmental Sciences (2021), 30 (3), 439–450
Sci. Rev. Eng. Env. Sci. (2021), 30 (3)
Przegląd Naukowy – Inżynieria i Kształtowanie Środowiska (2021), 30 (3), 439–450
Prz. Nauk. Inż. Kszt. Środ. (2021), 30 (3)
http://iks.pn.sggw.pl
DOI 10.22630/PNIKS.2021.30.3.37

Haider M. Al-JELAWY[1], Ayad Al-RUMAITHI[2], Aqeel T. FADHIL[2], Alaa J. NAJI[1]

[1] University of Al-Qadisiyah, College of Engineering
[2] University of Baghdad, College of Engineering

Mesoscale modeling of fracture in cement and asphalt concrete

Key words: mesoscale model, damage model, fracture energy, cement concrete, asphalt concrete, disk-shaped compact tension test

Introduction

Numerical modeling of concrete materials has taken several paths over the years. The most common method is macroscale modeling where concrete is modeled as a homogenous material. This type of modeling has two distinct approaches: continuum models and fiber-based models. Continuum models are the most commonly used type which utilize commercial finite element programs and they are computationally expensive. Fiber-based models, on the other hand, are less common and not computationally costly (Al-Jelawy, 2017; Haber, Mackie & Al-Jelawy, 2017; Al-Jelawy, Mackie & Haber, 2018). Recently, another type of modeling has emerged which is the mesoscale modeling.

Mesoscale modeling has become an alternative modeling method for macroscale modeling for the simulation of heterogeneous materials such as cement and asphalt concrete since realistic damage prediction and crack growth are crucial aspects of such materials (Unger, Eckardt & Kooenke, 2011; Thilakarathna, Baduge, Mendis, Vimonsatit & Lee, 2020). Mesoscale modeling in cement or asphalt concrete requires aggregate and mortar to be modeled as separate constituents. Sometimes an interfacial transition zone (ITZ) between the aggregate and mortar is modeled as a third material (Unger & Eckardt, 2011).

Heterogeneous material is created using image processing techniques or through random generation of aggregates. Aggregate can be rounded in shape or having sharp angles. Aggregate

size distribution is modeled through prescribed curves or empirical equations such as Fuller curve (Häfner, Eckardt, Luther & Kőnke, 2006; Zhang, Song, Liu, Wu & Song, 2017). Material models are then assigned to the aggregate and mortar based on their individual properties.

In previous studies, continuum models such as smeared crack models, damage models, and plastic-damage models were used to represent fracture properties within the numerical model (Unger & Eckardt, 2011). Also, models which utilized discrete cracks implemented in rigid-body-spring model were used (Grassl & Bažant, 2009), or discrete cracks which were included in finite elements such as extended finite elements (Moës, Dolbow & Belytschko, 1999).

Recently, the use of mesoscale modeling has been limited to simulate specimen subject to tension (Kim & Al-Rub, 2011; Unger & Eckardt, 2011; Unger et al., 2011; Chen, Xu, Mo & Zhou, 2018; Zhou & Lu, 2018; Karavelić, Nikolić, Ibrahimbegovic & Kurtović, 2019; Jin, Yu, Du & Yang, 2020) and compression (Xie, Guo, Yuan & Huang, 2015; Chen et al., 2018; Zhou & Lu, 2018; Karavelić et al., 2019; Chen et al., 2020). The use of fracture mechanics in civil engineering have restraints related to the selection of the test specimen geometry and the available equipment to run the test. The common specimen geometry used for concrete fracture testing is the three-point notched beam. Specimens extracted from the field have become more desirable in order to evaluate in situ structure capacity. Therefore, concrete cores are a suitable option for fracture testing since extracting beams from the field is difficult. Recently, geometry selection for concrete (Amirkhanian, Spring, Roesler & Paulino, 2016) was motivated by previous research on asphalt concrete specimens (Wagnoner, Buttlar & Paulino, 2005; Wagnoner, Buttlar, Paulino & Blankenship, 2006; Kim, Buttlar, Baek & Al-Qadi, 2009) where a disk-shaped compact tension test (DCT) was used extensively on asphalt core specimens that gave consistent and accurate results. Later the DCT geometry was adopted for asphalt specimens as a standard in ASTM D7313 (ASTM International [ASTM], 2013). The main advantage of the DCT specimen geometry is the easy fabrication from a field core or laboratory cylinder. Numerical studies that are performed on cement and asphalt DCT tests are mainly in macroscale (Wagnoner et al., 2005; Amirkhanian et al., 2016). Only one mesoscale study was conducted on mesoscale asphalt concrete specimens (Kim et al., 2009), while none were implemented on cement concrete DCT tests.

The objective of this study is to perform a mesoscale analysis on DCT specimens of cement concrete and asphalt concrete in order to obtain more realistic behavior of these heterogeneous materials. In mesoscale models, aggregate and matrix are represented as distinct materials and each material has its characteristic properties. Experimental data from previous studies on DCT specimens were used to validate the modeling results in terms of load-crack mouth opening displacement (CMOD) relationship.

Material models

Material models for fracture mechanics are mainly two types: constitutive models that represent cracks as a reduction in constitutive stiffness such as smeared crack model, damage models and damage-plasticity models. The other type of models such as embedded finite elements (Jirásek, 2000) and extended finite elements (Moës et al., 1999) utilizes a crack as a discontinuity in the displacement field. The first type of models has gained popularity due to its compatibility with finite element analysis (Rots, Nauta, Kuster Blaauwendraad, 1985; Rots, 1988; Rots & Blaauwendraad, 1989).

In the current study, isotropic damage model was used, and it is explained in the subsequent paragraphs. The softening curve for this model is defined as a function of fracture mechanics parameters.

This is the simplest form of damage models. It assumes that the damage is equal in all directions and represented by scalar value – ω (Kachanov, 1986; Lemaitre & Chaboche, 1990). The model is applied to the cementitious material only (such as cement mortar or asphalt) while the aggregate is modeled using its elastic properties.

The damage model is based on the following stress-strain relationship:

$$\sigma = \left(1 - \omega(\epsilon)\right) D\varepsilon \tag{1}$$

where D is the elastic material matrix. The damage (ω) can be defined as a function of fracture mechanics parameters as (Kurumatani, Terada, Kato, Kyoya & Kashiyama, 2016):

$$\omega(\epsilon) = \begin{cases} 1 - \frac{1}{E}\left(\frac{1}{\epsilon}\cdot\left(f_t - \left(f_t - \sigma_s\right)\cdot\frac{\left(\epsilon - \epsilon_0\right)}{w_s}\right)\right), \\ \text{if } \left(\epsilon - \epsilon_0\right) < w_s \\ 1 - \frac{1}{E}\left(\frac{1}{\epsilon}\cdot\left(\sigma_s \cdot\left(w_c - \frac{\left(\epsilon - \epsilon_0\right)}{w_c - w_s}\right)\right)\right), \\ \text{if } \left(\epsilon - \epsilon_0\right) \geq w_s \text{ and } \left(\epsilon - \epsilon_0\right) < w_c \\ 1, \quad \left(\epsilon - \epsilon_0\right) \geq w_c \end{cases} \tag{2}$$

Equation (2) is for bilinear softening, other softening types have different equations. The damage (ω) is zero if $\epsilon < \epsilon_0$.

Where:

- E – elastic modulus of the concrete or asphalt mortar material,
- f_t – uniaxial tensile strength of the concrete or asphalt mortar material,
- σ_s – stress at the point of slope change of bilinear softening curve, $\sigma_s = 0.25\, f_t$,
- w_s – damage at the point of slope change of bilinear softening curve, $w_s = 0.15\, w_c$.
- w_c – damage occurs at critical crack width. It can be defined as:

$$w_c = 5\frac{G_f}{hf_t} \tag{3}$$

Where G_f is the total fracture energy of the mortar material and h is equivalent element size defined as:

$$h = \sqrt{A_e} \tag{4}$$

for quadratic elements and:

$$h = \sqrt{2A_e} \tag{5}$$

for triangular element where A_e is the element area. ϵ_0 is the cracking strain and defined as:

$$\epsilon = \frac{f_t}{E} \tag{6}$$

ϵ is the highest equivalent strain the material ever experienced and related to equivalent strain ε_{eq} in case of loading and unloading as:

$$\varepsilon_{eq} > \epsilon \Rightarrow \epsilon = \varepsilon_{eq} \text{ (loading)} \tag{7}$$

$$\varepsilon_{eq} \leq \epsilon \Rightarrow \epsilon = \epsilon \text{ (unloading)} \tag{8}$$

Equivalent strain is defined as:

$$\varepsilon_{eq} = \sqrt{\varepsilon_{1b}^2 + \varepsilon_{2b}^2} \tag{9}$$

Where:

$$\varepsilon_{1b} = \varepsilon_1 \text{ if } \varepsilon_1 > 0 \text{ otherwise } \varepsilon_{1b} = 0 \tag{10}$$

$$\varepsilon_{2b} = \varepsilon_2 \text{ if } \varepsilon_2 > 0 \text{ otherwise } \varepsilon_{2b} = 0 \tag{11}$$

Where ε_1 and ε_2 are major and minor principal strains. It has been shown that isotropic damage model has low mesh sensitivity than other models such as smeared crack models (Kurumatani et al., 2016).

Geometry generation

To obtain a realistic representation of the concrete structure, the shape and size distribution of aggregate are described using a grading curve. Grading curves can be obtained using empirical equations such as Fuller curve. In the current study, Fuller curve was used which is in the following form:

$$passing = \left(\frac{d}{d_{\max}}\right)^{\alpha} \cdot 100 \tag{11}$$

where

d – sieve size [mm],
$d_{\max}$ – maximum size of aggregate [mm],
passing – accumulated percentage that pass the sieve size [%],
α – Fuller curve exponent and assumed to equals to 0.45 in the current study. Figure 1a shows an example of actual and simulated aggregate distribution using Fuller curve.

After that, ellipsoids are generated in three-dimensional domain (refer to Fig. 1b). Each individual ellipsoid has dimensions which are determined from the sieve curve and aspect ratio of the required aggregate. Aggregates are placed according to algorithm commonly known as set and place method which is explained by Unger et al. (2011). Based on this algorithm, the particles are divided into sets based on their sizes and then placed individually. If the placed particle intersects with another particle it will be placed again in a different empty spot. After particle placement was done, the ellipsoids were cut by a plane to obtain ellipses to shift the focus on two dimensional problems (refer to Fig. 1c). The cutting plane is located in the middle of width direction to avoid underrepresentation of larger particles near the edges of the specimen. Afterwards, specimen was

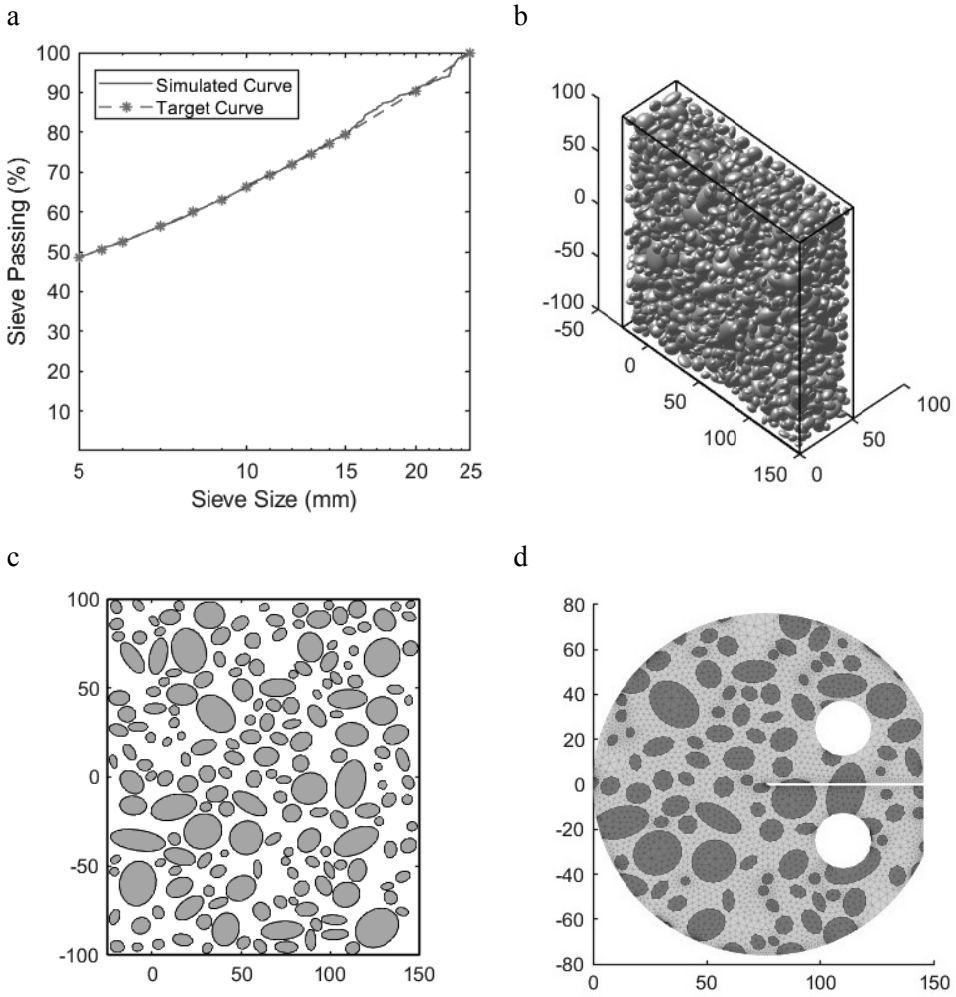

FIGURE 1. Geometry generation steps: a – sieve analysis; b – ellipsoids; c – ellipses; d – mesh

cut to form a disk-shaped geometry similar to that used in DCT test and a notch was made (see Fig. 1d). The ellipses were allowed to be cut at the boundaries to simulate in-situ conditions. Triangular mesh based on Delaunay triangulation was generated using MESH2D MATLAB code for two-dimensional geometries (Engwirda, 2005, 2014).

Numerical solution method

Cement and asphalt concrete tests were simulated using finite element method, and the triangular mesh was modeled as constant strain triangles elements. The applied load was vertical static support displacement through the circular holes with additional horizon-

tal support to ensure translational and rotation stability. The non-linear behavior was solved using Newton Raphson method with line searches implemented in MATLAB. The analysis results were compared with available experimental data in subsequent sections.

Model validation with Portland cement concrete experiments

The numerical model was validated against experimental tests of disk-shaped tension tests of concrete specimens. The selected specimens were tested by Amirkhanian et al. (2016). The material average properties are given in Table 1. They were 24 cored specimens, 18 specimens were tested at age 710 days (referred to as Mortar 1 in Table 1) and 6 specimens were tested at 1,578 days (Mortar 2 in Table 1). The averaged curves of the two types of the specimens were used in the comparisons with the numerical model.

Limestone coarse aggregate was used in all specimens with grading size of 5–20 mm. The percentage of coarse and fine aggregate was assumed 75% by volume. Fuller curve exponent of 0.45 was adopted. Aggregate distribution for the two types of specimens (Mortar 1 and Mortar 2) is shown in Figure 2a and Figure 3a, respectively. Disk geometry for the two types of specimens is shown in Figure 2b and Figure 4b, respectively. Crack growth from numerical simulation is shown in Figure 2c and Figure 3c for the two types. It can be observed that crack initiation and propagation are more realistic than straight cracks in macroscale models. The relationship between load and CMOD for the two types of specimens from numerical analysis is comparable to that from the experiments as depicted in Figure 2d and Figure 3d, respectively. The numerical model is able to predict the tensile strength, initial stiffness and the softening branch of load-CMOD curve with good accuracy.

TABLE 1. Material properties for cement concrete specimen

	E [MPa]	v	f_t [MPa]	G_f [N·mm^{-1}]
Aggregate	45 000	0.2	–	–
Mortar 1	38 000*	0.2	4**	0.15**
Mortar 2	38 000*	0.2	4.62***	0.163***

*Mortar modulus of elasticity was chosen in order to achieve bulk modulus of elasticity 40,600 MPa by using the following equation based on Reuss formula (Reuss, 1929):

$$E_{\text{bulk}} = \frac{100}{\frac{\%\ \text{aggregate}}{E\ \text{aggregate}} + \frac{\%\ \text{mortar}}{E\ \text{mortar}}} \quad (12).$$

**Tensile strength in macroscale model was 4 MPa and fracture energy is 0.1252 MPa.

***Tensile strength in macroscale model was 4.2 MPa and fracture energy is 0.148 MPa.

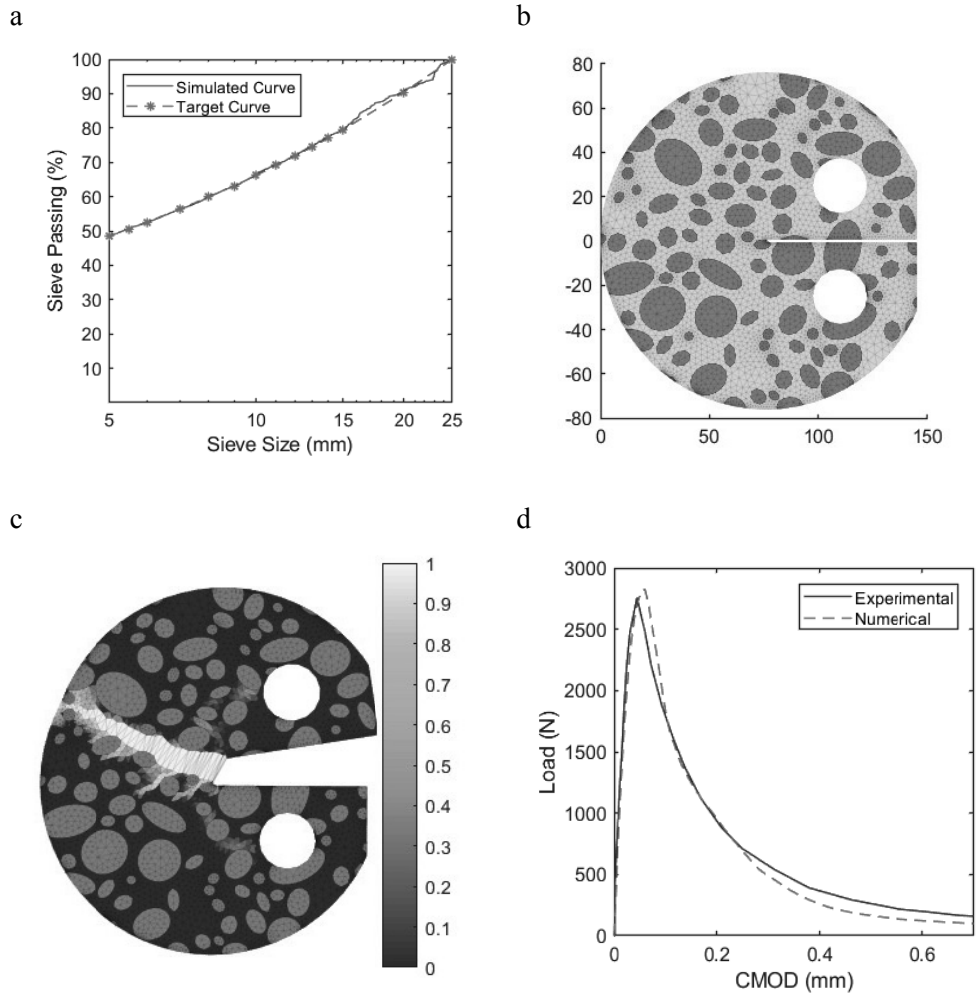

FIGURE 2. Model validation for cement concrete DCT (Mortar 1) specimens: a – sieve analysis; b – cement concrete mesh (7,028 elements); c – crack path at failure; d – load-CMOD curves

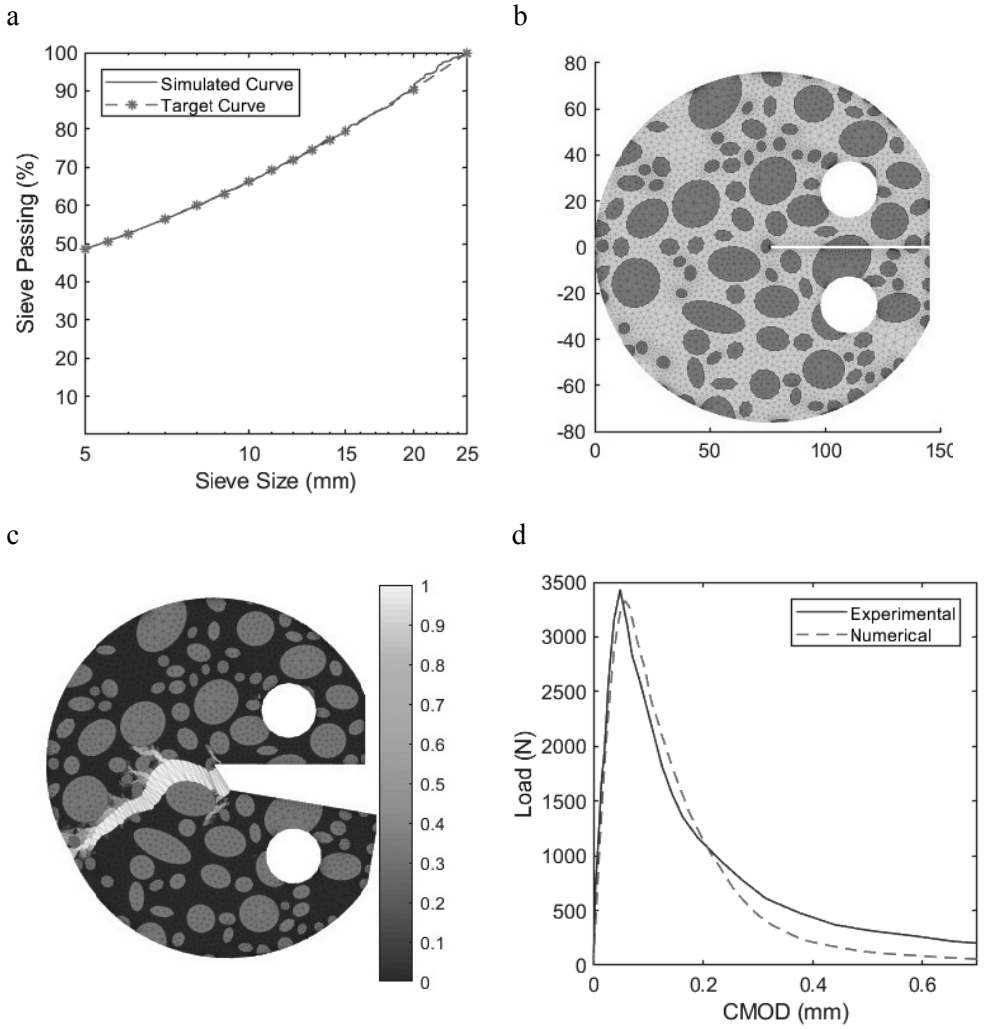

FIGURE 3. Model validation for cement concrete DCT (Mortar 2) specimens: a – sieve analysis; b – cement concrete mesh (8,082 elements); c – crack path at failure; d – load-CMOD curves

Comparisons with asphalt concrete experiments

In addition to the concrete specimens, of disk-shaped tension tests of asphalt specimens were used to validate the proposed numerical model. Three specimens were tested by Wagnoner et al. (2005). One mix was used with aggregate of grading size of 5–9.5 mm and an asphalt binder. Percentage of aggregate was assumed to be 90% by volume. Fuller curve exponent of 0.45 was adopted. Aggregate distribution of the

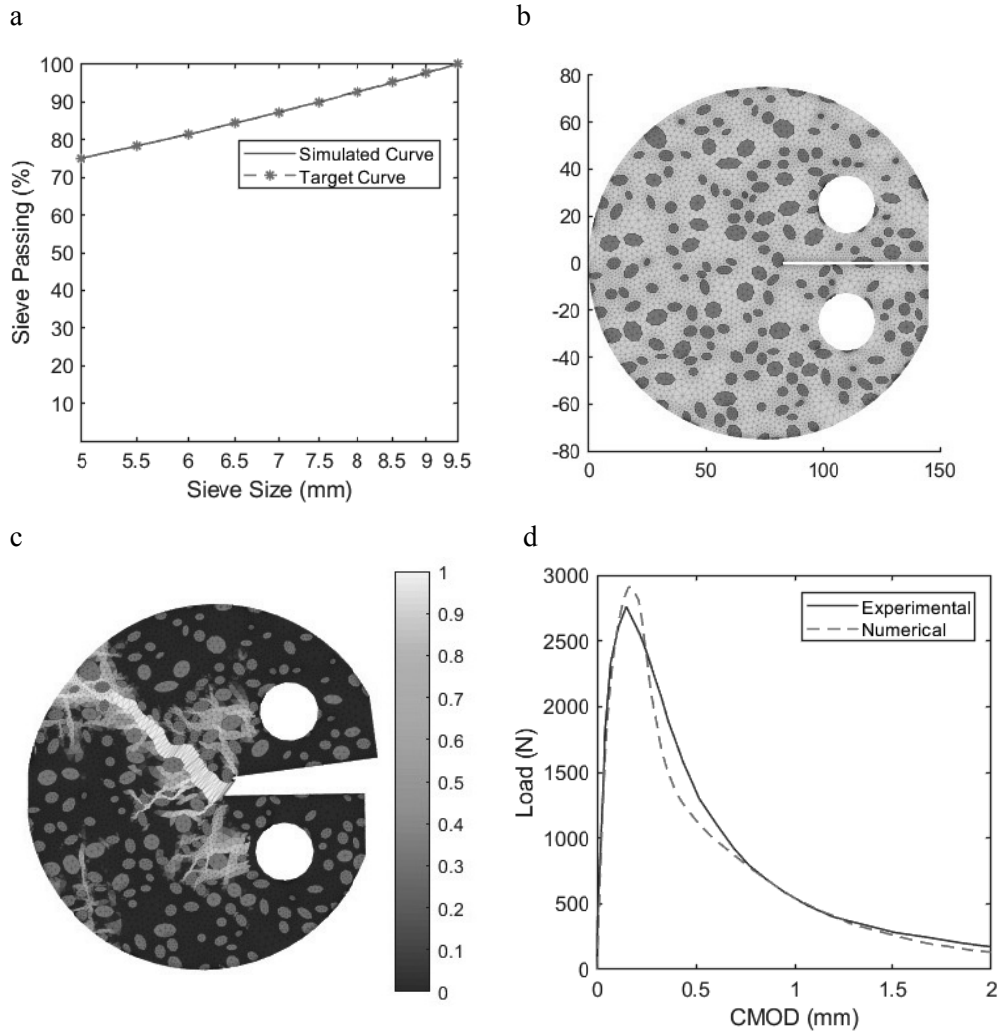

FIGURE 4. Model validation for asphalt concrete DCT specimens: a – sieve analysis; b – asphalt concrete mesh (14,708 elements); c – crack path at failure; d – load-CMOD curves

specimens is shown in Figure 4a. Disk geometry of specimens is shown in Figure 4b. The failure mode of the specimen from the numerical modeling is shown in Figure 4c. It can be seen that crack initiation and propagation are similar to that in an actual asphalt concrete specimen. Also, the numerical load-CMOD curve is in agreement with the experimental curve as depicted in Figure 4d. The predicted tensile strength, initial stiffness and the softening branch of load-CMOD curve are comparable to the experimental results.

TABLE 2. Material properties for asphalt concrete specimen

Material	E [MPa]	v	f_t [MPa]	G_f [N·mm^{-1}]
Aggregate	50 000	0.2	–	–
Mastic	12 000*	0.35	2.85**	0.459**

*Mastic modulus of elasticity was chosen in order to achieve bulk modulus of elasticity 14,200 MPa by using the following equation based on Reuss formula (Reuss, 1929):

$$E_{\text{bulk}} = \frac{100}{\frac{\%\ \text{aggregate}}{E\ \text{aggregate}} + \frac{\%\ \text{mastic}}{E\ \text{mastic}}} \quad (13).$$

**Tensile strength chosen 80% of indirect tensile splitting test results, while in the macroscale model of the original paper it was 74%. Fracture energy value in macroscale model is 0.328.

Conclusions

In this study, mesoscale modeling is performed on fracture behavior of cement and asphalt concrete composites using disk-shaped compact tension (DCT) tests. Realistic behavior of composite and heterogeneous materials such as cement and asphalt concrete require mesoscale modeling. In the presented model, aggregate and matrix (cement mortar or asphalt) are represented as distinct materials and each material has its characteristic properties where the matrix is modeled using isotropic damage model with softening and the aggregate is modeled using its elastic properties. Disk-shaped compact tension test is a better alternative to other tests such as three points bending tests for the determination of tensile strength and fracture energy of materials because it is more convenient for both field and laboratory specimens in addition to its accurate results. The test geometry is generated using a MATLAB code that takes care of the shape and size distribution of the aggregate. The numerical results show that the predicted load-CMOD curves are in good agreement with the experimental curves for both cement and asphalt concrete. Also, the numerical model can capture the variability of crack direction very well.

References

Al-Jelawy, H. (2017). *Shifted plastic hinge column connections using grouted sleeves for accelerated bridge construction* (doctoral dissertation). University of Central Florida, Orlando (FL).

Al-Jelawy, H.M., Mackie, K.R. & Haber, Z.B. (2018). Shifted plastic hinging for grouted sleeve column connections. *ACI Structural Journal*, *115*(4), 1101-1114.

Amirkhanian, A.N., Spring, D.W., Roesler, J.R. & Paulino, G.H. (2016). Forward and inverse analysis of concrete fracture using the disk-shaped compact tension test. *Journal of Testing and Evaluation*, *44*(1), 625-634.

ASTM International [ASTM] (2013). *Standard method for determining fracture energy of asphalt-aggregate mixtures using the disk--shaped compact tension geometry* (ASTM D7313-13). West Conshohocken (PA): ASTM International.

Chen, H., Xu, B., Mo, Y.L. & Zhou, T. (2018). Behavior of meso-scale heterogeneous concrete under uniaxial tensile and compressive loadings. *Construction and Building Materials*, *178*, 418-431.

Chen, H., Xu, B., Wang, J., Zhou, T., Nie, X. & Mo, Y.L. (2020). Parametric analysis on compressive strain rate effect of concrete using mesoscale modeling approach. *Construction and Building Materials*, *246*, 118375. https://doi.org/10.1016/j.conbuildmat.2020.118375

Engwirda, D. (2005). *Unstructured mesh methods for the Navier-Stokes equations* (undergraduate thesis). The University of Sydney, Sydney.

Engwirda, D. (2014). *Locally optimal Delaunay-refinement and optimisation-based mesh generation* (doctoral dissertation). The University of Sydney, Sydney.

Grassl, P. & Bažant, Z.P. (2009). Random lattice-particle simulation of statistical size effect in quasi-brittle structures failing at crack initiation. *Journal of Engineering Mechanics*, *135*(2), 85-92.

Haber, Z.B., Mackie, K.R. & Al-Jelawy, H.M. (2017). Testing and analysis of precast columns with grouted sleeve connections and shifted plastic hinging. *Journal of Bridge Engineering*, *22*(10), 04017078. https://doi.org/10.1061/(ASCE)BE.1943-5592.0001105

Häfner, S., Eckardt, S., Luther, T. & Könke, C. (2006). Mesoscale modeling of concrete: geometry and numerics. *Computers & Structures*, *84*(7), 450-461.

Jin, L., Yu, W., Du, X. & Yang, W. (2020). Mesoscale simulations of size effect on concrete dynamic splitting tensile strength: influence of aggregate content and maximum aggregate size. *Engineering Fracture Mechanics*, *230*, 106979. https://doi.org/10.1016/j.engfracmech.2020.106979

Jirásek, M. (2000). Comparative study on finite elements with embedded discontinuities. *Computer Methods in Applied Mechanics and Engineering*, *188*(1-3), 307-330.

Kachanov, L. (1986). *Introduction to continuum damage mechanics*. Berlin: Springer Science & Business Media.

Karavelić, E., Nikolić, M., Ibrahimbegovic, A. & Kurtović, A. (2019). Concrete meso-scale model with full set of 3D failure modes with random distribution of aggregate and cement phase. Part I: formulation and numerical implementation. *Computer Methods in Applied Mechanics and Engineering*, *344*, 1051-1072.

Kim, M., Buttlar, W.G., Baek, J. & Al-Qadi, I.L. (2009). Field and laboratory evaluation of fracture resistance of illinois hot-mix asphalt overlay mixtures. *Transportation Research Record*, *2127*(1), 146-154.

Kim, S.M. & Al-Rub, R.K.A. (2011). Meso-scale computational modeling of the plastic-damage response of cementitious composites. *Cement and Concrete Research*, *41*(3), 339-358.

Kurumatani, M., Terada, K., Kato, J., Kyoya, T. & Kashiyama, K. (2016). An isotropic damage model based on fracture mechanics for concrete. *Engineering Fracture Mechanics*, *155*, 49-66.

Lemaitre, J. & Chaboche, J.L. (1994). *Mechanics of solid materials*. Cambridge: Cambridge University Press.

Moës, N., Dolbow, J. & Belytschko, T. (1999). A finite element method for crack growth without remeshing. *International Journal for Numerical Methods in Engineering*, *46*(1), 131-150.

Reuss, A. (1929). Calculation of the yield point of mixed crystals. *Journal of Applied Mathematics and Mechanics*, *9*(1), 49-58.

Rots, J.G. (1988). *Computational modeling of concrete fracture*. Delft: Technische Hogeschool Delft.

Rots, J.G. & Blaauwendraad, J. (1989). Crack models for concrete, discrete or smeared? Fixed, multi-directional or rotating? *HERON*, *34*(1), 1989.

Rots, J.G., Nauta, P., Kuster, G.M.A. & Blaauwendraad, J. (1985). Smeared crack approach and fracture localization in concrete. *HERON*, *30*(1), 1985.

Thilakarathna, P.S.M., Baduge, K.K., Mendis, P., Vimonsatit, V. & Lee, H. (2020). Mesoscale modelling of concrete – a review of geometry generation, placing algorithms, constitutive relations and applications. *Engineering Fracture Mechanics*, *231*, 106974. https://doi.org/10.1016/j.engfracmech.2020.106974

Unger, J.F. & Eckardt, S. (2011). Multiscale modeling of concrete. *Archives of Computational Methods in Engineering*, *18*(3), 341-393.

Unger, J.F., Eckardt, S. & Kooenke, C. (2011). A mesoscale model for concrete to simulate mechanical failure. *Computers & Concrete*, *8*(4), 401-423.

Wagnoner, M.P., Buttlar, W. & Paulino, G.H. (2005). Disk-shaped compact tension test for asphalt concrete fracture. *Experimental Mechanics*, *45*(3), 270-277.

Wagnoner, M.P., Buttlar, W.G., Paulino, G.H. & Blankenship, P. (2006). Laboratory testing suite for characterization of asphalt concrete mixtures obtained from field cores (with discussion). *Journal of the Association of Asphalt Paving Technologists*, *75*, 815-851.

Xie, Z.H., Guo, Y.C., Yuan, Q.Z. & Huang, P.Y. (2015). Mesoscopic numerical computation of compressive strength and damage mechanism of rubber concrete. *Advances in Materials Science and Engineering*, *2015*, 257984. https://doi.org/10.1155/2015/279584

Zhang, Z., Song, X., Liu, Y., Wu, D. & Song, C. (2017). Three-dimensional mesoscale modelling of concrete composites by using random walking algorithm. *Composites Science and Technology*, *149*, 235-245.

Zhou, R. & Lu, Y. (2018). A mesoscale interface approach to modelling fractures in concrete for material investigation. *Construction and Building Materials*, *165*, 608-620.

Summary

Mesoscale modeling of fracture in cement and asphalt concrete. In this paper, mesoscale modeling is performed to simulate and understand fracture behavior of two concrete composites: cement and asphalt concrete using disk-shaped compact tension (DCT) tests. Mesoscale models are used as alternative to macroscale models to obtain better realistic behavior of composite and heterogeneous materials such as cement and asphalt concrete. In mesoscale models, aggregate and matrix are represented as distinct materials and each material has its characteristic properties. Disk-shaped compact tension test is used to obtain tensile strength and fracture energy of materials. This test can be used as a better alternative to other tests such as three points bending tests because it is more convenient for both field and laboratory specimens in addition to its accurate results. Comparing the numerical results of the mesoscale models of cement and asphalt concrete specimens with experimental data shows that these models can predict the behavior of these composite materials very well as seen in the curves of load-crack mouth opening displacement (CMOD). Also, the mesoscale modeling highlights the variability of crack direction where it is dependent on the random distribution of aggregate.

Authors' address:
Haider M. Al-Jelawy – corresponding author
(https://orcid.org/0000-0003-2465-794X)
University of Al-Qadisiyah
College of Engineering
Roads and Transport Engineering Department
Al-Jamaah Str., Al Diwaniyah
Iraq
e-mail: haider.aljelawy@qu.edu.iq

Ayad Al-Rumaithi
University of Baghdad
College of Engineering
Department of Civil Engineering
Baghdad
Iraq

Aqeel T. Fadhil
University of Baghdad
College of Engineering
Department of Civil Engineering
Baghdad
Iraq

Alaa J. Naji
University of Al-Qadisiyah
College of Engineering
Roads and Transport Engineering Department
Diwaniyah
Iraq

Scientific Review – Engineering and Environmental Sciences (2021), 30 (3), 451–463
Sci. Rev. Eng. Env. Sci. (2021), 30 (3)
Przegląd Naukowy – Inżynieria i Kształtowanie Środowiska (2021), 30 (3), 451–463
Prz. Nauk. Inż. Kszt. Środ. (2021), 30 (3)
http://iks.pn.sggw.pl
DOI 10.22630/PNIKS.2021.30.3.38

Osamah H. CHAFAT, Sahar Basim Al-GHURAB, Basim H. Al-HUMEIDAWI
University of Al-Qadisiyah, College of Engineering

Investigation the effect of newly used polymer modified bitumen on the performance of hot mix asphalt containing reclaimed asphalt pavement

Key words: creep compliance, rutting, recycling old pavement, novolac, hexamine

Introduction

Reclaimed asphalt pavement (RAP) is widely employed as a replacement for natural aggregates in road pavements in recent decades. In new mixtures, it has advantages of minimizing amount of raw materials used, reducing costs and reducing environmental damage. Many studies have been conducted on hot mix asphalt (HMA) incorporating RAP, ranging from mix design to performance assessment. Also, they investigated the impact of a increasing of the % RAP in new asphalt mixtures and found that HMA containing percentage of RAP can perform as well as or better than mixes comprised entirely fresh material (Al-Bayati, Tighe & Achebe, 2018; Mirhosseini, Tahami, Hoff, Dessouky & Ho, 2019; Zhu, Ma & Dong, 2020). The impact of polymer on performance of RAP-containing mixtures has also been studied in the literature (Daryaee, Ameri & Mansourkhaki, 2020; Wang et al., 2020). Some researchers reported, it is possible to produce HMA with a high RAP content and acceptable mechanical properties, however, thermal cracking resistance, fatigue resistance need further investigation (Leiva-Villacorta, Taylor & Willis, 2017).

Zhou, Gu, Jiang, Ni and Jiang (2019) studied the effect of RAP on the fatigue resistance of PMB mixtures. Their results showed that the increasing of RAP materials leads to increasing in fatigue life of mixtures. Pradhan and Sahoo (2020) examined the volumetric and mechanical properties of eleven mixes, five of them contained 30–70% RAP with softer binder, five mixes containing RAP with a rejuvenator, and one control mix. They found that, all mixes met the specifica-

tions of Superpave method. Ishaq and Giustozzi (2020) evaluated effects of adding RAP and a rejuvenator on freeze/ /thaw and moisture damage of HMA, using 20% RAP. Their results showed that using rejuvenator can help in decreasing the deteriorating of RAP mixtures and decrease the impacts of freeze/thaw and moisture damage of HMA. Ma et al. (2020) observed an improving in moisture resistance and cracking of mixes containing RAP heated to higher temperature. Montanez, Caro, Carrizosa, Calvo and Sanchez (2020) demonstrated that the mechanical responses and performance of HMA containing RAP vary significantly with RAP sources.

Polymer modified bitumen (PMB) is widespread in last years. It improves general characteristic of HMA prepared with it as well as the long term performance (Plati, 2019). Due to the higher initial and maintenance cost of flexible pavement, PMB and RAP showed to become more cost-effective in terms of fatigue life than conventional mixes (Souliman, Mamlouk & Eifert, 2016).

Kodippily, Holleran and Henning (2016) investigated the impact of adding RAP and PMB on HMA performance by preparing six mixtures with PMB and RAP at 0%, 15%, and 30%. Their results revealed that the mixture, which contains high percentage of RAP and PMB, meets the requirements of mechanical properties and sustainability of roads. Liphardt, Król and Radziszewski (2016) studied the effect of RAP which already contain PMB on rutting resistance in stone mastic asphalt (SMA) mixtures. It has been observed that adding more RAP-modified binders to asphalt mixes improves rutting resistance. Porot, Broere, Wistuba and Grönniger (2017) focused on evaluation the performance of mixture containing high percentage of RAP up to 70% with a bio-based rejuvenator agents. They found that the stiffness modulus was higher than the control mix and the rejuvenator agents improve the performance of HMA at high temperatures. It has been found that asphalt mixtures containing a low to medium ratio of RAP, often less than 25%, can perform as well as or better than mixes prepared with new materials (McDaniel & Nantung, 2005).

The current study focuses on investigation the effect of inclusion RAP in HMA up to 70%. The replacement was conducted for all sizes of aggregate particle in HMA. The study involved using PMB prepared with novolac (phenol formaldehyde solid resin) and it cross-linking agent (hexamine). This polymer is very limit and not previously used with HMA containing RAP.

Materials

Reclaimed asphalt pavement (RAP)

Reclaimed asphalt pavement material was collected from an old highway pavement connected Al-Diwainyah and Najaf cities (Iraq). The binder content and gradation of RAP were calculated after extracting the bitumen from RAP according to the ASTM D2172 standard (ASTM International [ASTM], 2017). The percentage of asphalt binder in RAP was found to be 2.92%. The physical properties and gradation of RAP materials can be found in previous article by authors (Al-Ghurabi & Al-Humeidawi, 2021).

Bitumen and aggregates

AC 40-50 was used as conventional bitumen. It physical properties and consistency tests results were reported in previous article by authors (Al-Ghurabi & Al-Humeidawi, 2021). The aggregates were crushed limestone with nominal maximum size of 12.5 mm. Limestone dust was used as mineral filler. The gradation, physical and chemical properties of aggregate and mineral filler were reported in previous article by authors (Al-Ghurabi & Al-Humeidawi, 2021).

Polymer

Novolac with cross-linking agent (hexamine) was utilized in this research to modify pure bitumen. The percentage of addition of novolac was 3% of weight of bitumen, and hexamine was added as 10% of weight of novolac. These percentages were selected according to several trials of asphalt binder consistency tests. The procedure of preparing PMB was found elsewhere (Al-Humeidawi, Medhlom, kadhim Hameed & Kadhim, 2018).

Methodology of the work

Mix design

The mixtures were produced using Marshall mix design technique according to the AASHTO T245 standard (American Association of State Highway and Transportation Officials [AASHTO], 2015). Optimum binder content (OBC) was found to be (4.7%) by total weight of mix. The experiments were carried out in two stages: the first stage involved, in addition to control mix, designing and preparing seven mixes with different % RAP (10%, 20%, 30%, 40%, 50%, 60%, and 70%) and conventional bitumen. These mixes were tested to predict their volumetric, mechanical, and performance characteristics. The second stage involved repeat preparing these mixes using PMB and the same tests were conducted for HMA mixes prepared with PMB.

Laboratory test

Four tests were included in this experimental program. The first test was Marshall stability which was conducted according to the ASTM D6927 standard (ASTM, 2015), the second test was indirect tensile strength (ITS) test which was conducted according to the AASHTO T283 standard (AASHTO, 2007), the third test was creep compliance test which was conducted according to the AASHTO T322 standard (AASHTO, 2011) and used to evaluate the stiffness and fatigue cracking resistance of HMA. This test was conducted by applying constant load for 100 s at temperature of 0°C, where two LVDTs were used to measure horizontal strain and one for vertical strain. The last test was wheel track test which was conducted according to the BS EN 12697-22 standard (British Standard Institution [BSI], 2003) and used to evaluate the permanent deformation of mix (rutting). This test was conducted by applying 10,000 cycles of loading on each specimen at temperature of 60°C. The moisture susceptibility of mixes was evaluated by calculating the tensile strength ratio (TSR) according to the AASHTO T283 standard.

Results and discussion

Volumetric properties

The volumetric properties of mixes were calculated using experimental tests results. These properties include air void (AV), voids in mineral aggregate (VMA), and voids filled with asphalt (VFA). The table illustrates the values of volumetric properties of HMA containing RAP with conventional and PMB binder. All volumetric properties were within the requirement limits. The AV are slightly increased with using PMB that may be related to increasing the viscosity of bitumen. The values of other properties have been changed accordingly. According to results of volumetric properties, all percentages of replacement can be adopted.

Marshall stability test

Figure 1 shows the results of Marshall stability for HMA involved replacing the virgin aggregate with different content of RAP up to 70% with an increment of 10%. The replacement included the retained aggregate on all sieves of coarse and fine aggregate with the adopted ratio. The values of Marshall stability is increased with using RAP especially at 10% and 50% RAP. These percentages of increases were 11% and 13% for mix with 10% and 50% RAP respectively for specimens prepared with conventional binder. The Marshall stability decreases with increasing RAP content up to 30% RAP, after that, Marshall stability increases again up to 50% RAP then decreases again. This response can be explained by, as a percentage of RAP replacement increases the ratio of aged asphalt increased which causes a reduction in Marshall stability, after 40% RAP replacement, the contribution of coarse aggregate increases which comprises 52% of total aggregate compared with fine aggregate which comprises 41% of total aggregate and lead to increases in

TABLE. Volumetric properties of HMA containing RAP

% RAP	AV%		VMA%		VFA%	
	conventional binder	PMB binder	conventional binder	PMB binder	conventional binder	PMB binder
	acceptable limits					
	(3–5) (SCRB, 2003)		≥ 14 (SCRB, 2003)		(65–75) (Asphalt Institute [AI], 2014)	
0%	4		15.1		73.5	
10%	3.55	3.87	14	14.3	74.6	72.9
20%	3.99	4.4	14.37	14.7	72.23	70
30%	3.63	3.79	14	14.2	74	73.3
40%	3.67	4.1	14.1	14.5	73.9	71.7
50%	4.61	4.73	14.9	15	69.1	68.5
60%	4.77	4.8	15.1	15.1	68.41	68.2
70%	4.41	4.61	14.1	14.9	70	69

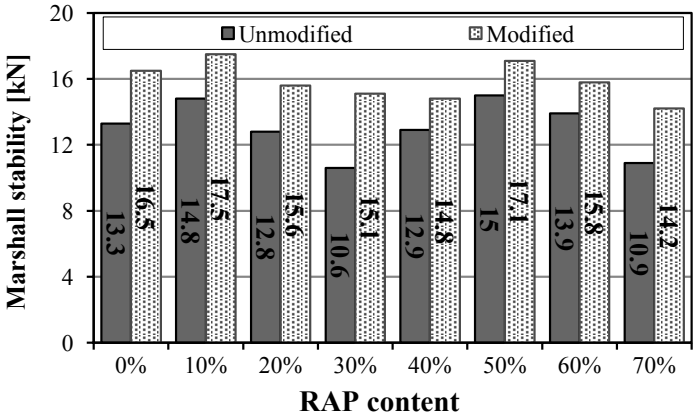

FIGURE 1. Marshall stability results for HMA contain different percentages of RAP

Marshall stability due to more mechanical interlock. With exceeding optimum value and replacing more than half the quantity of aggregate with RAP, the stability gradually decreases due to the contribution of more aged binder. For HMA prepared with PMB, it can be observed that all mixes have higher values of Marshall stability compared to mixes prepared with unmodified (conventional) binder. That is attributed to high viscosity of PMB binder resulting from modifying the binder with polymer. The trend of changing Marshall stability with RAP content is similar to that of unmodified bitumen for the same reason, however, the percentage of reduction is less than that of unmodified asphalt binder due to using PMB. For all mixes with conventional and PMB, Marshall flow values were in a range of 2–4 mm which is with the specifications of the State Roads and Bridges Corporation (SCRB, 2003).

Indirect tensile strength test (ITS)

Figure 2 shows the results of ITS for unconditioned and conditioned specimens of HMA mixes prepared with different percentages of RAP and unmodi-

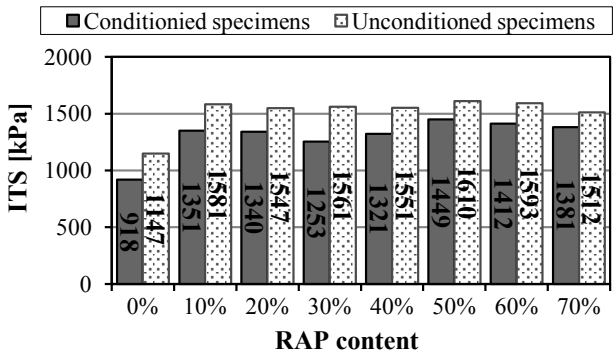

FIGURE 2. ITS test values for specimens with different percentages of RAP and conventional bitumen

fied bitumen. The use of RAP for all percentages of replacement significantly improves the ITS values for both unconditioned and conditioned specimens of HMA mixes. That is maybe attributed to existing of a hardening binder that has a higher viscosity which consequently increases the adhesion between the aggregate particles. The maximum value of ITS for both unconditioned and conditioned specimens of HMA mixes was achieved at 50% RAP replacement in a similar trend to that observed in Marshall stability test. Figure 3 presents the results of ITS for unconditioned and conditioned specimens of HMA mixes prepared with different percentages of RAP and PMB. The use of PMB improves ITS values especially for condition specimens due to more adhesion between aggregate particles. No significant variation in ITS values was observed between conditioned specimens with different percentages of RAP due to using PMB, which provides more adhesion between mix components. Figure 4 illustrates TSR for specimens prepared with conventional and PMB binder, and contain different percentages of RAP. All mixes showed TSR more than 80% which represents a minimum limit according to AASHTO T283. The use of PMB significantly improves TSR values of all mixes with an optimum value obtained at 50% RAP.

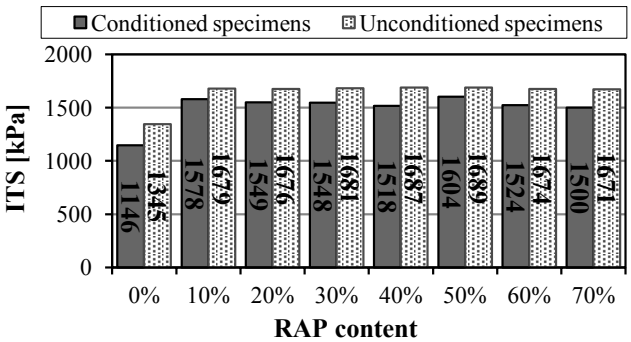

FIGURE 3. ITS test values for specimens with different percentages of RAP and PMB binder

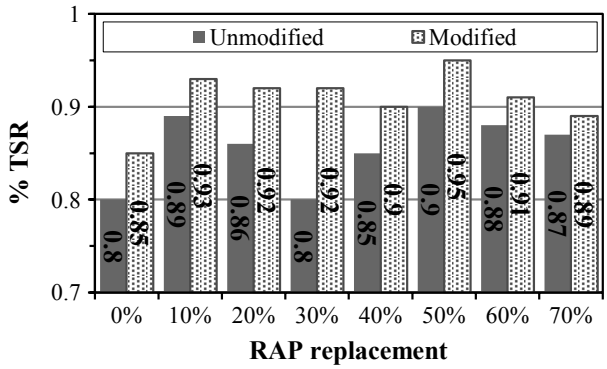

FIGURE 4. TSR values for modified and unmodified specimens with different percentages of RAP

Creep compliance

The creep compliance test was conducted at temperature of 0°C as shown in Figure 5. Figure 6 illustrates the results of creep compliance for control and HMA mixes prepared with different percentage of RAP and unmodified bitumen. Figure 7 illustrates the results of creep compliance for HMA mix prepared with different percentage of RAP and PMB, while Figure 8 shows the final results of creep compliance for samples with conventional and PMB. Form these figures it can be observed that the using of all investigated percentages of RAP reduce the values of creep compliance compared with control mix. That may be related to higher vis-

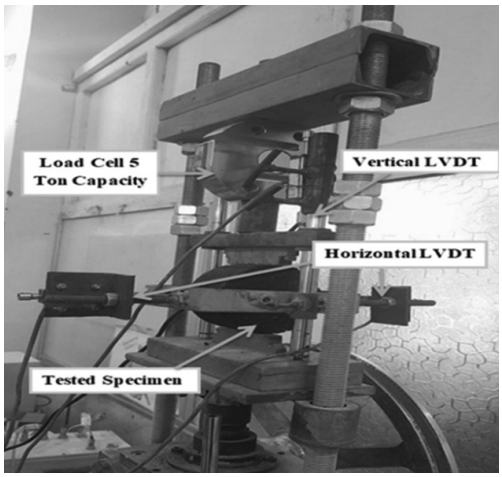

FIGURE 5. Test machine for creep compliance

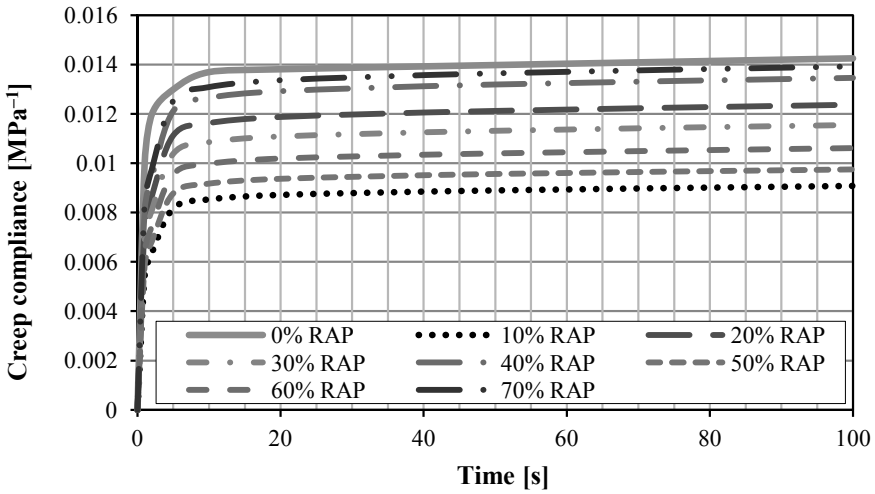

FIGURE 6. Creep compliance for HMA contained different percentages of RAP and conventional bitumen

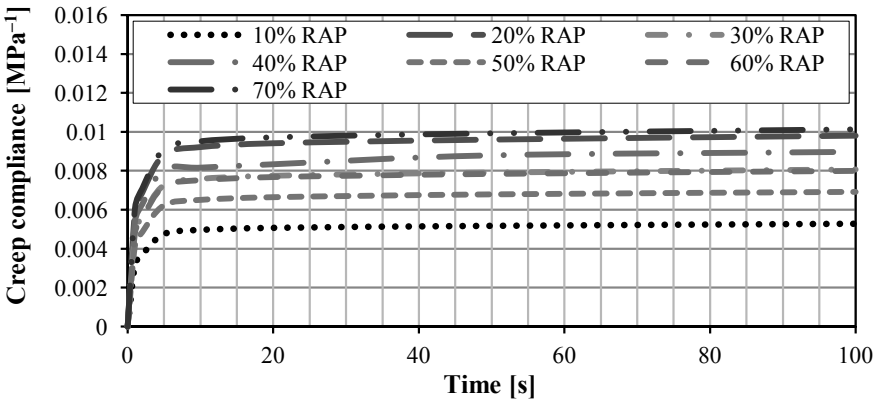

FIGURE 7. Creep compliance for HMA contained different percentages of RAP and PMB

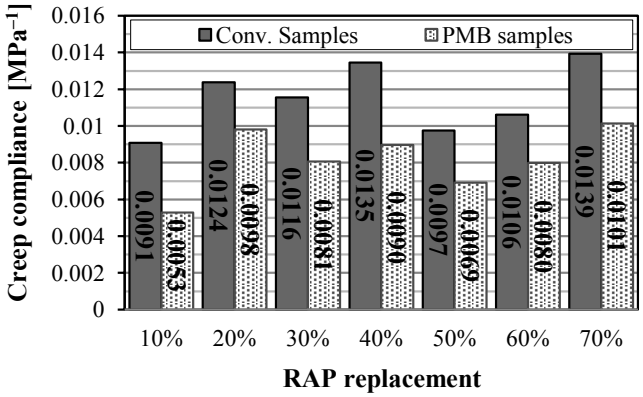

FIGURE 8. Creep compliance for HMA mixes with conventional and PMB

cosity of hardened binder and less porosity of RAP aggregate which reduces the asphalt binder absorption. Also, the using of PMB significantly reduces the creep compliance values for all percentages of RAP replacement which is an indication of increase the stiffness of HMA and increases the cracks resistance. That may be related to more adhesion between aggregate particles provided by PMB. The lower creep compliance values were obtained at percentages of RAP replacement of 10% and 50% in similar trend to what were observed in previous tests.

Wheel track test (WTT)

Wheel track test was conducted according to the BS EN 12697-22 standard, using wheel track testing machine shown in Figure 9. The specimens were nine, one specimen was for control mix, four specimens with conventional binder and four different percentages of RAP (10%, 30%, 50%, and 70%) and four specimens with PMB binder and four different percentages of RAP (10%, 30%, 50%, and 70%). Figures 10, 11 and 12 show the results of rut depth for all previously mentioned

FIGURE 9. Wheel track testing machine

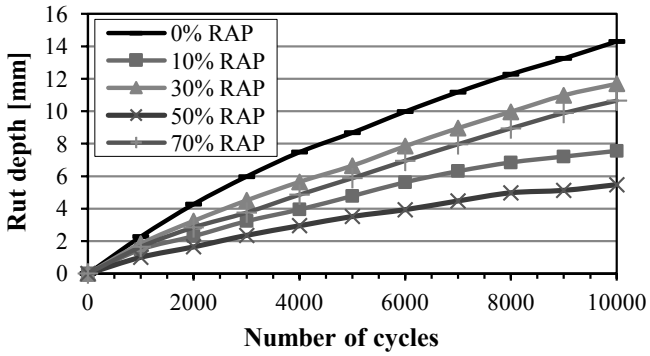

FIGURE 10. Effect of RAP content on rut depth for specimens prepared with conventional binder

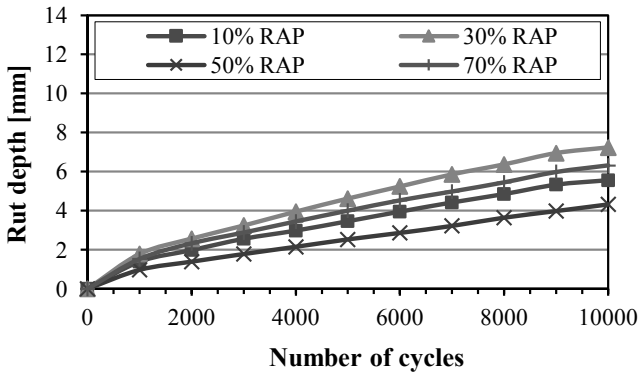

FIGURE 11. Effect of RAP content on rut depth for specimens prepared with PMB binder

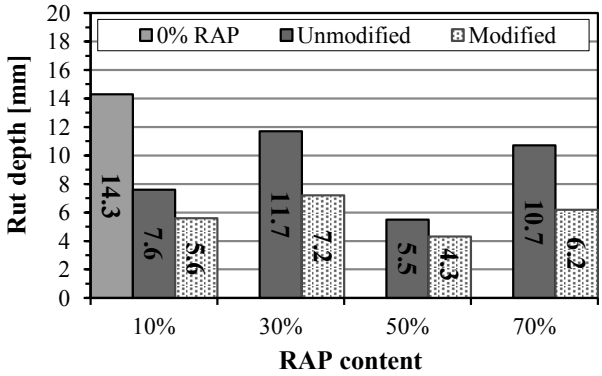

FIGURE 12. Final rut depth values for all HMA mixes with different percentage of RAP, and with conventional and PMB binder

specimens. The results showed that the using of RAP reduces the rut depth compared with control mix. Significant reduction was observed with PMB instead of conventional binder. The lowest rutting depth was obtained at 50% RAP replacement for both conventional and PMB binder. The percentages of reduction were reached up 38% and 30% for specimens contains 50% RAP, and prepared with conventional and PMB binder respectively compared with control mix. The increase in binder stiffness constrains the ability of the aggregate particles to slide or move even on a micro-scale due to the high viscosity of hardened and PMB binder which improves the rutting resistance of HMA. Figure 13 shows pictures for tested specimens.

Conclusions

Based on the results of this study, the following conclusions can be drawn:

1. The using of PMB binder prepared by adding novolac and hexamine to conventional bitumen, can significantly improve the performance of HMA contained RAP. This type of PMB is used for first time with HMA contained RAP.

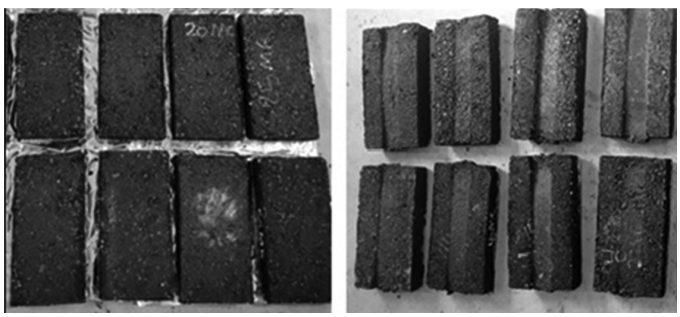

FIGURE 13. Sample preparation and testing for wheel track test

2. In general, the incorporation of RAP material in various percentages, as well as PMB in this study, improves mechanical properties and performance of HMA (Marshall stability, ITS, moisture damage resistance, resistance for permenant deformation, i.e. ruting, and fatigue life).
3. According to results of this study, it was found that the 50% RAP replacement is the optimum percentage of RAP replacment in HMA. Using of 50% RAP resulted in maximum increasing in ITS values for both unconditioned and conditioned samples. This improvement leads to high resistance to moisture damage of HMA measured in term of TSR and consequently less stripping for mix components.
4. From the creep compliance test, the incorporation of RAP materials and PMB reduce the creep compliance values for all percentages of RAP replacement which is an indication of increasing stiffness of HMA and improves the fatigue life.
5. The inclusion of RAP materials and PMB improved rutting resistance of HMA. The rut depth values of HMA contained RAP and PMB significantly reduced compared with the control mix. The lowest rutting depth was obtained at 50% RAP replacement for both conventional and PMB binder as the rut depth reduced to 38% and 30% of the control mix value for unmodified and PMB mixes respectively.
6. Results of experimental work indicated that all HMA which prepared with RAP and PMB resulted in better performance compared to HMA contianed entirely fresh aggregate and conventional binder due to high viscosity of RAP and PMB which leads to an increase in the stiffness of HMA.

References

Al-Bayati, H.K.A., Tighe, S.L. & Achebe, J. (2018). Influence of recycled concrete aggregate on volumetric properties of hot mix asphalt. *Resources. Conservation and Recycling*, *130*, 200-214.

Al-Ghurabi, S.B. & Al-Humeidawi, B.H. (2021). Comparative evaluation for the effect of particles size of reclaimed asphalt pavement (RAP) on the properties of HMA. *Journal of Physics: Conference Series*, *1895*(1), 012025. https://doi.org/10.1088/1742-6596/1895/1/012025

Al-Humeidawi, B.H., Medhlom, M.K., kadhim Hameed, K. & Kadhim, H.K. (2018). Production of hard grade bitumen for using in high modulus asphalt concrete. *Journal of University of Babylon for Engineering Sciences*, *26*(6), 157-174.

American Association of State Highway and Transportation Officials [AASHTO] (2007). *Standard method of test for resistance of compacted asphalt mixtures to moisture-induced damage* (AASHTO T283). Washington: American Association of State Highway and Transportation Officials.

American Association of State Highway and Transportation Officials [AASHTO] (2011). *Determining the creep compliance and strength of hot mix asphalt (HMA) using the indirect tensile test device* (AASHTO T322). Washington: American Association of State Highway and Transportation Officials.

American Association of State Highway and Transportation Officials [AASHTO] (2015). *Standard method of test for resistance to plastic flow of asphalt mixtures using Marshall apparatus* (AASHTO T245). Washington: American Association of State Highway and Transportation Officials.

Asphalt Institute [AI] (2014). *MS-2 asphalt mix design methods*. Lexington (KY): Asphalt Institute.

ASTM International [ASTM] (2015). *Standard test method for Marshall stability and flow of asphalt mixtures* (ASTM D6927-15). West Conshohocken (PA): ASTM International.

ASTM International [ASTM] (2017). *Standard test methods for quantitative extraction of asphalt binder from asphalt mixtures* (ASTM D2172). West Conshohocken (PA): ASTM International.

British Standard Institution [BSI] (2003). *Bituminous mixtures. Test methods for hot mix asphalt* (BS EN 12697-22). London: British Standard Institution.

Daryaee, D., Ameri, M. & Mansourkhaki, A. (2020). Utilizing of waste polymer modified bitumen in combination with rejuvenator in high reclaimed asphalt pavement mixtures. *Construction and Building Materials*, *235*, 117516. https://doi.org/10.1016/j.conbuildmat.2019.117516

Ishaq, M.A. & Giustozzi, F. (2020). Rejuvenator effectiveness in reducing moisture and freeze/ /thaw damage on long-term performance of 20% RAP asphalt mixes: An Australian case study. *Case Studies in Construction Materials*, *13*, e00454. https://doi.org/10.1016/j.cscm.2020.e00454

Kodippily, S., Holleran, G. & Henning, T.F.P. (2016). Deformation and cracking performance of recycled asphalt paving mixes containing polymer-modified binder. *Road Materials and Pavement Design*, *18*(2), 425-439.

Leiva-Villacorta, F., Taylor, A. & Willis, R. (2017). *High-modulus asphalt concrete (HMAC) mixtures for use as base course*. Auburn (AL): National Center for Asphalt Technology Report at Auburn University.

Liphardt, A., Król, J. & Radziszewski, P. (2016). Influence of polymer modified binder content from RAP on stone mastic asphalt rutting resistance. *Procedia Engineering*, *153*, 407-413.

Ma, Y., Polaczyk, P., Park, H., Jiang, X., Hu, W. & Huang, B. (2020). Performance evaluation of temperature effect on hot in-place recycling asphalt mixtures. *Journal of Cleaner Production*, *277*, 124093. https://doi.org/10.1016/j.jclepro.2020.124093

McDaniel, R. & Nantung, T. (2005). Designing superpave mixes with locally reclaimed asphalt pavement. *TR NEWS*, *239*, 28-30.

Mirhosseini, A.F., Tahami, S.A., Hoff, I., Dessouky, S. & Ho, C.H. (2019). Performance evaluation of asphalt mixtures containing high-RAP binder content and bio-oil rejuvenator. *Construction and Building Materials*, *227*, 116465. https://doi.org/10.1016/j.conbuildmat.2019.07.191

Montanez, J., Caro, S., Carrizosa, D., Calvo, A. & Sanchez, X. (2020). Variability of the mechanical properties of Reclaimed Asphalt Pavement (RAP) obtained from different sources. *Construction and Building Materials*, *230*, 116968. https://doi.org/10.1016/j.conbuildmat.2019.116968

Plati, C. (2019). Sustainability factors in pavement materials, design, and preservation strategies: a literature review. *Construction and Building Materials*, *211*, 539-555.

Porot, L., Broere, D., Wistuba, M. & Grönniger, J. (2017). Asphalt and binder evaluation of asphalt mix with 70% reclaimed asphalt. *Road Materials and Pavement Design*, *18*(sup2), 66-75.

Pradhan, S.K. & Sahoo, U.C. (2020). Influence of softer binder and rejuvenator on bituminous mixtures containing reclaimed asphalt pavement (RAP) material. *Journal of Transportation Science Technology* (in press).

Souliman, M.I., Mamlouk, M. & Eifert, A.J.P.E. (2016). Cost-effectiveness of rubber and polymer modified asphalt mixtures as related to sustainable fatigue performance. *Procedia Engineering*, *145*, 404-411.

State Corporation of Roads and Bridges [SCRB] (2003). *General specifications for roads and bridges*. Baghdad: State Corporation of Roads and Bridges, Ministry of Housing and Construction, Republic of Iraq.

Wang, J., Qin, Y., Xu, J., Zeng, W., Zhang, Y., Wang, W., & Wang, P. (2020). Crack resistance investigation of mixtures with reclaimed SBS modified asphalt pavement using the SCB and DSCT tests. *Construction and Building Materials*, *265*, 1-8.

Zhou, Z., Gu, X., Jiang, J., Ni, F., & Jiang, Y. (2019). Fatigue cracking performance evaluation of laboratory-produced polymer modi-

fied asphalt mixture containing reclaimed asphalt pavement material. *Construction and Building Materials*, *216*, 379-389.

Zhu, J., Ma, T. & Dong, Z. (2020). Evaluation of optimum mixing conditions for rubberized asphalt mixture containing reclaimed asphalt pavement. *Construction and Building Materials*, *234*, 117426. https://doi.org/10.1016/j.conbuildmat.2019.117426

Summary

Investigation the effect of newly used polymer modified bitumen on the performance of hot mix asphalt containing reclaimed asphalt pavement. The current research focuses on investigating the effect of using reclaimed asphalt pavement (RAP) on performance of hot mix asphalt (HMA) prepared with polymer modified bitumen (PMB) binder. This PMB used for the first time with HMA contained RAP. The mechanical properties and performance of HMA were assessed using several standard tests including Marshall, indirect tensile strength, creep compliance, and wheel track test. The RAP replacement was conducted up to 70% of total aggregate in HMA with an increment of 10%. The results of investigation showed, that the use of PMB binder prepared by addition novolac (phenol formaldehyde solid resin) and hexamine to conventional bitumen, significantly improved the performance of HMA contained RAP. Also, the optimum percentage of RAP replacement was found to be 50% of total aggregate in HMA. For this level of replacement, the rut depth reduced up to 38% of its original value.

Authors' address:
Basim H. Al-Humeidawi – corresponding author
(https://orcid.org/0000-0002-1566-5983)
University of Al-Qadisiyah
College of Engineering
Roads and Transport Engineering Department
Al-Jamaah Str., Al Diwaniyah
Iraq
e-mail: basim.alhumeidawi@qu.edu.iq

Scientific Review – Engineering and Environmental Sciences (2021), 30 (3), 464–476
Sci. Rev. Eng. Env. Sci. (2021), 30 (3)
Przegląd Naukowy – Inżynieria i Kształtowanie Środowiska (2021), 30 (3), 464–476
Prz. Nauk. Inż. Kszt. Środ. (2021), 30 (3)
http://iks.pn.sggw.pl
DOI 10.22630/PNIKS.2021.30.3.39

Haider M. OWAID, Muna M. Al-RUBAYE, Haider M. Al-BAGHDADI

University of Babylon, College of Engineering

Use of waste paper ash or wood ash as substitution to fly ash in production of geopolymer concrete

Key words: geopolymer concrete (GC), fly ash (FA), waste paper ash (WPA), wood ash (WA), alkaline solution

Introduction

Concrete is the most popular and widely used building material owing to availability of its raw materials and it combines good mechanical properties, durability, workability and it is relatively inexpensive. Ordinary Portland cement (OPC) is the key constituent binding material used in the concrete production, however manufacturing of OPC contributes substantially to global CO_2 emissions and energy consumption (Fairbairn et al., 2010). The main causes of high CO_2 emissions, which is known as the greenhouse gas rising from manufacturing of OPC have been attributed to the process of calcination of limestone and high energy consumption (Davidovits, 2011; Turner & Collins, 2013). Concrete is mainly used in the construction of buildings in civil engineering applications and infrastructure projects. Hence, the construction of buildings is under increasing pressure of developing green binder materials that possess the desired engineering properties to overcome the CO_2 emission and reduce the dependence on the OPC (Małaszkiewicz & Jastrzębski, 2018; Abdulkareem, Ramli & Matthews, 2019). Several alternative cementitious materials that are principally derived from industrial by-products can provide comparable performance to the OPC in a range of applications, but with an additional advantage of significantly reduced greenhouse emissions (Gartner, 2004). The alternative materials involve sugar cane bagasse ash (SCBA), fly ash (FA), metakaolin (MK), rice hush ash (RHA), blast furnace slag (BFS), vulcanic ash and bottom ash (BA) (Fernandez-Jimenez, Palomo & Lopez-Hombrados, 2006; Fairbairn et al., 2010; Risdanareni, Karjanto & Khakim, 2016;

Thaarrin & Ramasamy, 2016; Ekaputri & Junaedi, 2017; Mehta and Siddique, 2018), which contain much silica (SiO_2) and alumina (Al_2O_3). The most popular of these materials that considered in manufacturing GC is fly ash (FA), which is residue from the burnt coal, and it is available worldwide as a waste material (Ryu, Lee, Koh & Chung, 2013). An alternative concrete termed "geopolymer concrete" (GC) that based on one of the by-product materials as a substitute for OPC has been considered as environmentally friendly concrete (Hardjito, Wallah, Sumajouw & Rangan, 2004).

This concrete is formed by the alkaline activation of the aforementioned by-products materials to form an aluminosilicate gel structure through the polycondensation reaction. The alkaline activator used is commonly a combination of a hydroxyl, usually sodium hydroxide (NaOH) or potassium hydroxide (KOH) and sodium silicate (Na_2SiO_3) or potassium silicate (Turner & Collins, 2013). Besides, it is required to provide curing for GC with elevated temperature between 40°C and 80°C for at least 6 h to achieve an equivalent strength to OPC concrete (Duxson et al. 2007; Ryu et al. 2013). Beside the interest in finding low CO_2 emission and low energy consumption binders there is an interest in investigating the possibility of using the waste materials as the substitutes for OPC in producing of geopolymer concretes (Shi, Wu, Riefler & Wang, 2005). The construction industry offers reusability solutions for wastes due to the large consumption of materials and the large number of construction sites, thereby, in many developed economies, waste represents a resource that can be utilized for a diversity of beneficial purposes (Tam, Soomro & Evangelista, 2018). Huge amounts of paper and wood waste are generated every day due to the increase of production and population, the disposal of these waste to landfill is expensive in addition to the scarcity of suitable land that cause a number of pollution and environmental problems. Consequently, an economical alternative to landfill disposal is by reusing of waste materials, the waste reusability has many advantages, including the decrease in the waste volumes, the reduction of greenhouse gas emissions and the consumption of natural resources (Letelier, Henriquez-Jara, Manosalva & Moriconi, 2019).

Previous research has been published concerning the influence of using paper sludge ash on the properties of concrete and paste (Ishimoto, Origuchi & Yasuda, 2000; Bai et al., 2003; Frías, Garcia, Vigil & Ferreiro, 2008; García, de la Villa, Vegas, Frias & de Rojas, 2008; Mozaffari, Kinuthia, Bai & Wild, 2009). According to Pachamuthu and Thangaraju (2017), the improvement of the mechanical properties of GC that contains paper sludge ash depends on the percentages of paper sludge ash and the curing conditions. On the other hand, several studies (Etiegni & Campbell, 1991; Naik, Kraus & Siddique, 2003; Udoeyo, Inyang, Young & Oparadie, 2006; Chowdhury, Maniar & Suganya, 2015) were conducted to investigate the feasibility of the use of wood ash as a partial replacement material to OPC in making of blended mortar or concrete. This paper presents the feasibility of incorporating of waste paper ash (WPA) or wood ash (WA) as replacement materials for fly ash (FA)

(class F) in preparation geopolymer concrete (GC). The influence of the WPA or WA incorporation on the geopolymers' workability, compressive strength, splitting tensile strength and flexural strength has been studied and compared with neat FA geopolymer as a control mix.

Materials

Fly ash (FA), waste paper ash (WPA) and wood ash (WA)

In this study, fly ash FA (class F) that collected from Turkish hard coal from power station Iskenderun was used to produce GC mixes, the specific gravity of FA was 2.21 $g \cdot cm^{-3}$. It conforms to the ASTM standard specification C618--08a (ASTM International [ASTM], 2008). The waste paper ash (WPA) is a leftover material that has found in large quantities worldwide within offices, government departments and houses. The waste paper ash used for this study was collected from burning in oven up to 650 ±20°C, for 60 min, it has a specific gravity of 2.53 $g \cdot cm^{-3}$. Besides, wood ash (WA) obtained from industrial by-product such wood burning, it has a specific gravity of 2.31 $g \cdot cm^{-3}$. The chemical composition of FA, WPA and WA are listed in Table 1.

Fine and coarse aggregate

The fine aggregate used was natural river sand, free from loam and clay. The fine aggregate having specific gravity of 2.66 $g \cdot cm^{-3}$, with sulfate content of 0.23% and the grading of fine aggregate satisfies the requirements of Iraqi standard IQS 45/1984 (Iraqi Central Agency for Standardization and Quality Control [ICASQC], 1984) (Zone 2). While, the crushed gravel was used in this study with maximum size of 19 mm. The coarse aggregate having a specific gravity of 2.64 $g \cdot cm^{-3}$ and the sulfate ratio of 0.04% and it conforms to the IQS 45/1984 standard.

High-water range reducer

A high-water range reducer (SP400) has been utilized to enhance the workability of GC. It complies with the ASTM C494-C494M standard (ASTM, 2017).

Alkaline activator liquid

The alkaline liquid was obtained by blending solutions of sodium hydroxide and sodium silicate to activate the fly ash. Sodium hydroxide has flakey form and high purity more than 98%, which could be dissolved in the filtered water (molarity of solution of sodium hydro-

TABLE 1. Chemical composition of fly ash (FA), waste paper ash (WPA) and wood ash (WA)

Oxides [%]	SiO_2	AL_2O_3	Fe_2O_3	CaO	MgO	Na_2O	K_2O	SO_3	L.OI
FA	65.65	17.69	5.98	0.98	0.72	1.35	2.99	0.19	3.1
WPA	47.80	27.00	2.34	6.53	3.32	3.50	6.38	1.10	1.13
WA	32.51	28.30	2.14	9.53	3.32	10.50	12.3	0.10	22.50

xide (10M). The sodium silicate Na_2SiO_3 as a solution is commercially available.

Experimental program

The experimental program consists of preparing and testing different GC mixes to examine the influence of incorporating WPA or WA on the properties of GC. The developed GC mixes for this study were prepared at replacement ratios of FA by WPA or WA of 25, 50, 75 and 100% in addition to a control mix containing 100% of FA. The tested mixes have been evaluated with respect to the workability, the compressive strength at ages of the tested specimens of 7, 28 and 56 days. Tensile splitting strength and flexural strength at age of the 28 days.

Mix proportions of GC mixes

Based on the geopolymer concrete mix designed by Rangan (2008), the GC mix was developed taken into account the workability and the ratio of silicate-sodium to sodium hydroxide solution was 2.5. The density of GC was 2,400 $kg \cdot cm^{-3}$. The mix proportions of all GC mixes are illustrated in Table 2.

Preparation of test specimens

The binder (FA, WPA or WA) was dry mixed with the fine and coarse aggregates using pan mixer for 4 min. Then, the superplasticizer dosages (SP) and the prepared alkaline activator liquid used of the GC mixes were mixed for 2 min and added gradually to the solid ingredients. Afterwards, the wet mixing continued for 5 min more until the mix was homogenized. For the workability evaluation, the fresh GC mixes were tested using slump test. The slump test was performed in accordance with the ASTM C143/C143M-05a standard (ASTM, 2005).

TABLE 2. Mix proportions of test GC mixes [$kg \cdot m^{-3}$]

Mix symbol	FA	Repl. [%]	WPA	WA	Fa*	Ca**	Alkaline liquid	Alkaloid to binder ratio	SP
GF-0	404	0	0	0	660	1 100	176	0.43	9
GF-P25	303	25	101	–	660	1 100	176	0.43	9
GF-P50	202	50	202	–	660	1 100	176	0.43	9
GF-P75	101	75	303	–	660	1 100	176	0.43	9
GF-P100	0	100	404	–	660	1 100	176	0.43	9
GF-W25	303	25	–	101	660	1 100	176	0.43	9
GF-W50	202	50	–	202	660	1 100	176	0.43	9
GF-W75	101	75	–	303	660	1 100	176	0.43	9
GF-W100	0	100	–	404	660	1 100	176	0.43	9

*fine aggregate, **coarse aggregate.

For evaluating the compressive, splitting tensile and flexural strengths, the fresh GC mixes were cast into cubic moulds of 100 mm, cylindrical moulds of 100 × 200 mm and prism moulds of 100 × 100 × 400 mm. After casting, the specimens were vibrated for 2 min on the vibration table to remove entrapped air. Thereafter, the moulded specimens were covered using a plastic sheet to prevent water evaporation. According to Rangan (2008), the effective curing temperature is 60°C, thus the specimens were then cured in an oven at a temperature of 60°C for one day.

Finally, the specimens have been left at room temperature until the testing date. The compressive strength test was conducted in accordance the BS 1881--116:1983 standard (British Standards Institute [BSI], 1983), while the splitting tensile strength was conducted according to the ASTM C496 standard (ASTM, 2004), and the flexural strength test was conducted according to the ASTM C78 standard (ASTM, 2002).

Results and discussion

Workability of GC mixes

The workability of all fresh GC mixes was measured immediately after mixing using slump test as for the conventional concrete. The SP was used to achieve the required slump with a dosage of 2.25% by weight of binder for all types of GC mixes and the liquid/binder ratio was kept of 0.43 for all the GC mixes. The slump values for all GC mixes were ranged from 98–104 mm as summarized in Table 3, the results showed there were no significant differences in the slump values for all GC mixes.

TABLE 3. The slump of GC mixes

Mix symbol	Slump [mm]
GF-0	104
GF-P25	98
GF-P50	101
GF-P75	100
GF-P100	102
GF-W25	99
GF-W50	103
GF-W75	101
GF-W100	99

Mechanical properties of GC mixes

The results of the compressive, splitting tensile and flexural strengths of GC specimens are in Table 4. The results of compressive strength of GC specimens were at ages of 7, 28 and 56 days and Figures 1 and 2 display the variations of compressive strength as the proportional percentages of compressive strength GC mixes to the control GC mixes (GF-0). As observed from Table 4 that the control mix GF-0 (100% FA) developed the highest compressive strength than the other blended mixes containing WPA or WA at the all ages, and the compressive strength of the control specimens increased after extended aging to 56 days. Results also show a small decrease in the compressive strength for GC mixes that incorporation WPA of 25% (GF-P25) at the all-tested ages and 50% (GF-P50) at 7 and 28 days in comparison with the GF-0. Whereas the GF-P50 at 56 days has more decrease in compressive strength as compared to the GF-0.

TABLE 4. Test results of the mechanical properties of GC mixes properties

Mix symbol	Compressive strength [MPa]			Splitting tensile strength [MPa]	Flexural strength [MPa]
	7 days	28 days	56 days	28 days	28 days
GF-0	42.38	57.73	61.51	3.52	4.85
GF-P25	42.00	56.78	59.86	3.41	4.77
GF-P50	41.82	55.53	56.88	3.21	5.02
GF-P75	39.18	52.43	52.26	3.10	4.35
GF-P100	35.12	49.28	50.37	2.93	4.10
GF-W25	41.10	55.24	57.82	2.92	4.55
GF-W50	34.11	49.27	53.58	2.54	4.35
GF-W75	29.22	43.13	47.75	2.30	3.83
GF-W100	20.00	39.5	44.21	2.10	3.17

On the other hand, excluding the GC mix incorporation WA of 25% (GF-W25) at ages of 7 and 28 days, the GC mixes inclusion WA of 50, 75 and 100% (GF-W50, GF-W75 and GF-W100) have the lowest compressive strength at all tested ages in comparison to GF-0 mix. Besides, it can be seen from Figures 1 and 2 that the most notable decreases in compressive strength appear in the mixes 100 % WPA (GF-P100) or 100% WA (GF-W100) compared to those of the control mixes (GF-0) at all tested ages. The compressive strength of the control mixes decreases by about 14, 17.6 and 18% and 52.8, 31.6 and 28% in the GC mixes incorporation 100% WPA or 100% WA at 7, 28 and 56 days

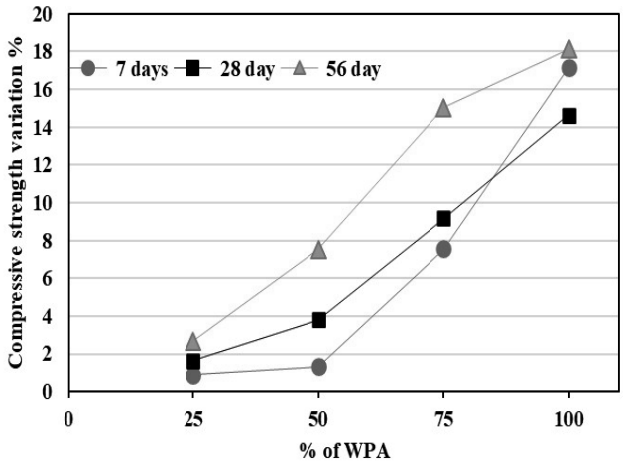

FIGURE 1. Compressive strength variation of GC mixes with replacement of FA by WPA

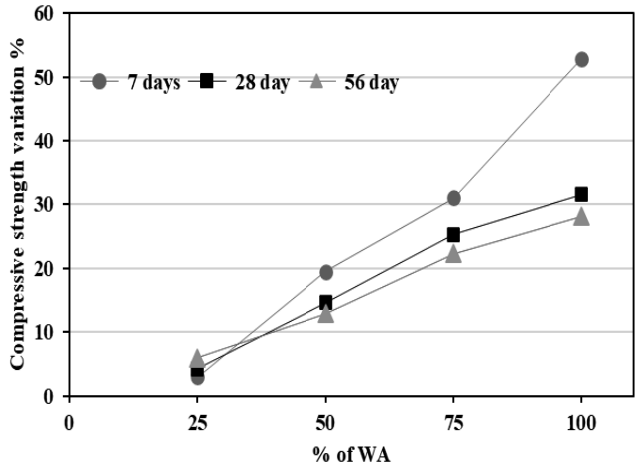

FIGURE 2. Compressive strength variation of GC mixes with replacement of FA by WA

respectively. Moreover, the reduction in compressive strength for GC mixes inclusion WA is more obvious than in mixes inclusion WPA. This may be due to the concentration of silicate through WPA more than WA, which affects the strength development due to higher silicates availability for the polymerization (Fernández-Jiménez, García-Lodeiro & Palomo, 2007). Also, the high CaO content present in WA causes reduction in strength of GC mixes (Astutiningsih and Liu, 2005; Luga & Peqini, 2019). Generally, the reduction of compressive strength for GC mixes as the replacement percentages of WPA or WA are increased, is justified due to the slower dissolution rate of WPA and WA in comparison with that high dissolution rates of the FA aluminosilicate, which has an impact on the strength development; as a result of reducing the silicon and aluminium ions (Shi et al., 2005).

The results of the splitting tensile strength of the GC specimens at age of 28 days are given in Table 4. Figure 3 displays the variations of splitting tensile strength as proportional percentages to the control mixes GF-0. As can be observed from these results that the splitting tensile strength of the control mix GF-0 (100% FA) developed the highest splitting tensile strength than the other blended mixes containing WPA or WA. The splitting tensile strength of the GC mixes inclusion WPA or WA reduced with increasing WPA and WA contents and the reductions were more pronounced when compared with reductions in compressive strength.

The splitting tensile strength of the control mix decreases by about 16.8 and 40.3% in the GC mixes incorporation 100% WPA or 100% WA respectively. Besides, the GC mixes inclusion WA showed lower values of the splitting tensile strength as compared to those obtained for GC mixes inclusion WPA.

The flexural strength results of the studied GC specimens at 28 days are presented in Table 4 and Figures 4 and 5. It is evident from the test results that the use of WPA or WA resulted in decrease in the flexural strength with

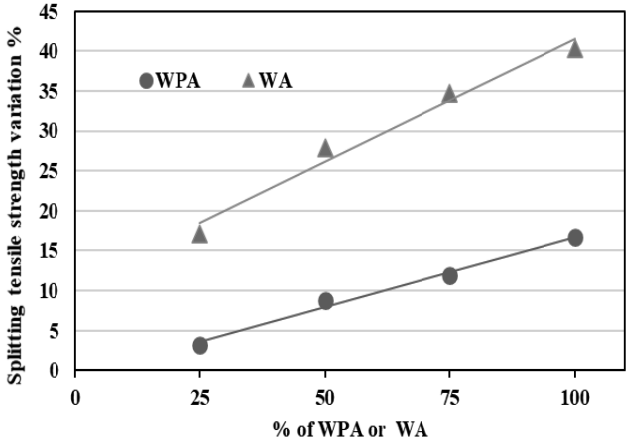

FIGURE 3. Splitting tensile strength variation of GC mixes with replacement of FA by WPA or WA

increasing WPA or WA contents excluding the GC mix with 50% WPA, which exhibited flexural strength greater than that of the control mix (GF-0). Further, the reductions in flexural strengths for GC mixes inclusions WPA or WA are close to those reductions in compressive strength for these mixes and less than the reductions in splitting tensile strength.

Figures 6 and 7 show the studied strength parameters (compressive strength, splitting tensile strength and flexural strength) at age of 28 days for GC mixes with replacement of FA by WPA or WA respectively. The decrease in the strength parameters occurred as the WPA or WA contents increase, which, can attributed to the silicate and aluminate contents and low value of pozzolanic reactivity of WPA and WA. Moreover, the reduction is more pronounce in GC mixes inclusion WA due to high content of CaO present in WA.

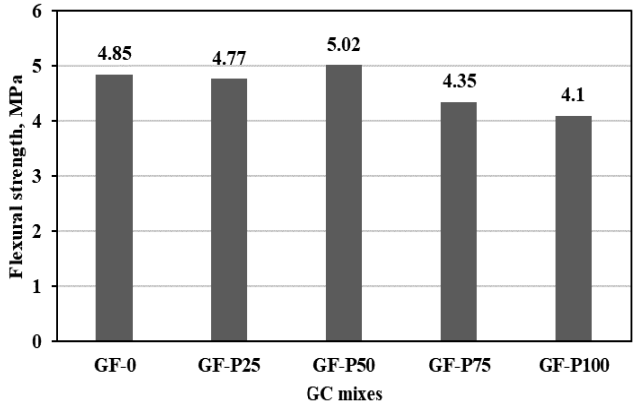

FIGURE 4. The flexural strength of the GC mixes with replacement of FA by WPA

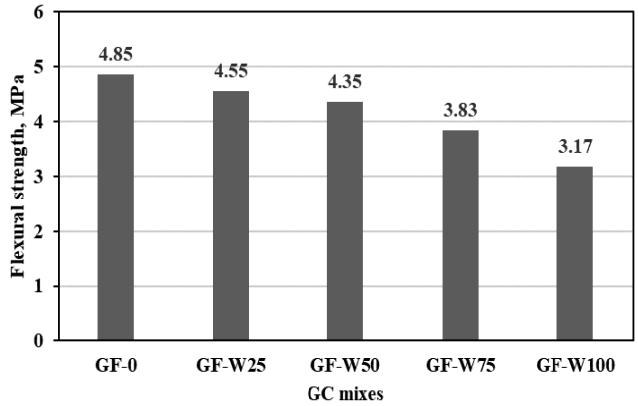

FIGURE 5. The flexural strength of the GC mixes with replacement of FA by WA

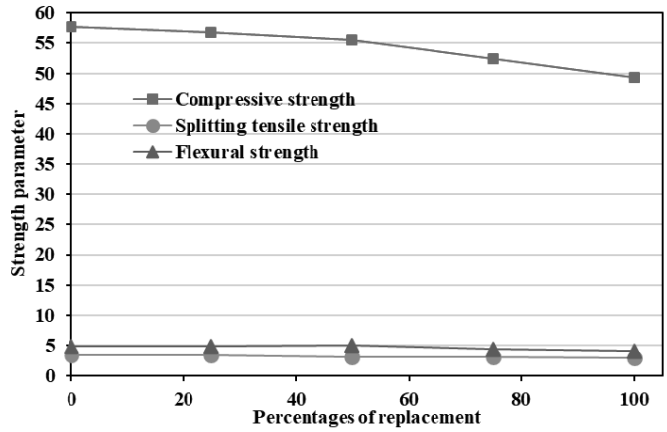

FIGURE 6. Strength parameters at 28 days for GC mixes with replacement of FA by WPA

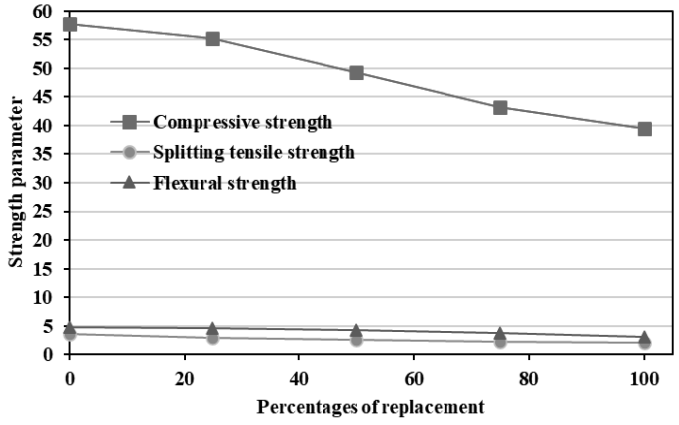

FIGURE 7. Strength parameters at 28 days for GC mixes with replacement of FA by WA

Conclusions

The properties of GC made with WPA from offices, and houses and WA from industrial waste replacing FA class F in absolute volume percentages up to 100% was evaluated in this study. The main conclusions are as follows:

– The results of the workability showed that there were no significant differences in the slump values of developed GC mixes with WPA or WA and the control GC mix (GF-0).
– The results of the development compressive strength of GC mixes inclusion 25–50% of WPA are close when compared with compressive strength of control mix of (GF-0). Replacement of 75–100% of WPA caused a further decrease in compressive strength of the GC mixes.
– The replacement with 25% WA had little effect on the compressive strength of GC mixes, while replacement with 50, 75 and 100% WA resulted in more reduction in the compressive strength of GC mixes in comparison with the control mix (GF-0).
– The splitting tensile strength of the GC mixes inclusion WPA is influenced with increasing WPA content, and the inclusion of WA as replacement for FA negatively affected the splitting tensile strength. The reductions in splitting tensile strength are more pronounced than the reductions in compressive and in flexural strengths.
– The reductions in flexural strength for GC mixes inclusion WPA or WA are close to those reductions in compressive strength for these mixes and less than the reductions in splitting tensile strength.
- From the present obtained results, it can be concluded that the GC mix with partial replacement of FA by WPA up to 50% or WA up to 25% can be satisfactorily used in preparation of the GC. Besides, utilizing these materials in developing GC has economic and environmental benefits.

References

Abdulkareem, O.A., Ramli, M. & Matthews, J.C. (2019). Production of geopolymer mortar system containing high calcium biomass wood ash as a partial substitution to fly ash: an early age evaluation. *Composites Part B: Engineering*, *174*, 106941. https://doi.org/10.1016/j.compositesb.2019.106941

ASTM International [ASTM] (2002). *Standard test method for flexural strength of concrete* (ASTM C78-02). West Conshohocken (PA): ASTM International.

ASTM International [ASTM] (2004). *Standard test method for splitting tensile strength of cylindrical concrete specimens* (ASTM C496-04). West Conshohocken (PA): ASTM International.

ASTM International [ASTM] (2005). *Standard test method for slump of hydraulic-cement concrete* (ASTM C143/C 143M-05a). West Conshohocken (PA): ASTM International.

ASTM International [ASTM] (2008). *Standard specification for coal fly ash and raw or calcined natural pozzolan for use in concrete* (ASTM C618-08a). West Conshohocken (PA): ASTM International.

ASTM International [ASTM] (2017). *Standard specification for chemical admixtures for concrete* (ASTM C494-C494M). West Conshohocken (PA): ASTM International.

Astutiningsih, S. & Liu, Y. (2005). Geopolymerisation of Australian slag with effective dissolution by the alkali. In *Proceedings of the World Congress Geopolymer* (pp.

69-73). Geopolymer Institute: Saint Quentin, France.

Bai, J., Chaipanich, A., Kinuthia, J.M., O'Farrell, M., Sabir, B.B., Wild, S. & Lewis, M.H. (2003). Compressive strength and hydration of wastepaper sludge ash–ground granulated blastfurnace slag blended pastes. *Cement and Concrete Research*, *33*(8), 1189-1202.

British Standards Institute [BSI] (2000). *Testing concrete. Part 116: Method for determination of compressive strength of concrete cubes* (BS 1881-116:1983). London: British Standards Institute.

Chowdhury, S., Maniar, A. & Suganya, O.M. (2015). Strength development in concrete with wood ash blended cement and use of soft computing models to predict strength parameters. *Journal of Advanced Research*, *6*(6), 907-913.

Davidovits, J. (2020). *Geopolymer chemistry and applications*. 5th ed. Saint-Quentin, France: Geopolymer Institute.

Duxson, P., Fernández-Jiménez, A., Provis, J.L., Lukey, G.C., Palomo, A. & van Deventer, J.S. (2007). Geopolymer technology: the current state of the art. *Journal of Materials Science*, *42*(9), 2917-2933.

Ekaputri, J.J. & Junaedi, S. (2017). Effect of curing temperature and fiber on metakaolin--based geopolymer. *Procedia Engineering*, *171*, 572-583.

Etiegni, L. & Campbell, A.G. (1991). Physical and chemical characteristics of wood ash. *Bioresource Technology*, *37*(2), 173-178.

Fairbairn, E.M., Americano, B.B., Cordeiro, G.C., Paula, T.P., Toledo Filho, R.D. & Silvoso, M.M. (2010). Cement replacement by sugar cane bagasse ash: CO_2 emissions reduction and potential for carbon credits. *Journal of Environmental Management*, *91*(9), 1864-1871.

Fernandez-Jimenez, A.M., Palomo, A. & Lopez--Hombrados, C. (2006). Engineering properties of alkali-activated fly ash concrete. *ACI Materials Journal*, *103*(2), 106-112.

Fernández-Jiménez, A., García-Lodeiro, I. & Palomo, A. (2007). Durable characteristics of alkali activated fly ashes. *Journal of Material Sciences*, *42*, 3055-3065.

Frías, M., García, R., Vigil, R. & Ferreiro, S. (2008). Calcination of art paper sludge waste for the use as a supplementary cementing material. *Applied Clay Science*, *42*(1-2), 189-193.

García, R., Villa, R.V. de la, Vegas, I., Frías, M. & Rojas, M.S. de (2008). The pozzolanic properties of paper sludge waste. *Construction and Building Materials*, *22*(7), 1484-1490.

Gartner, E. (2004). Industrially interesting approaches to "low-CO_2" cements. *Cement and Concrete Research*, *34*(9), 1489-1498.

Hardjito, D., Wallah, S.E., Sumajouw, D.M. & Rangan, B.V. (2004). On the development of fly ash-based geopolymer concrete. *Materials Journal*, *101*(6), 467-472.

Iraqi Central Agency for Standardization and Quality Control [ICASQC] (1984). *Iraqi standards for natural aggregate resources for concrete* (IQS 45/1984). Baghdad: Iraqi Central Agency for Standardization and Quality Control (translated from Arabic edition).

Ishimoto, H., Origuchi, T. & Yasuda, M. (2000). Use of papermaking sludge as new material. *Journal of Materials in Civil Engineering*, *12*(4), 310-313.

Letelier, V., Henríquez-Jara, B.I., Manosalva, M. & Moriconi, G. (2019). Combined use of waste concrete and glass as a replacement for mortar raw materials. *Waste Management*, *94*, 107-119.

Luga, E. & Peqini, K. (2019). The Influence of Oxide Content on the Properties of Fly Ash/Slag Geopolymer Mortars Activated with NaOH. *Periodica Polytechnica Civil Engineering*, *63*(4), 1217-1224.

Malaszkiewicz, D. & Jastrzebski, D. (2018). Lightweight self-compacting concrete with sintered fly-ash aggregate. *Scientific Review – Engineering and Environmental Sciences*, *27*(3), 328-337.

Mehta, A. & Siddique, R. (2018). Sustainable geopolymer concrete using ground granulated blast furnace slag and rice husk ash: Strength and permeability properties. *Journal of Cleaner Production*, *205*, 49-57.

Mozaffari, E., Kinuthia, J.M., Bai, J. & Wild, S. (2009). An investigation into the strength development of wastepaper sludge ash blended with ground granulated blastfurnace slag. *Cement and Concrete Research*, *39*(10), 942-949.

Naik, T.R., Kraus, R.N., & Siddique, R. (2003). Controlled low-strength materials containing mixtures of coal ash and new pozzolanic material. *Materials Journal*, *100*(3), 208-215.

Pachamuthu, S. & Thangaraju, P. (2017). Effect of incinerated paper sludge ash on fly ash-based geopolymer concrete. *Građevinar*, *69*(9), 851-859.

Rangan, B.V. (2008). *Fly ash-based geopolymer concrete*. Perth: Curtin University of Technology.

Risdanareni, P., Karjanto, A. & Khakim, F. (2016). Physical properties of volcanic ash based geopolymer concrete. *Materials Science Forum*, *841*, 1-6.

Ryu, G.S., Lee, Y.B., Koh, K.T. & Chung, Y.S. (2013). The mechanical properties of fly ash-based geopolymer concrete with alkaline activators. *Construction and Building Materials*, *47*, 409-418.

Shi, C., Wu, Y., Riefler, C. & Wang, H. (2005). Characteristics and pozzolanic reactivity of glass powders. *Cement and Concrete Research*, *35*(5), 987-993.

Tam, V.W., Soomro, M. & Evangelista, A.C.J. (2018). A review of recycled aggregate in concrete applications (2000–2017). *Construction and Building Materials*, *172*, 272-292.

Thaarrini, J. & Ramasamy, V. (2016). Properties of foundry sand, ground granulated blast furnace slag and bottom ash based geopolymers under ambient conditions. *Periodica Polytechnica Civil Engineering*, *60*(2), 159-168.

Turner, L.K., & Collins, F.G. (2013). Carbon dioxide equivalent (CO_2-e) emissions: A comparison between geopolymer and OPC cement concrete. *Construction and Building Materials*, *43*, 125-130.

Udoeyo, F.F., Inyang, H., Young, D.T. & Oparadu, E.E. (2006). Potential of wood waste ash as an additive in concrete. *Journal of Materials in Civil Engineering*, *18*(4), 605-611.

Summary

Use of waste paper ash or wood ash as substitution to fly ash in production of geopolymer concrete. Large quantities of paper and wood waste are generated every day, the disposal of these waste products is a problem because it requires huge space for their disposal. The possibility of using these wastes can mitigate the environmental problems related to them. This study presents an investigation on the feasibility of inclusion of waste paper ash (WPA) or wood ash (WA) as replacement materials for fly ash (FA) class F in preparation geopolymer concrete (GC). The developed geopolymer concretes for this study were prepared at replacement ratios of FA by WPA or WA of 25, 50, 75 and 100% in addition to a control mix containing 100% of FA. Sodium hydroxide (NaOH) solutions and sodium silicate (Na_2SiO_3) are used as alkaline activators with 1M and 10M of sodium hydroxide solution.The geopolymer concretes have been evaluated with respect to the workability, the compressive strength, splitting tensile strength and flexural strength. The results indicated that there were no significant differences in the workability of the control GC mix and the developed GC mixes incorporating WPA or WA. Also, the results showed that, by incorporating of 25–50% PWA or 25% WA, the mechanical properties (compressive strength, splitting tensile strength and flexural strength) of GC mixes slightly decreased. While replacement with 75–100% WPA or with 50–100% WA has reduced these mechanical properties of GC mixes. As a result, there is a feasibility of partial replacement of FA by up to 50% WPA or 25% WA in preparation of the geopolymer concrete.

Authors' address:
Haider Mohammed Owaid
(https://orcid.org/0000-0001-7252-5875)
University of Babylon
College of Engineering
Department of Civil Engineering
Al-Hillah – Al-Najaf Road, Babylon
Iraq
e-mail: eng.haider.ma@uobabylon.edu.iq
haidernccl@yahoo.com

Muna M. Al-Rubaye
University of Babylon
College of Engineering
Department of Civil Engineering
Al-Hillah – Al-Najaf Road, Babylon
Iraq
e-mail: eng.muna.mohamed@uobabylon.edu.iq

Haider M. Al-Baghdadi
University of Babylon
College of Engineering
Department of Civil Engineering
Al-Hillah – Al-Najaf Road, Babylon
Iraq
e-mail: eng.haider.m@uobabylon.edu.iq

Scientific Review – Engineering and Environmental Sciences (2021), 30 (3), 477–484
Sci. Rev. Eng. Env. Sci. (2021), 30 (3)
Przegląd Naukowy – Inżynieria i Kształtowanie Środowiska (2021), 30 (3), 477–484
Prz. Nauk. Inż. Kszt. Środ. (2021), 30 (3)
http://iks.pn.sggw.pl
DOI 10.22630/PNIKS.2021.30.3.40

Larap Kemayan ESTU, Betty SUSANTI, Febrian HADINATA

University of Sriwijaya, Faculty of Engineering

Operation and maintenance financial feasibility analysis of centralized domestic wastewater treatment system (case study: Palembang City Sewerage Project)

Key words: financial feasibility, wastewater, sewerage, operation and maintenance

Introduction

The lack of proper sanitation access in Indonesia, especially centralized domestic wastewater infrastructure, largely caused by budget insufficiency, for both construction and operation/ /maintenance cost (Kerstens, Legowo & Gupta, 2012; Pham & Kuyama, 2013; Kerstens, Leusbrock & Zeeman, 2015; Bergkamp, Setiadi, Adisurya & Lim, 2018). This condition led to high backlog for proper sanitation access (Bergkamp et al., 2018). Numerous studies have documented the importance of the financial feasibility on sewerage construction phase (Wedgwood & Sansom, 2003; OECD, 2004, 2007; Kerstens et al., 2012; Eales, Blackett, Siregar & Febriani, 2013; Kearton, 2013; Sugiana, 2013; Yengejeh, Davideh & Baqeri, 2014; Kerstens et al., 2015; McNamara, 2018; Wijaya & Soedjono, 2018; Fitriani, Putra & Juliantina, 2019).

While financially not beneficial, the centralized domestic wastewater infrastructure in Indonesia still built on economic benefit premise (Eales et al., 2013; Kearton, 2013). Main factor that made it not beneficial is the uncertainty on operation and maintenance phase (Kerstens et al., 2015). Low user tariff added with slow development for sewer connection, made the infrastructure built in past years become unproductive. Adding options such as grant or loan to elevate the financial feasibility on operation and maintenance phase thought to be effective to resolve the problems (Sugiana, 2013).

The aim of the research was to analyze the financial feasibility on operation and maintenance phase of Palembang City Sewerage Project using net present value (*NPV*), benefit cost ratio (*BCR*),

and internal rate of return (*IRR*) calculation based on cost and revenue variable. The satisfactory conditions are: $NPV > 0$, $BCR > 1$, and $IRR > MARR$. Should the conditions did not meet, follow up analysis to improve the results by calculate different scenarios should be done.

Material and methods

This research used Palembang City Sewerage Project Phase 1 as case study. Palembang City Sewerage Project is a project located in Palembang City, South Sumatra Province, Indonesia. The aim of this project is to solve the domestic wastewater problems in Palembang, by providing the centralised domestic wastewater treatment system in Palembang, that designed for 22,000 connections city-wide (KIAT, 2017). Phase 1 of Palembang City Sewerage Project starts in 2017 and will be finished in 2022 with 4,064 household and 2,229 commercial connection as main objective funded by Government of Indonesia Budget. The later expansion in Phase 2 to fill the maximum capacity of the wastewater treatment plant will be funded by the South Sumatra Provincial Budget and Palembang Municipality Budget in 2025.

Financial analysis on operation and maintenance of centralized domestic wastewater treatment system, emphasize on budget analysis to determine the feasibility of said phase financialy (Kvernberg, 2012; Yengejeh et al., 2014). Based on OECD (2004), the analysis needed to provide financing options and assurance when the operator solely dependent on tariff revenue to operate and maintain the system. The analysis also needed to prevent high idle capacity and fail system, caused by rejection to pay from the customers (Wedgwood & Sansom, 2003).

Based on previous study, cost and revenue variable chosen to be calculated for this project operation and maintenance financial feasibility. The revenue variable consists of household and commercial tariff, while the cost variable consist of: (a) chemical usage cost, (b) sludge disposal cost, (c) personnel wage cost, (d) fuel and electricity cost, and (e) spare-part replacement cost (OECD, 2004, 2007; van Buuren, 2010; Rosaria, 2010; Kvernberg, 2012; Sugiana, 2013; Kerstens et al., 2015; KIAT, 2017; McNamara, 2018; Fitriani et al., 2019).

During this research, first hand information on prices in Palembang was obtained during site visit and through discussions with involved stake-holders. The data obtained from the Ministry of Public Works and Housing (MOPWH) was willingness-to-pay survey results that involved 100 respondent, each from, household and commercial connection targets. As for cost variable data, were obtained from both MOPWH and PDAM Tirta Musi as the operator candidate for the system.

The analysis were calculated using discounted cash flow techniques (DCF) in worksheet computer application. The DCF was choosen because the calculation results affected by time value of money. Time value for money is a conjecture that money has different value in different period of time. The analysis should also: (a) simple to understand, (b) easy to calculate, (c) measures profitability, (d) ensures liquidity, (e) can adjust for risks, and (f) considers all cash flows (Bhandari, 2009; Maroyi, 2011). Thus the analysis calcu-

late net present value (*NPV*), benefit to cost ratio (*BCR*), and internal rate of return (*IRR*) to determine the feasability.

As previously stated, the financial feasibility was determined using *NPV*, *BCR*, and *IRR*. Net present value, presented in Eq. (1), is the difference between the present value of cash inflows (C_t) and the present value of cash outflows (C_o) over a period of time. All cash flows are discounted to present values using the required rate of return (r). The desirable result show by positive value of the calculation ($NPV > 0$). The applied currency rates based on Government of Indonesia official exchange rates were 14,500 Indonesian rupiah to 1 US dollar (Rp/USD). A 8.9% of discount rate for 20 years are applied in Eqs. (1) and (2).

$$NPV = \sum_{t=0}^{T} \left(\frac{C_t}{(1+r)^t} \right) - C_o \qquad (1)$$

Benefit to cost ratio defined as the ratio of the present value of future cash inflows to the cash outflows. Mathematically, this can be calculated using Eq. (2). The result deem satisfactory if the result is larger than one. Internal rate of return defined as the rate at which the net present value of project equals of zero. The satisfactory condition for the calculation met if the value of the calculated rate is larger than minimum acceptable rate of return ($IRR > MARR$). The use of *NPV*, *BCR*, and *IRR* calculation to determine the financial feasibility was applied by Prihandrijanti, Malisie and Otterpohl (2008), and Kerstens et al. (2015).

$$BCR = \frac{revenue\ PV}{cost\ \ PV} \qquad (2)$$

Follow up analysis to improve the feasibility taken when the satisfactory conditions did not met. The aim of follow up analysis was to improve the result of *NPV*, *BCR*, and *IRR* calculations to meet the satisfactory conditions. Following scenarios is choosen based on input from PDAM Tirta Musi as operator candidate for follow up analysis: (a) tariffs adjustment analysis, (b) analysis on adding grant as option, and (c) analysis on adding loan as option.

Results and discussion

Base assumption

The input data for the calculation, shown in Table 1, consists of base assumption of cost and revenue variable. Using the data provided, *NPV*, *BCR*, and *IRR* then calculated and showed these results: *NPV* = USD – 4,239,448.28, *BCR* = 0.8719, and *IRR* = –5%. These results did not meet the satisfactory conditions, thus the follow up analysis to improve the results taken.

Follow up analysis

1. Tariff adjustment
   Tariff adjustment analysis was taken to determine minimum tariff to meet the satisfactory conditions. The tariff adjustment calculation done with following conditions: (a) adjust household tariff with 100% increment, while commercial tariff fixed, and (b) adjust commercial tariff with 10% increment, while household tariff is fixed. The result presented in Table 2.

TABLE 1. Base assumption of cost and revenue variable (MOPWH and PDAM Tirta Musi)

Variable		Value [USD]
Cost	chemical usage	6 896.55 per month = 82 758.62 per year
	sludge disposal	1 022 400 per year
	personnel wage	3 655.17 per month = 43 862.07 per year
	fuel and electricity	14 513.79 per month = 174 165.52 per year
	spare-part replacement	10 344.83 per year; 689 655.17 per 10 year; 13 793 103.45 per 20 year
	depreciation (flat)	2 068 965.52 per year
Revenue	household tariff	0.76 per month
	commercial tariff	20.69 per month
	installation cost (1 time)	344.83

TABLE 2. Tariff adjustment analysis (own studies)

Tariff base assumption [USD]		Tariff adjustment [USD]		Escalation [%]
Household	0.76	$NPV > 0$, $BCR > 1$	8.28	1 000
		$IRR > MARR$	26.21	3 355
Commercial	20.69	$NPV > 0$, $BCR > 1$	31.03	50
		$IRR > MARR$	60.00	190

As shown in Table 2, the tariff adjustment for household to meet satisfactory condition of *NPV* and *BCR* is 1,000% increase from base tariff, and to meet the satisfactory condition of *IRR* the tariff need to increase 3,355%. For the commercial tariff, minimum 50% escalation from base tariff needed to meet *NPV* and *BCR* desirable results, and 190% escalation to make the *IRR* > *MARR*.

2. Grant
   Adding grant as option to improve the feasibility was calculate as shown in Tables 3 and 4, following these scenarios:
   a. Grant for sewer connection expansion
      Grant that given one time to expand the sewer connection until reached the maximum amount of 22,000 sewer connection.
   b. Grant for tariff subsidy
      Recurring grant to give subsidy for base tariff, in order to prevent financial loss for sewerage operator.

As stated on the calulations in Tables 3 and 4, the total grant needed to achieve maximum sewer connection is 5,416,207 USD for 20 years or annually 270,810.35 USD. The amount of grant needed for subsidy is bigger compared to the grant needed for sewer expansion.

TABLE 3. Grant for sewer connection expansion (own studies)

Scenario	Connection type	Number of connections	*NPV* [USD]	*BCR*	*IRR* [%]	Total grant [USD]
Base asumption	household	4 064	–4 239 448	0.87	–5	–
	commercial	2 229				
Maximum household connection	household	19 771	20 719 103	1.64	13	5 416 207
	commercial	2 229				
Maximum commercial connection	household	4 064	43 270 207	2.33	23	5 416 207
	commercial	17 936				

TABLE 4. Grant for tariff subsidy (own studies)

Connection type	Number of connections	Base tariff	Tariff adjustment	Monthly subsidy	Annual subsidy	*NPV*	*BCR*	*IRR* [%]
		[USD]						
Household	4 064	0.76	8.28	30 550.07	366.600.83	211 517.24	1.01	0
			26.21	103 421.79	1 241 061.52	11 383 655.17	1.35	9
Commercial	2 229	20.69	31.03	23 058.62	276 703.45	646 206.90	1.02	1
			60.00	87 622.76	1 051 473.10	11 488 551.72	1.35	9

3. Loan
   Adding loan as option to improve the feasibility, shown in Table 5, was calculate using these scenarios:
   a. Loan for 100% maximum household connection expansion, with 20 years flat reimbursement.
   b. Loan for 50% maximum household connection expansion + + grant for 50% maximum household connection expansion, with 20 years flat reimburesment.
   c. Loan for 75% maximum household connection expansion + + grant for 25% maximum household connection expansion, with 20 years flat reimburesment.
   d. Loan for 100% maximum commercial connection expansion, with 20 years flat reimbursement.
   e. Loan for 50% maximum commercial connection expansion + grant for 50% maximum commercial connection expansion, with 20 years flat reimburesment.
   f. Loan for 75% maximum commercial connection expansion + grant for 25% maximum commercial connection expansion, with 20 years flat reimburesment.

Based on Table 5, adding loan is proven to improve the financial feasibility, shown by the improvement on *NPV*, *BCR*, and *IRR* calculation results.

TABLE 5. Loan analysis for Palembang City Sewerage Project (own studies)

Scenario		Number of connections		Loan	Grant	*NPV*	*BCR*	*IRR* [%]
		household	commercial	[× 1 000 USD]				
a	Maximum household, 100% loan	19 771	2 229	5 416.21	–	17 833.65	1.51	11
b	Maximum household, 50% loan + 50% grant	19 771	2 229	2 708.10	2 702.70	19 185.34	1.57	12
c	Maximum household, 75% loan + 25% grant	19 771	2 229	3 712.07	1 699.04	18 659.17	1.55	11
d	Maximum commercial, 100% loan	4 064	17 936	5 416.21	–	33 053.74	1.95	17
e	Maximum commercial, 50% loan + 50% grant	4 064	17 936	2 708.10	2 694.63	34 386.30	2.03	19
f	Maximum commercial, 75% loan + 25% grant	4 064	17 936	3 870.00	1 536.98	33 767.14	1.99	18

Furthermore, the combination of loan and grant to expand both household and commercial connection shows a better results compared to expansion solely funded by loan.

Conclusions

The financial feasibility value of Palembang City Sewerage Project calculated based on base tariff for operation and maintenance phase, shows negative result. The budget needed for the operation and maintenance phase for Palembang City Sewerage Project was 2,450,620 USD or annually 78 USD per capita, it was bigger than the results found in Kerstens et al. (2015) for annually 16 USD per capita, or annually 8.5 USD per capita in Prihandrijanti et al. (2008).

Low user charge tariff makes the financial feasibility results did not meet satisfactory condition. Improvement using tariff adjustment found that a minimum of 1,000% for household tariff and 50% for commercial tariff needed to make the *NPV* and *BCR* results accepted. And further 3,355% and 190% escalation for household and commercial tariff needed to meet satisfactory conditions of *NPV*, *BCR*, and *IRR*.

These results need to be advocated to the user, to prevent rejection of willingness to pay from the user. It means that the external factor plays a large portion for the decision making, and the success rate is low for tariff escalation based on previous research (OECD, 2004; Prihandrijanti et al., 2008; van Buuren, 2010; Kerstens et al., 2012; Sugiana, 2013; Kerstens et al., 2015).

From authors' point of view, the options using combination of grant and loan is the best choice. The sewerage operator can make business plan and search for loan and grant to get the budget needed for both business expansions as well for operation and maintenance budget.

Acknowledgements

The authors thank the Ministry of Public Works and Housing, Working Unit of Human Settlement Implementation of South Sumatra and PDAM Tirta Musi Palembang for fruitful discussion and sharing of data.

References

Bergkamp, G., Setiadi, T., Adisurya, T. & Lim, J. (2018). *Wastewater management and resource recovery in Indonesia.* Nyon: ARCOWA.

Bhandari, S.B. (2009). *Discounted payback period-some extensions*. Las Vegas: ASBSS.

Buuren, J. van (2010). *Sanitation choice involving stakeholders. A participatory multi-criteria method for drainage and sanitation system selection in developing cities applied in Ho Chi Minh City, Vietnam.* Wageningen: Wageningen University.

Eales, K., Blackett, I., Siregar, R. & Febriani, E. (2013). *Review of community-managed decentralized wastewater treatment systems in Indonesia.* Washington: World Bank.

Fitriani, H., Putra, F. & Juliantina, I. (2019). *Economic analysis of the wastewater treatment plant.* Bali: MATEC Web Conferences.

Kearton, R. (2013). *East Asia Pacific Region Urban Sanitation Review, Indonesia Country Study.* Washington: World Bank.

Kerstens, S., Legowo, H. & Gupta, I.B. (2012). Evaluation of DEWATS in Java, Indonesia. *Journal of Water, Sanitation and Hygiene for Development*, *2*(4), 254-265.

Kerstens, S., Leusbrock, I. & Zeeman, G. (2015). Feasibility analysis of wastewater and solid waste systems for application in Indonesia. *Science of the Total Environment*, *531*, 53-65.

KIAT (2017). *Project Design Document Palembang City Sewerage Project.* Jakarta: KIAT.

Kvernberg, E.B. (2012). *Performance assessment of a wastewater treatment plant in Kumasi, Ghana.* Oslo: Norwegian University of Life Science.

Maroyi, V. (2011). *Capital budgeting practices: a South African perspective.* Wageningen: Wagenigen University.

McNamara, G. (2018). *Economic and evironmental cost assessment of wastewater treatment systems. A life cycle perspective.* Dublin: Dublin City University.

Organisation for Economic Co-operation and Development [OECD] (2004). *Financing strategy of the urban wastewater in selected municipalities of the Sichuan Province in China.* Paris: OECD.

Organisation for Economic Co-operation and Development [OECD] (2007). *Feasible financing strategies for water supply and sanitation.* Paris: OECD.

Pham, N.B. & Kuyama, T. (2013). *Community--based sanitation lessons learned from SANIMAS programme in Indonesia.* Kanagawa: WEPA.

Prihandrijanti, M., Malisie, A. & Otterpohl, R. (2008). Cost benefit analysis for centralized and decentralized wastewater treatment system (case study: Surabaya-Indonesia). In I. Al Baz, R. Otterpohl, C. Wendland (eds.), *Efficient Management of Wastewater – Its Treatment and Reuse in Water-Scarce Countries* (pp. 259-268). Berlin: Springer.

Rosaria, F. (2010). *A rapid assessment of septage management in Asia. Policies and practies in India, Indonesia, Malaysia, the Philippines, Sri Lanka, Thailand, and Vietnam.* Los Angeles: AECOM.

Sugiana, K. (2013). *Feasibility analysis of the Wastewater Treatment Plant (WWTP) – PPP Project in DKI Jakarta.* Bogor: Restpent Press.

Wedgwood, A. & Sansom, K. (2003). *Willingness-to-pay surveys, a stremlined approach.* Loughborough: Loughborough University.

Wijaya, I.M.W. & Soedjono, E.S. (2018). Domestic wastewater in Indonesia: challenge in the future related to nitrogen content. *International Journal of Geomate*, *15*(47), 32-41.

Yengejeh, R., Davideh, K. & Baqeri, A. (2014). Cost/benefit evaluation of wastewater treatment plant types (SBR, MLE, Oxidation Ditch), case study: Khouzestan, Iran. *Bulletin of Environment, Pharmacology and Life Sciences*, *4*(1), 55-60.

Summary

Operation and maintenance financial feasibility analysis of centralized domestic wastewater treatment system (case study: Palembang City Sewerage Project). Budget needed for operation and maintenance of centralized domestic wastewater management in Indonesia is often overlooked. This results in fail systems, high idle capacity, and abandoned assets. While the economic feasibility often used as the basis for centralized domestic wastewater infrastructure construction, the financial feasibility often shown a different result. The construction phase will be feasible according the analysis, while the operation and maintenance phase will have a different result. As unsolicited projects, the operation and maintenance of sewerage in Indonesia always have budget difficulties, thus needed scenario to resolve the matter. In this study, cost and revenue variable will be analyzed to determine the feasibility value based on *NPV*, *BCR*, and *IRR* calculations. The revenue comes from user charge tariffs on household and commercials connections, and cost variable consists of: chemical usage cost; sludge disposal cost; personnel wage cost; fuel and electricity cost; spare-part replacement cost. The analysis will determine whether both household connection and commercials connection in the sewerage system have positive results. Should negative results emerged, follow up analysis added to elevate the results consists of following scenarios: sensitivity analysis for tariffs adjustment; sensitivity analysis adding grant as option; sensitivity analysis adding loan as option. While analysis of base tariffs shown negative results on *NPV*, *BCR*, and *IRR* calculation, the follow up analysis shown significant changes thus the results is desirable.

Authors' address:
Larap Kemayan Estu
University of Sriwijaya
Faculty of Engineering
Civil Engineering Department
Jalan Srijaya Negara, Bukit Besar, Palembang
30139
Indonesia

Betty Susanti – corresponding author
(https://orcid.org/0000-0002-6705-3591)
University of Sriwijaya
Faculty of Engineering
Civil Engineering Department
Jalan Srijaya Negara, Bukit Besar, Palembang
30139
Indonesia
e-mail: bettysusanti0401@gmail.com

Febrian Hadinata
(https://orcid.org/0000-0002-9637-006X)
University of Sriwijaya
Faculty of Engineering
Civil Engineering Department
Palembang, South Sumatra
Indonesia

Scientific Review – Engineering and Environmental Sciences (2021), 30 (3), 485–495
Sci. Rev. Eng. Env. Sci. (2021), 30 (3)
Przegląd Naukowy – Inżynieria i Kształtowanie Środowiska (2021), 30 (3), 485–495
Prz. Nauk. Inż. Kszt. Środ. (2021), 30 (3)
http://iks.pn.sggw.pl
DOI 10.22630/PNIKS.2021.30.3.41

Noora SAAD[1], Samara Al-DULAIMI[2]

[1] Al-Nahrain University, College of Engineering
[2] University of Zakho, Faculty of Science

Removal of Meropenem by using *Lemna minor*

Key words: kinetic models, biodegradation, *Lemna minor*, Meropenem

Introduction

Rapeutic drugs are a class of anthropogenic substances that are an emerging issue about pollution of the environment. Antibiotics are therapeutic organic compounds that can be produced by particular microorganisms as secondary metabolites, or can be generated artificially or semi-artificially (Phillips, 2003). Antibiotics exert antibacterial activity by altering the basic metabolic pathways of bacteria (Girardi et al., 2011).

These compounds are commonly used in human medicine for the prevention of bacterial infections, in agriculture for the fight against plant pathogens, in the veterinary industry and in aquaculture for the control of pathogenic agents. Antibiotics, however, are also used as growth promoters (Nunes, Veiga, Frankenbach, Serôdio & Pinto, 2019).

This number contains both human and veterinary antibiotics, most of which are antibiotics for veterinary purposes (Thiele-Bruhn, 2003). For all the reasons previously studied, the increasing concentration of antibiotics in the environment resulted from the increased use of such products.

Although not present in high concentrations, widespread dissemination of such materials has recently been observed, particularly in the aquatic environment. Generally, urine and feces are the primary sources of unchanged types of prescription drugs in nature after the excretion of pharmaceutical materials. This helps, with or without treatment, these chemicals to enter waste water (Nunes et al., 2019).

In certain countries, excrete-containing waste water and drug residues are processed at wastewater treatment

plants where they can be contaminated or absorbed by sludge treatment (Faisal, Nassir, Naji, Naushad & Ahamad, 2020; Naji, Faisal, Rashid, Naushad & Ahamad, 2020; Rahi et al., 2020; Saad, Abd Ali, Naji, Faisal & Al-Ansari, 2020). The danger of such pharmaceuticals is subjected to the surface when the contaminated wastewater is not treated successfully or not treated at all (Karthikeyan & Meyer, 2006; Alshammari et al., 2020).

Many engineering developments, including coagulation, floatation, chemical reduction, oxidation, photochemical degradation, and microbial remediation, have been proposed to address these issues by eliminating antibiotics from habitats (Abd Ali et al., 2020; Ahmed, Naji, Faisal, Al-Ansari & Noushad, 2020; Naji, Jassam, Yaseen, Faisal & Al-Ansari, 2020).

The utility of plants has grown over the years in the biological remediation of pollutants. In the literature, many plant species with the ability to eliminate a wide range of environmental pollutants have been recorded (Sekulic et al., 2019; Ahmed, Faisal, Jassam, Naji & Naushad, 2020; Naji, Jassam et al., 2020).

The one given by Zhao et al. (2010) in which *Lemna minor* was tested is another example of using plants to mitigate the impact of pharmaceuticals in practical circumstances. The plant showed a strong response to large amounts of both absorbing and metabolizing pharmaceuticals. The conditions in which the plants have been tested are made as similar as possible to the environmental conditions under which they will be subjected. Therefore, the objective of this research is to study the photototoxicity of Meropenem on *Lemna minor* for different Meropenem concentrations from 1 June 2020 to 15 July 2020.

Material and methods

Lemna minor

In Steinberg medium, *Lemna minor* cultures were produced in controlled laboratory conditions at 25 ±2°C. The plant was subjected to continuous light to tolerate to the new environment for five days prior to the beginning of the test in order to allow plant acclimatization to the conditions needed by the adopted test guidelines. The *Lemna minor* was subsequently exposed to a series of three concentrations of Meropenem for five days. Meropenem standard stock solutions have been prepared in water at a concentration of 1,000 $mg \cdot L^{-1}$ and held in amber screw-capped glass vials in darkness at a temperature of –20°C for a period of seven days (Faisal, Al-Wakel, Assi, Naji & Naushad, 2020).

The concentrations selected were 0.01, 0.05, and 0.1 $mg \cdot L^{-1}$. The operation process was based on the operation of the built wetland as batch reactors for different influencer concentrations for the period from 1 June 2020 to 15 July 2020 as previously mentioned. The batch experiments were carried out with a period of detention equal to five days. At the Ministry of Science and Technology, the sample concentration of water was measured. Liquid samples were obtained and the Meropenem was centrifuged and musurified using high-performance liquid chromatography (HPLC).

Results and discussion

The removal efficiencies for different initial concentrations (0.01, 0.05, and 0.1 mg·L^{-1}, respectively) of *Lemna* spp. CW are shown in Figure 1. Each concentration was tracked for two months in this figure (from June 1st to July 31st). To take the readings, a check point was set every two weeks. At each check point, the readings were taken as five-day shipments (the check points assigned were June 1st, June 15th, July 1st, and July 15th). For better clarification, each initial concentration was placed into a separate figure.

Removal efficiencies have shown that the detention period has risen from one day to five days. The removal efficiency values for *Lemna* spp. samples for the first period (1 June 2020) were 83.1, 85.1, 86.3, 87.4 and 88.4 for the first period (1 June 2020) and 57.4, 58.4, 61.5, 62.5 and 63.5 (15 July 2020) for the last period, corresponding to 0.1 mg·L^{-1} for each period and initial concentration, respectively.

The efficiency of the *Lemna* spp. system was very good, with overall removal efficiencies ranging from 58.4% for Meropenem to 88.4% for both under low concentration. The removal efficiency values for *Lemna* spp. samples were 88.4 for the first period and 63.5 for the last period corresponding to the 5th and the initial concentration was 0.1 mg·L^{-1}, compared with the removal efficiency of Meropenem for the first and last periods for the last day (5th). In this analysis, as the concentration used, the decrease in removal efficiency reported in *Lemna* spp. systems could also be attributed to that toxic effect.

The removal efficiency values for *Lemna* spp. samples decreased from 95.3 to 88.4 relative to the removal efficiency of Meropenem when the initial concentration rose from 0.01 to 0.1 mg·L^{-1} for the first cycle and the last day (5th), respectively. These findings indicate that the content of Meropenem medium in the plant continues to increase. In duckweed, high doses of Meropenem induce the synthesis of few metabolites (starch, protein, polypeptic, etc.) that could lead to excess biomass in such configurations. Few previous workers have also documented the physiological alternation and inhibition of enzymatic pathways in plants subjected to elevated Meropenem load, indicating the adverse effect of elevated Meropenem content on the functioning of the plan (Białk-Bielińska et al., 2018).

To run the system at the optimal scale, the load in the duckweed-based phytoremediation system should be optimized (Verma & Suthar, 2015). The results confirmed that the presence of *Lemna* spp. in the units for adopted concentrations would increase the reduction of Meropenem because *Lemna* spp. will provide the required environment for phytoremediation growth within the root zone and other parts of *Lemna* spp. (Kouki, M'hiri, Saidi, Belad'd & Hassen, 2009). Plants have a photosystem responsible for light harvesting and energy transfer to the act (Baker 2008; Faisal, Alquzweeni, Naji & Naushad, 2020). Bacteria was also reduced in contamination level. This could be as a result of biochemical activities of the indigenous microbes within the wastewater which tend to use up the pollutants in the wastewater (Rakhshaee, Giahi & Pourahmad, 2009).

a) Concentration = 0.01 mg·L^{-1}

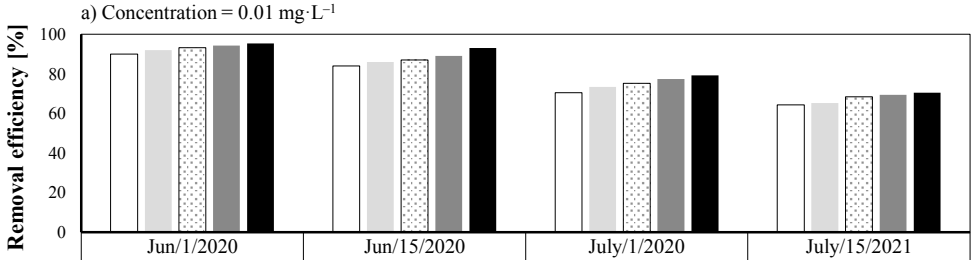

	Jun/1/2020	Jun/15/2020	July/1/2020	July/15/2021
1 Day	90	84	70.4	64.3
2 Day	92	86	73.4	65.3
3 Day	93.2	87	75.2	68.4
4 Day	94.3	89	77.4	69.4
5 Day	95.3	93	79.2	70.4

b) Concentration = 0.05 mg·L^{-1}

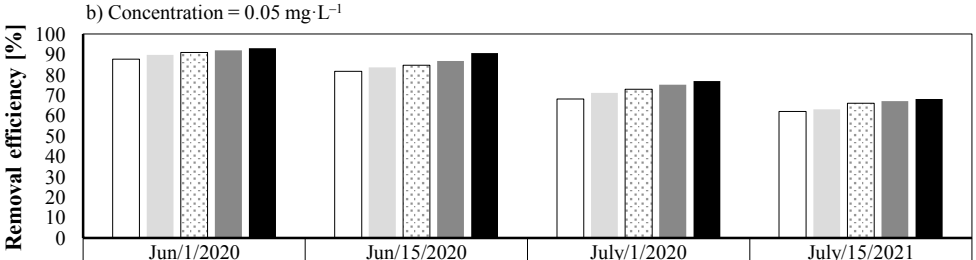

	Jun/1/2020	Jun/15/2020	July/1/2020	July/15/2021
1 Day	87.7	81.7	68.1	62
2 Day	89.7	83.7	71.1	63
3 Day	90.9	84.7	72.9	66.1
4 Day	92	86.7	75.1	67.1
5 Day	93	90.7	76.9	68.1

c) Concentration = 0.1 mg·L^{-1}

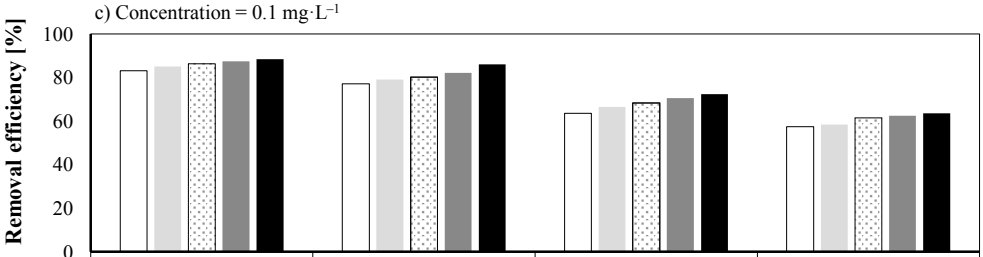

	Jun/1/2020	Jun/15/2020	July/1/2020	July/15/2021
1 Day	83.1	77.1	63.5	57.4
2 Day	85.1	79.1	66.5	58.4
3 Day	86.3	80.1	68.3	61.5
4 Day	87.4	82.1	70.5	62.5
5 Day	88.4	86.1	72.3	63.5

FIGURE 1. Constant initial concentration (0.01, 0.05 and 0.1 mg·L^{-1}) removal efficiencies of Meropenem in CW of *Lemna* spp.

These photosystems have very effective light harvesting processes, simultaneously preventing photosynthetic photo-oxidative damage. This may occur during periods of intense light, and photosynthetic organisms have evolved different defensive mechanisms to cope with it (Jahns & Holzwarth, 2012; Faisal, Ibreesam et al., 2020). There are two key pathways for chloroplasts: electron transfer to molecular oxygen leading to the formation of O_2, H_2O_2 and hydroxyl radicals (O percent H) (Halliwell, 2007), and a second pathway involving the transfer of energy from triplet chlorophyll to molecular oxygen leading to the formation of superoxide radicals (O^{-}_2) (Nunes et al., 2019).

In plants, O^{-}_2 is naturally generated during photosynthesis in chloroplasts, particularly when plants develop under conditions of environmental stress that inhibit photosynthetic processes, causing excessive absorption of light energy (Nunes et al., 2019; Faisal, Jasim, Naji, Naushad & Ahamad, 2021).

Meropenem is believed to interfere with the electron transport chain leading to the formation of oxidized chlorophyll triplets capable of transferring energy directly to the O_2 molecule, which in turn has a dual effect on plant cells resulting in the oxidation of biomolecules, including lipids (which are structural elements of the cell membranes), but also proteins with a dual effect on plant cells (Ramel et al., 2012; Faisal & Naji, 2019).

However, can ultimately endanger the normal physiology of plants. That is why defensive/adaptive mechanisms among plant species are highly elaborate. Catalase is a key enzyme that plays an essential role in the degradation of hydrogen peroxide. This enzyme serves as a protector for the species against the deleterious oxidant effects that can be caused by this chemical (Nunes, Verde & Soares, 2015).

In cells, catalase is still involved to prevent damage caused by the normal formation of H_2O_2 during aerobic processes that are part of the cell's physiological activity. An rise in the levels of hydrogen peroxide is overserved, but due to the metabolism mechanism of certain chemicals, it may result from the occurrence of oxidative stress. This is immediately followed by increased catalase activity, which acts as a physiological compensation during conditions of oxidative stress (Nunes et al., 2019) according to Gomes et al. (2017). There was a noticeable increase in peroxide concentration and a large increase in catalase activity in minor plants after 0.75 $mg \cdot L^{-1}$ of ciprofloxacin was exposed for one week. These data agree with the pattern that has been collected here. This data set indicates that biomolecules are influenced by reactive oxygen species that ultimately result from Meropenem's metabolism.

Chemical oxygen demand (COD) and root length

By weighing COD, the content of organic matter was determined. A commercial Hach package (2125915 COD HR) was added to this purpose, according to the US EPA System 410.4 (EPA, 1993). This process relies on the oxidation of the organic compounds, which has been quantified at 610 nm based on the potential to reduce the dichromate ion to chroma ions. A multiparametric Hanna

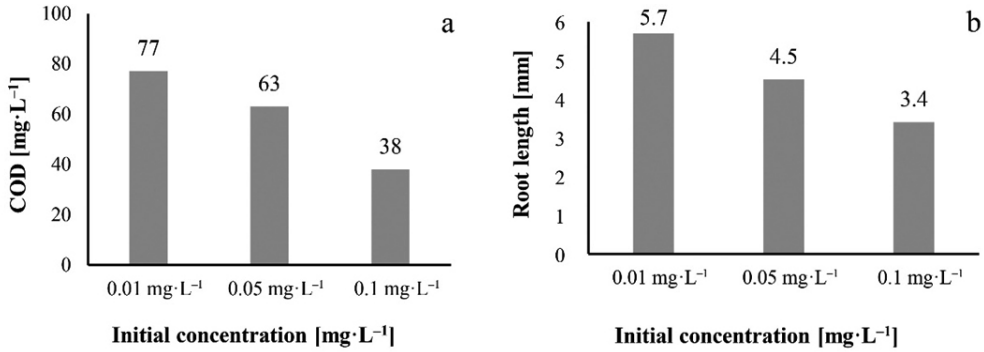

FIGURE 2. The removal efficiencies of chemical oxygen demand (COD) and root length with different initial concentration (0.01, 0.05 and 0.1 mg·L^{-1}) for Meropenem in CW of *Lemna* spp.

spectrophotometer (HI 83214 model) was used to evaluate the absorbance values that precisely fit COD (mg·L^{-1}) levels. The parameters evaluated for varying concentrations and the removal increases were found in the raw material with reduced concentration for the chemical oxygen (Fig. 2).

Kinetics of biodegradation

Kinetic is a critical factor for understanding the biodegradation process, calculating the speed of bioremediation and creating effective clean up for a polluted area. A set of empirically derived rate laws is the kinetics of biodegradation. The three lists in Table 1 are enough to explain most biological reactions.

Using zero-order, first-order, second-order and Grau kinetic models, the removal data is represented. In order to achieve non-linear fitting, zero--order, first-order and second-order kinetic models have a small application for bio removal of various Meropenem concentrations by applying the "solver" option in Excel 2016. In order to analyze the kinetics for biodegradation processes, the final concentration to intial concentration of Meropenem in the sand was also plotted against time as shown in the figure. The biodegradation kinetics of kerosene were analyzed using the kinetic models described in Figures 3a, 3b and 3c for 0.01, 0.05 and 0.1 mg·L^{-1}, respectively.

Although there was not a very strong agreement with the experimental data in the zero-order, first-order, and second-order models, the Grau model showed a very good contrast to the collected experimental data.

TABLE 1. Mathematical kinetic models

Model	Mathematical formula
Zero order	$C = C \cdot - kt$
First order	$C = C \cdot e^{-kt}$
Second order	$C = \frac{C}{1 + C \cdot kt}$
Grau	$C = C \cdot \left(1 - \frac{1}{b + \frac{a}{t}}\right)$

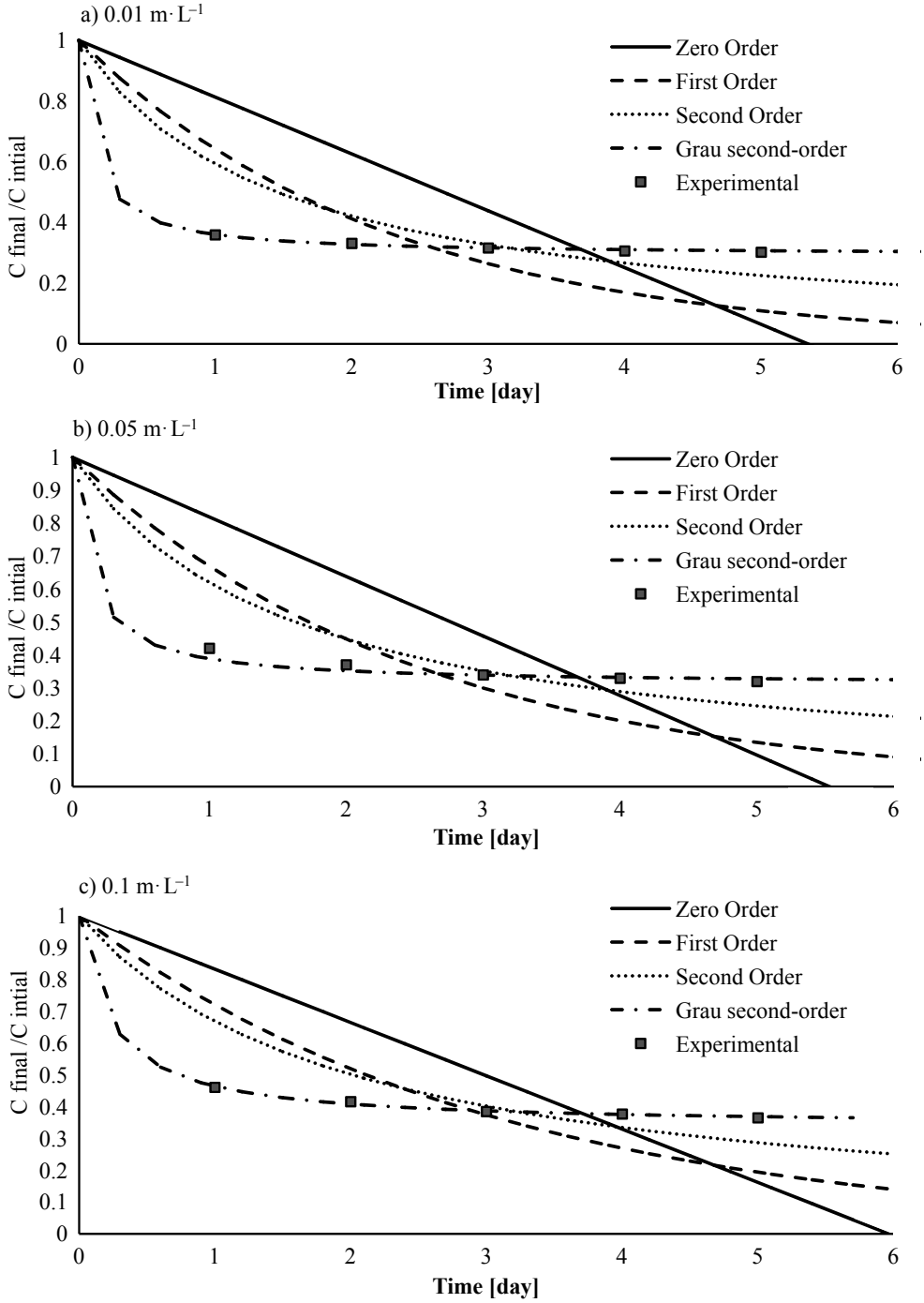

FIGURE 3. Kinitic model of plant system for different initial concentration (0.01, 0.05 and 0.1 mg·L^{-1})

Compared to other methods, the information collected separately for each of the kinetic models from the slopes of plots indicates a strong compliance with the second-order model. In Table 2, however, all constants resulting from fitting with R^2 and *SSE* were added. The listed figures show that there is a satisfactory correspondence between experimental results and model predictions, as is evident from the *SSE* values in combination with R^2.

options currently available to the petrochemical industry.

This research has shown that *Lemna minor*, an invasive aquatic plant abundant in surface waters throughout the world, has a great potential to ecologically remediate and extract a large amount of Meropenem from polluted waters. The plant was able to absorb and degrade Meropenem from wetlands. However, it was not possible to completely elucidate these processes due to the uncertainty

TABLE 2. Parameter of kinetics model for plant system

Model	Parameter	Intial concentration [mg·L^{-1}]		
		0.01	0.05	0.1
First order	k	0.4440	0.4020	0.3278
	R^2	0.9954	0.9846	0.9779
	SSE	0.0000	0.0003	0.0012
Second order	k	68.8890	12.3272	4.9683
	R^2	0.9982	0.9924	0.9901
	SSE	0.0000	0.0000	0.0002
Zero order	k	0.0019	0.0090	0.0168
	R^2	0.9034	0.8843	0.8964
	SSE	0.0000	0.0007	0.0026
Grau	a	0.1496	0.1823	0.3525
	b	1.4128	1.4509	1.5138
	R^2	0.9835	0.9878	0.9850
	SSE	0.0000	0.0000	0.0000

Conclusions

The treatment of contaminated wetlands with Meropenem using traditional methods attracts concern from some parts of society, while ecological approaches are considered with minimal

of the fate and the transformation/mineralization processes of Meropenem by *Lemna minor*. For 0.01, 0.05 and 0.1 mg·L^{-1} influential concentration, the variation of effluent concentration with hydraulic retention time for all units under consideration was well defined by

the Grau second-order kinetic model. It is therefore suggested that studies should be carried out to explain the underlying mechanisms of degradation, conversion and mineralization by *Lemna minor* of Meropenem.

References

Abd Ali, Z.T., Naji, L.A., Almuktar, S.A., Faisal, A.A., Abed, S.N., Scholz, M., Naushad, M. & Ahamad, T. (2020). Predominant mechanisms for the removal of nickel metal ion from aqueous solution using cement kiln dust. *Journal of Water Process Engineering*, *33*, 101033. https://doi.org/10.1016/j.jwpe.2019.101033

Ahmed, D.N., Faisal, A.A., Jassam, S.H., Naji, L.A. & Naushad, M. (2020). Kinetic model for pH variation resulted from interaction of aqueous solution contaminated with nickel ions and cement kiln dust. *Journal of Chemistry*, *2020*, 8732308. https://doi.org/10.1155/2020/8732308

Ahmed, D.N., Naji, L.A., Faisal, A.A., Al-Ansari, N. & Naushad, M. (2020). Waste foundry sand/MgFe-layered double hydroxides composite material for efficient removal of Congo red dye from aqueous solution. *Scientific Reports*, *10*(1), 1-12.

Alshammari, M., Al Juboury, M.F., Naji, L.A., Faisal, A.A., Zhu, H., Al-Ansari, N. & Naushad, M. (2020). Synthesis of a novel composite sorbent coated with siderite nanoparticles and its application for remediation of water contaminated with Congo red dye. *International Journal of Environmental Research*, *14*, 177-191.

Baker, N.R. (2008). Chlorophyll fluorescence: a probe of photosynthesis in vivo. *Annual Review of Plant Biology*, *59*, 89-113.

Białk-Bielińska, A., Matzke, M., Caban, M., Stolte, S., Kumirska, J. & Stepnowski, P. (2018). Effects of five sulphonamides on duckweed (*Lemna minor*) after prolonged exposure time and their dependency on photoradiation. *Science of the Total Environment*, *618*, 952-960.

Faisal, A.A., Alquzweeni, S.S., Naji, L.A. & Naushad, M. (2020). Predominant mechanisms in the treatment of wastewater due to interaction of benzaldehyde and iron slag byproduct. *International Journal of Environmental Research and Public Health*, *17*(1), 226. https://doi.org/10.3390/ijerph17010226

Faisal, A.A., Al-Wakel, S.F., Assi, H.A., Naji, L.A. & Naushad, M. (2020). Waterworks sludge-filter sand permeable reactive barrier for removal of toxic lead ions from contaminated groundwater. *Journal of Water Process Engineering*, *33*, 101112. https://doi.org/10.1016/j.jwpe.2019.101112

Faisal, A.A., Ibreesam, M.M., Al-Ansari, N., Naji, L.A., Naushad, M. & Ahamad, T. (2020). COMSOL multiphysics 3.5 a package for simulating the cadmium transport in the sand bed-bentonite low permeable barrier. *Journal of King Saud University – Science*, *32*(3), 1944-1952.

Faisal, A.A., Jasim, H.K., Naji, L.A., Naushad, M. & Ahamad, T. (2021). Cement kiln dust-sand permeable reactive barrier for remediation of groundwater contaminated with dissolved benzene. *Separation Science and Technology*, *56*(5), 870-883.

Faisal, A.A. & Naji, L.A. (2019). Simulation of ammonia nitrogen removal from simulated wastewater by sorption onto waste foundry sand using artificial neural network. *Association of Arab Universities Journal of Engineering Sciences*, *26*(1), 28-34.

Faisal, A.A., Nassir, Z.S., Naji, L.A., Naushad, M. & Ahamad, T. (2020). A sustainable approach to utilize olive pips for the sorption of lead ions: numerical modeling with aid of artificial neural network. *Sustainable Chemistry and Pharmacy*, *15*, 100220. https://doi.org/10.1016/j.scp.2020.100220

Girardi, C., Greve, J., Lamshöft, M., Fetzer, I., Miltner, A., Schäffer, A. & Kästner, M. (2011). Biodegradation of ciprofloxacin in water and soil and its effects on the microbial communities. *Journal of Hazardous Materials*, *198*, 22-30.

Gomes, M.P., Gonçalves, C.A., Brito, J.C.M. de, Souza, A.M., Silva Cruz, F.V. da, Bicalho, E.M., Figueredo, C.C. & Garcia, Q.S. (2017). Ciprofloxacin induces oxidative stress in duckweed (*Lemna minor* L.): implications

for energy metabolism and antibiotic-uptake ability. *Journal of Hazardous Materials*, *328*, 140-149.

Halliwell, B. (2007). Biochemistry of oxidative stress. *Biochemical Society Transactions*, *35*, 1147-1150.

Jahns, P. & Holzwarth, A.R. (2012). The role of the xanthophyll cycle and of lutein in photoprotection of photosystem II. *Biochimica et Biophysica Acta (BBA) – Bioenergetics*, *1817*(1), 182-193.

Karthikeyan, K.G. & Meyer, M.T. (2006). Occurrence of antibiotics in wastewater treatment facilities in Wisconsin, USA. *Science of the Total Environment*, *361*(1-3), 196-207.

Kouki, S., M'hiri, F., Saidi, N., Belaďd, S. & Hassen, A. (2009). Performances of a constructed wetland treating domestic wastewaters during a macrophytes life cycle. *Desalination*, *246*(1-3), 452-467.

Naji, L.A., Faisal, A.A., Rashid, H.M., Naushad, M. & Ahamad, T. (2020). Environmental remediation of synthetic leachate produced from sanitary landfills using low-cost composite sorbent. *Environmental Technology & Innovation*, *18*, 100680. https://doi.org/10.1016/j.eti.2020.100680

Naji, L.A., Jassam, S.H., Yaseen, M.J., Faisal, A.A. & Al-Ansari, N. (2020). Modification of Langmuir model for simulating initial pH and temperature effects on sorption process. *Separation Science and Technology*, *55*(15), 2729-2736.

Nunes, B., Veiga, V., Frankenbach, S., Serôdio, J. & Pinto, G. (2019). Evaluation of physiological changes induced by the fluoroquinolone antibiotic ciprofloxacin in the freshwater macrophyte species *Lemna minor* and *Lemna gibba*. *Environmental Toxicology and Pharmacology*, *72*, 103242. https://doi.org/10.1016/j.etap.2019.103242

Nunes, B., Verde, M.F. & Soares, A.M. (2015). Biochemical effects of the pharmaceutical drug paracetamol on *Anguilla anguilla*. *Environmental Science and Pollution Research*, *22*(15), 11574-11584.

Phillips, I. (2003). Does the use of antibiotics in food animals pose a risk to human health? A critical review of published data. *Journal of Antimicrobial Chemotherapy*, *53*, 28-52.

Rahi, M.A., Faisal, A.A., Naji, L.A., Almuktar, S.A., Abed, S.N. & Scholz, M. (2020). Biochemical performance modelling of non-vegetated and vegetated vertical subsurface-flow constructed wetlands treating municipal wastewater in hot and dry climate. *Journal of Water Process Engineering*, *33*, 101003. https://doi.org/10.1016/j.jwpe.2019.101003

Rakhshaee, R., Giahi, M. & Pourahmad, A. (2009). Studying effect of cell wall's carboxyl–carboxylate ratio change of *Lemna minor* to remove heavy metals from aqueous solution. *Journal of Hazardous Materials*, *163*(1), 165-173.

Ramel, F., Birtic, S., Ginies, C., Soubigou-Taconnat, L., Triantaphylidčs, C. & Havaux, M. (2012). Carotenoid oxidation products are stress signals that mediate gene responses to singlet oxygen in plants. *Proceedings of the National Academy of Sciences*, *109*(14), 5535-5540.

Saad, N., Abd Ali, Z.T., Naji, L.A., Faisal, A.A.A.H. & Al-Ansari, N. (2020). Development of Bi-Langmuir model on the sorption of cadmium onto waste foundry sand: effects of initial pH and temperature. *Environmental Engineering Research*, *25*(5), 677-684.

Sekulic, M.T., Boskovic, N., Slavkovic, A., Garunovic, J., Kolakovic, S. & Pap, S. (2019). Surface functionalised adsorbent for emerging pharmaceutical removal: adsorption performance and mechanisms. *Process Safety and Environmental Protection*, *125*, 50-63.

Thiele-Bruhn, S. (2003). Pharmaceutical antibiotic compounds in soils – a review. *Journal of Plant Nutrition and Soil Science*, *166*(2), 145-167.

Verma, R. & Suthar, S. (2015). Lead and cadmium removal from water using duckweed – *Lemna gibba* L.: Impact of pH and initial metal load. *Alexandria Engineering Journal*, *54*(4), 1297-1304.

Zhao, J.L., Ying, G.G., Liu, Y.S., Chen, F., Yang, J.F., Wang, L., Yang, Y.B., Stauber, J.L. & Warne, M.S.J. (2010). Occurrence and a screeninglevel risk assessment of human pharmaceuticals in the Pearl River system, South China. *Environmental Toxicology and Chemistry*, *29*(6), 1377-1384.

Summary

Removal of Meropenem by using *Lemna minor*. In this paper we presented a case study about the removal of a pharmaceutical contamination (in this case Meropenem) from the environment using organic natural substance (in this case study is *Lemna minor*). The study proved the efficiency of the used material to remove the contamination of three specific contamination levels of Meropenem. The experimental testing proved the concept, the effect on two vital measures (the chemical oxygen demand – COD, and the root length), which showed improvement in both measures. The degradation mechanism was proven to be not arbitrary by testing the degradation behavior measured practically to four kinetic models. The practical work was found to fit perfectly with the Grau second order model as the simulation work included in the paper shows. Based on this study it can be proven that the dangerous chemicals resulted from the residue of a pharmaceutical substances can be removed efficiently using a totally natural environmental friendly material.

Authors' address:
Noora Saad – corresponding author
Al-Nahrain University
College of Engineering
Civil Engineering Department
Al-Jadiriyah, 64074 Baghdad
Iraq
e-mail: nano_8098@yahoo.com

Samara Al-Dulaimi
University of Zakho
Faculty of Science
Department of Environmental Sciences
Zakho International Road, 12 Duhok
Kurdistan Region
Iraq

Scientific Review – Engineering and Environmental Sciences (2021), 30 (3), 496–508
Sci. Rev. Eng. Env. Sci. (2021), 30 (3)
Przegląd Naukowy – Inżynieria i Kształtowanie Środowiska (2021), 30 (3), 496–508
Prz. Nauk. Inż. Kszt. Środ. (2021), 30 (3)
http://iks.pn.sggw.pl
DOI 10.22630/PNIKS.2021.30.3.42

Marcel PAREDES[1, 2], Fausto LOPEZ[1], Tito CASTILLO[1], Alexis ANDRADE[1, 3], Valeria ARROBA[1]

[1] Universidad Nacional de Chimborazo, Facultad de Ingeniería
[2] Universidad Politécnica de Madrid, Escuela Técnica Superior de Ingenieros Industriales
[3] Universidad Politécnica de Valencia, Escuela Técnica Superior de Ingeniería de Caminos, Canales y Puertos

Sustainable acoustic insulation for prefabricated concrete homes in Andean zones

Key words: Andean zones, acoustic insulators, construction, manufactured homes

Introduction

The use of precast concrete has become a viable way to build houses due to the high degree of reliability of its properties and characteristics when controlling the quality of the process and the quality standards in the production plant (du Plessis et al., 2021). This is corroborated by the precast division of the national cement union of Ecuador (Ucem), which based on basic criteria of high productivity at low cost, industrialization and applicability (low time for assembly), show that the properties that the concrete will develop are optimal in the face of variations due to on site work restrictions (Kim, Kim & Cho, 2020). During the design and selection of construction materials, the weather is a key factor. Sudden changes in temperature directly affect the behavior of the materials (creating cracks and/or detachments) due to thermal shock (Rajeshkumar, Anandaraj, Kavinkumar & Elango, 2020). Due to its privileged geographical position, Ecuador has a variety of weather for its four regions: coast, Sierra, Amazon, and Galapagos; however, Andean zones presents the best conditions in terms of maintenance for the materials due to the cold temperatures (Cevallos, Jaramillo, Ávila & Aldaz, 2017). Andean region is made of rows of mountains, snow-capped mountains, volcanoes, high Andean peaks, valleys, and lagoons. It is characterized by a humid tropical climate in transition zones towards the coast and

the Amazon, temperate semi-humid to humid in the inter-Andean zone, hot and dry in the inter-Andean valleys and cold in the highlands and mountains in the paramos, above 3,000 m of altitude. Temperature is linked to altitude; between 1,500 and 3,000 m the average values vary between 8 and 20°C, with a temperature gradient of ~ 5°C for every 1,000 m of altitude (Narváez & León, 2001). These climatic considerations are necessary when attempting to maintain comfort in habitability. This refers to construction solutions used in a building or home to minimize the transmission of sounds (noise or noise pollution) from the outside or from an adjacent room. This can be achieved using acoustic insulation materials (Escobar, 2019). The place of origin of the acoustic materials can be mineral or natural, synthetic, and bio-based. Through the years, both materials, techniques and technologies have improved, reaching a high acoustic quality of the constructions. Countries such as Spain or Ecuador are an excellent reference in terms of research on acoustic insulation of buildings (Taban et al., 2019). Even though the construction sector offers a variety of acoustic materials, it is unknown which are the most optimal materials to use them, due to the scarce information in Ecuador on the subject (Obaco, Royuela & Matano, 2020). Consequently, it is necessary to prepare a comparative study of acoustic materials for prefabricated concrete homes for Andean zones of Ecuador. This research validates itself through its development: search and analysis of relevant updated academic and university research, data comparison and use of statistical tools and techniques that allow understanding and building a new research generating contexts; in this case on optimal acoustic materials for application in environments created with precast concrete (Guevara Patiño, 2016).

Methodology

The Delphi method was used for the determination of the best acoustic insulators, after the gathering of the information obtained by the experts, the results were validated with the AHP method (analytic hierarchy process), and organizing the information hierarchically and thus it was possible to determine the best materials for acoustic insulation in buildings in Andean area of Ecuador.

According to José, Vidal and Lluch (2019), the foundation of AHP is:

a) The structuring a hierarchical model (representation of the problem by identifying the goal, criteria, sub-criteria, and alternatives).
b) Prioritization of the elements of the hierarchical model.
c) Evaluation of the elements by assigning "weights".
d) Ranking of the alternatives according to the given weights.
e) Synthesis.
f) Analysis of sensitivity.

It is important to identify the problem in the methodology to accept the criteria of the experts and place the proposed alternatives on a list, allowing the use of these tools in solving the acoustic problem in Andean areas (Fig. 1). This will provide a series of viable solutions to builders and users.

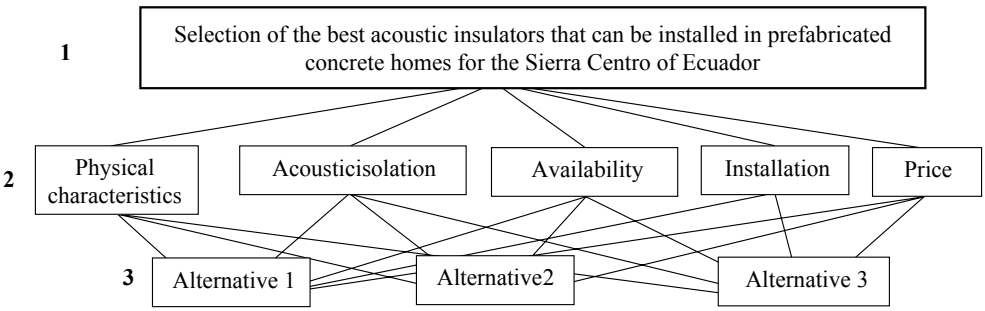

FIGURE 1. Hierarchy tree (García-Ruiz & Lena-Acebo, 2018)

The main strategy of AHP is the paired comparisons, this uses an underlying scale with values from 1 to 9 to qualify the relative preferences of two elements, that is, a comparison is made between two elements to determine the order of the alternatives (Table 1).

The prioritization of the importance, preferences, or probabilities of pair elements. Based on a common attribute or criteria represented in the decision hierarchy, it is the mathematical basis of AHP (Chandna, Saini & Kumar, 2021). In terms of quality to make the final decision, the consistency of the judgments shown during the series of paired comparisons is important. A perfect consistency is difficult to achieve, since in almost any set of paired comparisons there will always be some inconsistency; for they are judgments made by human beings. If the degree of consistency is acceptable this can be continued with the decision process, if the degree of consistency is unacceptable the decision maker will have to consider and possibly modify their judgement about the paired comparisons before continuing with the analysis. If the degree of consistency is acceptable this can be continued with the decision process, if the degree of consistency is unacceptable the decision maker will have to consider and possibly modify their judgement about the paired comparisons before continuing with the analysis.

To determine if the criteria are well evaluated, the consistency ratio (*CR*)

TABLE 1. Saaty scale for the AHP method (Lin & Kou, 2021)

Value	Definition	Comments
1	same importance	Criteria A is equal to the importance of criteria B.
3	moderated importance	Experience and judgment slightly favor criteria A over criteria B.
5	big importance	Experience and judgment strongly favor criteria A over criteria B.
7	very big importance	Criteria A is much more important than criteria B.
9	extreme importance	The greater importance of criteria A over criteria B is beyond doubt.
2, 4, 6, 8	Intermediate values between the previous ones, when it is necessary to qualify.	

calculation is used, where the result of the criteria is compared with the data shown in Table 2.

TABLE 2. Maximum percentage of consistency ratio

Matrix size	% max. *CR*
3	5%
4	9%
≥ 5	10%

Matrix size formulas used to calculate consistency ratio:

$$IC = (\lambda\_p - n) / (n - 1) \quad (1)$$

$$IA = (1.98 \cdot (n - 2)) / n \quad (2)$$

$$CR = IC / IA \quad (3)$$

where:
IC – consistency index,
CR – consistency ratio,
λ_p – average Landa,
IA – Ranm consistency,
n – array order.
Note: Landa is the quotient of the row vector and the average vector of the material comparison matrix; average Landa (λ_p) is needed to evaluate the consistency of the evaluations made by the experts (Caner & Aydin, 2021).

Results and discussion

Based on a bibliographic search on the different types of acoustic insulators, it was observed that, for an acoustic insulating material, there are no parameters defined by any regulations. However, there are some characteristics that can help to compare and choose an optimal material depending on the type of noise to be mitigated (Dong et al., 2021). In general, it is understood as "acoustic insulation" to reduce the noise level of a room (Opydo, 2004). However, the difference between the terms "isolation" and "absorption" must be considered. The acoustic absorbers are used to being materials of low density (they are light) and great flexibility. Acoustic insulators, on the other hand, are materials of high density (heavy) and greater rigidity, for each type of noise there are certain physical characteristics that the materials must meet so that their use contributes to noise reduction (Sato, Kurisu, Morimoto & Maeda, 2021). In the same manner, as the chosen insulation will be applied in the Sierra del Ecuador area in height ranges from 2,000 to 6,700 m above sea level, relevant characteristics must be considered in terms of functionality; more specifically to the data on the coefficient of thermal expansion (Bao et al., 2021). Table 3 shows the value of this characteristic of the materials and shows characteristics to be considered for the functionality of the material.

The characteristics of the acoustic insulating / absorbent materials, shown in Table 3, serve as a guide for an adequate comparison between acoustic insulating / / absorbent materials. It is worth mentioning that most of the bibliography, consulted publications, do not fully specify the physical characteristics of the tested materials (thickness, density, porosity, among others).

On the other hand, the value of the thermal shock coefficient represents the expansion of the volume of the material; here, materials shrink in cold and expand in heat (He, Huang & Jiang, 2021). The lower the coefficient of

TABLE 3. Home functionality: physical characteristics of acoustic isolators

Isolating material	Density	Thickness	Volumetric expansion coefficient	Dynamic stiffness	Endurance strength to 10%	Reference
Cork	100–120 $kg \cdot m^{-3}$	50 mm	25–50($\times 10^{-6}$) $°C^{-1}$	126 $MN \cdot m^{-3}$	0.1 MPa	(Liu, Cao, Wang, Wang & Liu, 2021)
Balsa laminated panel	140–160 $kg \cdot m^{-3}$	10–12 cm	N/A	N/A	N/A	(Cameselle-Molares, Vassilopoulos & Keller, 2019)
Audiglue	1 030 $kg \cdot m^{-3}$	N/A	N/A	N/A	N/A	(Suonox, 2019)
Fiberglass	16.02 $kg \cdot m^{-3}$	28.5 mm	12($\times 10^{-6}$) $°C^{-1}$	N/A	N/A	(Piuzzi, Scheuermann Filho, Villena Del Carpio, & Consoli, 2021)
PRFV (fiberglass reinforced plastic)	1 800 $kg \cdot m^{-3}$	1.27–5.08 cm	12($\times 10^{-6}$) $°C^{-1}$	N/A	450 MPa	(Banazadeh-Neishabouri & Shirazi, 2021)
PRFN composed with jute fiber	N/A	1.27–5.08 cm	N/A	N/A	N/A	(Sivakandhan, Murali, Tamiloli & Ravikumar, 2020)
Chipboard board plating – DM board	700 $kg \cdot m^{-3}$	25–30 mm	N/A	N/A	N/A	(Sivakandhan et al., 2020)
Polyurethane foam	45 $kg \cdot m^{-3}$	3–7 cm	5–8($\times 10^{-6}$) $°C^{-1}$	4.83 $MN \cdot m^{-3}$	0.2 MPa	(Kuranchie, Yaya & Bensah, 2021)
Polyurethane foam	10–30 $kg \cdot m^{-3}$	10 and 50 mm	30–210($\times 10^{-6}$) $°C^{-1}$	5–20 $MN \cdot m^{-3}$	200 kPa	(Tang, Lei, Huang & Xiao, 2019)
Etherboard or fiber concrete	1 250 $kg \cdot m^{-3}$	6–25 mm	0.01 $mm \cdot m^{-1} \cdot °C^{-1}$	N/A	920 kPa	(Ranaivomanana & Leklou, 2021)
Pneumatic acoustic panel recycled with resin	N/A	12 mm	N/A	N/A	N/A	(Ghofrani, Ashori, Rezvani & Arbabi Ghamsari, 2016)

Wood fiber	618 $kg \cdot m^{-3}$	4 cm	5($\times 10^{-6}$) $°C^{-1}$	N/A	200 kPa	(Cherradi et al., 2021)
PRFN coconut fiber composed	N/A	1.27–5.08 cm	N/A	N/A	N/A	(Quiñones-Bolaños et al., 2021)
Rock wool	138 $kg \cdot m^{-3}$	50 mm	7($\times 10^{-6}$) $°C^{-1}$	N/A	45 kPa	(Cheng, Lin & Huang, 2011)
Chipboard laminated panel (plywood)	720–740 $kg \cdot m^{-3}$	38 mm	N/A	25 $MN \cdot m^{-3}$	N/A	(Nishimura, 2015)
MDF laminated panel	500 and 800 $kg \cdot m^{-3}$	38 mm	25–75($\times 10^{-6}$) $°C^{-1}$	N/A	600 kPa	(Nishimura, 2015)
PRFN kenaf fiber compound	N/A	1.27–5.08 cm	N/A	N/A	N/A	(Sreenivasan, Sulaiman, Ariffin, Baharudin & Abdan, 2018)
Cabuya	124.6 $kg \cdot m^{-3}$	30 mm	N/A	N/A	N/A	(Torres & Aragon, 2006)
Abaca or hemp	125.8 $kg \cdot m^{-3}$	25 mm	N/A	10–37 $MN \cdot m^{-3}$	N/A	(Torres & Aragon, 2006)
Cellular glass	145 $kg \cdot m^{-3}$	4 cm	9($\times 10^{-6}$) $°C^{-1}$	11.14 $MN \cdot m^{-3}$	50–160 $t \cdot m^{-2}$	(Cherradi et al., 2021)
Icopor (expanded polystyrene) to 75% and rubber to 25%	N/A	3 cm	N/A	N/A	N/A	(Torres & Aragon, 2006)
Coconut fiber	117.4 $kg \cdot m^{-3}$	37 mm	N/A	7.2 $MN \cdot m^{-3}$	N/A	(Quiñones-Bolaños et al., 2021)
Encapsulated Cisco coffee in polyethylene bag	85.3 $kg \cdot m^{-3}$	N/A	N/A	N/A	N/A	(Cherradi et al., 2021)
Rice fiber	60 $kg \cdot m^{-3}$	3 cm	N/A	N/A	N/A	(Abbass & Singh, 2021)

thermal expansion, the less the material will shrink or expand with changes in temperature. A high thermal expansion coefficient affects the dimensional stability of the insulating material (Yuan et al., 2017). In cold conditions, thermal bridges occur as the material shrinks and creates joint cracks or subsidence. This causes a strong impact on the performance of the insulation because it causes premature aging of the same and the need for repair or replacement is essential.

Expert selection

With the purpose of developing both the Delphi methodology and the AHP methodology, a group of experts was brought together. They established judgments and evaluations of the criteria of applicability and functionality of the insulating materials. In the first assessment, the comparison and weight of the criteria regarding the applicability of the material in prefabricated concrete homes was established, using the Saaty numerical scale. Subsequently, the consistency of said assessments was verified, which provide coherence in the investigation, and consequently, obtained the list of acoustic insulating materials as a result.

Results of the AHP methodology

The evaluations obtained from the AHP methodology, compares not only the physical-technical properties of the materials, but also criteria regarding the selection of the materials. In other words, the set of evaluations obtained from the AHP methodology helped to generate the list of acoustic materials in descending order with the best options to be applied in manufactured homes. The consistency ratio values with the weights of the criteria and their own vectors once the average of the evaluations and judgments of the experts consulted has been completed. As these values are less than 0.1, they are useful for the purpose of research.

Table 4 shows the eigenvectors obtained with the evaluations by interviewing the experts, using the Delphi and AHP methodology (eigenvectors of each criteria and the average eigenvector once the necessary iterations have been completed), depending on "availability of the material and price", two criteria with more weight with respect to the applicability of the insulators for the prefabricated homes. This is consistent, because: it is useless for us to have information on a suitable and acoustic insulating material that cannot be found in the market and preferably in the local or national market.

TABLE 4. Eigenvectors of the criteria in AHP methodology

Physical-technical characteristics	Availability	Isolation	Installation	Own vector (weight of criteria)
0.48079291	0.080661063	0.15691286	0.1360679	0.213608682
0.152848742	0.199214723	0.06714229	0.19437598	0.153395435
0.088321967	0.457676376	0.47875944	0.34302058	0.341944591
0.201590302	0.158596394	0.19099108	0.17746785	0.182161406
0.076446079	0.103851445	0.10619434	0.14906768	0.108889886

In the same way, the price factor is decisive in the construction environment since more importance is given to lowering prices than to the insulation characteristics. This must change since noise can affect the health conditions of the people on those homes.

The consistency of the responses is less than 0.1, which translates into coherent answers that provide weight in the investigation to make the list of acoustic insulating materials.

In the evaluations of acoustic materials, several factors were taken into consideration in addition to those mentioned above: the sustainability characteristics of the material, the comparison of existing materials on the market and prototypes proposed in research, since they demonstrate to have an adequate behavior as an insulator / acoustic absorber.

To obtain the result table (Table 5) with the value of the materials: multiply the values of the tables of eigenvectors (functionality of the material) and the weight of the criteria (applicability of the material). Here, the best option is the one with the highest value.

Only materials that are used inside the house are presented in Table 5, since when comparing the values of their characteristics, they differ depending on where the material is applied. For this reason, materials exclusively for internal

TABLE 5. List of sustainable and unsustainable acoustic insulating materials

Acoustic insulating / Absorbing material	AHP assessment
Audipet	0.070696426
Audiseal	0.050828737
Sound absorbing plates (polyurethane foam)	0.049224798
Cork	0.047869328
Balsa laminated panel	0.043807815
Curtain	0.043693331
Audiglue	0.042399282
Fiberglass	0.041491311
PFRV (fiberglass reinforced plastic)	0.040225609
PRFN composed with jute fiber	0.034156729
Veneered chipboard board – DM board	0.033375732
Polyurethane foam	0.033366785
Polystyrene foam	0.033013585
Etherboard or fiber cement	0.032797451
Pneumatic acoustic panel recycled with resin	0.031420276

Acoustic insulating / Absorbing material	AHP assessment
Gypsum (plaster)	0.031133019
Wood fiber	0.030465064
PRFN composite with coconut fiber	0.030142847
Rock wool	0.029523870
Chipboard laminated panel (plywood)	0.028230806
MDF laminated panel	0.027637440
PRFN composite with kenaf fiber	0.027517869
Cabuya	0.026881398
Abaca or hemp	0.026365038
Cellular glass	0.026049431
Icopor (expanded polystyrene) at 75% and rubber at 25%	0.024062313
Coconut fiber	0.023963115
Encapsulated Cisco coffee in polyethylene bag	0.020250811
Rice fiber	0.019409784

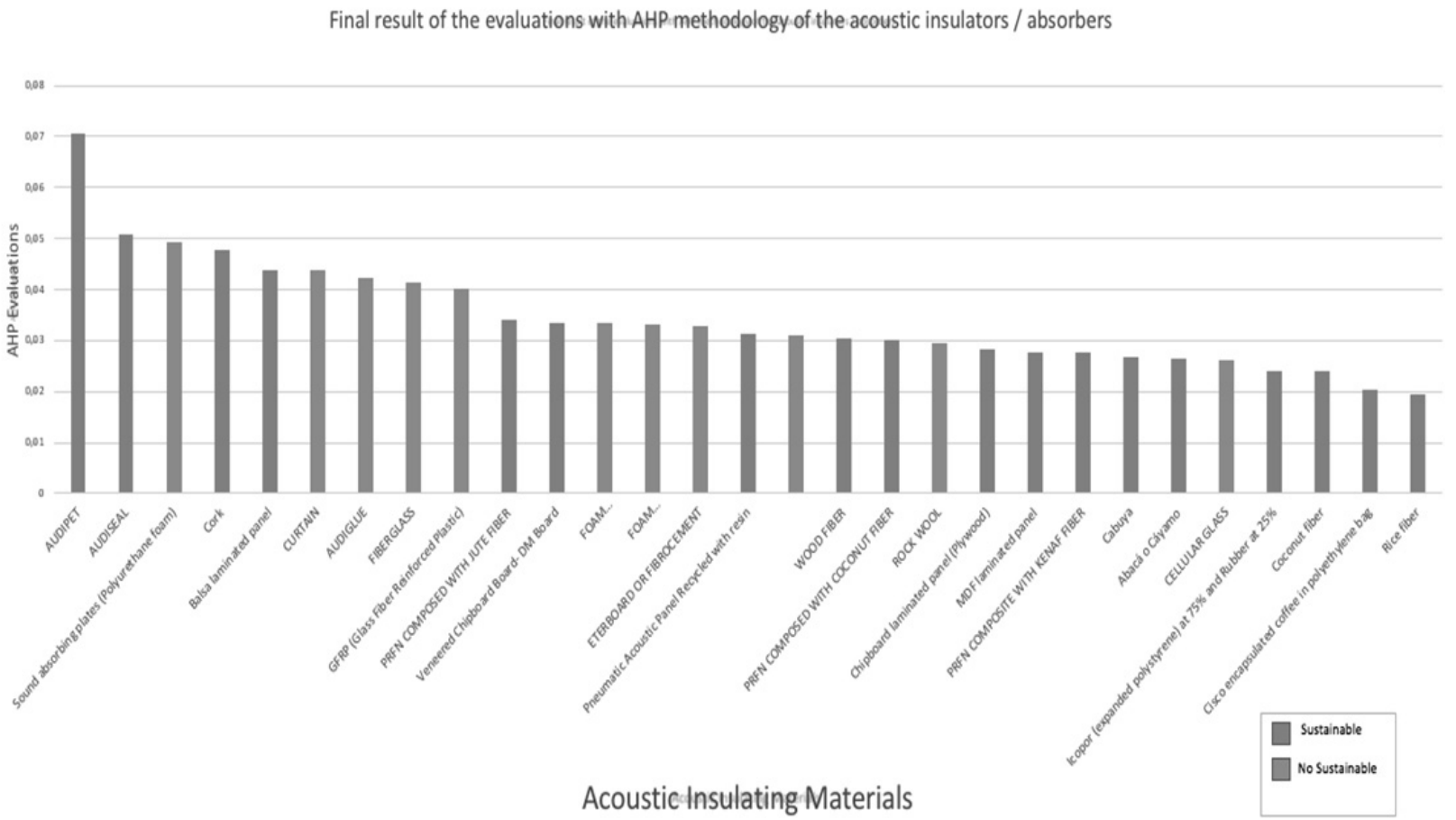

FIGURE 2. Value chart obtained by the AHP methodology

use are compared since the setting and the characteristics of the materials for outdoor use are completely different.

Acoustic insulating materials for ceilings were excluded, although they can be installed inside the building, in precast concrete homes (specifically in modular precast) the mezzanine height standard is 2.40 m, which is not optimal to use it because the living space would be reduced considerably. In Figure 2, the options of the insulators to be used in prefabricated concrete houses are presented in hierarchical order.

In Figure 2, it is evident that the sustainable materials do not present much difference once all the criteria and individual comparisons by criteria have been evaluated. This shows that they are a viable alternative to replace the use of mineral and synthetic materials that are not renewable and that use up the planet's natural resources. The notorious difference in the peaks of the bars is in the criteria of availability, since most sustainable insulators are prototypes. In other words, they are not yet found on an industrial scale, but they prove to be viable and feasible in their realization. In this way, it contributes to an increase in its useful life, to a positive impact on the environment and to the energy efficiency of the home.

Conclusions

In Ecuador there is no regulation or guide document for the characterization of acoustic materials, since most of them focus on standards for measuring the sound level in indoor and outdoor rooms, in order to later compare the results with the admissible noise levels. Likewise, the sources of information with databases of the materials do not fully specify the physical characteristics of the tested materials (thickness, density, porosity, among others). Consequently, an invitation is made to the acoustic scientific community and interested university groups to organize databases that establish the characteristics of the materials and that serve for a correct comparison of them.

It is worth mentioning that prefabricated materials with additives or resins were not compared to improve acoustic quality in the process plant; because they do not fall into the category of insulating materials to be used once the house is built. However, it is recommended to exclusively develop this type of studies in future research, to improve the quality of the material in terms of insulation and thus, obtaining acoustic comfort without the need to use a material already prepared for this purpose.

To guarantee people's health, acoustic insulation constitutes an important control in the comfort of the home; since in the long run, being subjected to noise pollution translates into health problems. Therefore, it is necessary to implement materials that help mitigate this effect.

In acoustic insulation, plastic reinforced with natural fiber (PRFN) can be classified as alternative materials to plastic reinforced with fiberglass (GRP) because its acoustic absorption coefficient varies between 0.3 NRC for coconut fibers and 0.9 NRC for jute fibers, compared to glass fibers whose absorption was 0.63 NRC. This shows that they have better acoustic absorbent performance.

References

Abbass, M. & Singh, G. (2021). Fatigue analysis of rice husk ash and basalt fibre-based sustainable geopolymer concrete in rigid pavements. *Materials Today: Proceedings*, *45*(6), 5014-5022. https://doi.org/10.1016/j.matpr.2021.01.450

Banazadeh-Neishabouri, N. & Shirazi, S.A. (2021). Development of Erosion Equations for Fiberglass Reinforced Plastic (FRP). *Wear*, 203657. https://doi.org/10.1016/j.wear.2021.203657

Bao, J., Zou, D., Zhu, S., Ma, Q., Wang, Y. & Hu, Y. (2021). A medium-temperature, metal-based, microencapsulated phase change material with a void for thermal expansion. *Chemical Engineering Journal*, *415*, 128965. https://doi.org/10.1016/j.cej.2021.128965

Cameselle-Molares, A., Vassilopoulos, A.P. & Keller, T. (2019). Two-dimensional quasi-static debonding in GFRP/balsa sandwich panels. *Composite Structures*, *215*, 391-401. https://doi.org/10.1016/j.compstruct.2019.02.077

Caner, H.I. & Aydin, C.C. (2021). Shipyard site selection by raster calculation method and AHP in GIS environment, İskenderun, Turkey. *Marine Policy*, *127*, 104439. https://doi.org/10.1016/j.marpol.2021.104439

Cevallos, O.A., Jaramillo, D., Ávila, C. & Aldaz, X. (2017). Production and quality levels of construction materials in Andean regions: A case study of Chimborazo, Ecuador. *Journal of Construction in Developing Countries*, *22*(1), 115-136. https://doi.org/10.21315/jcdc2017.22.1.7

Chandna, R., Saini, S. & Kumar, S. (2021). Fuzzy AHP based performance evaluation of massive online courses provider for online learners. *Materials Today: Proceedings* (in press). https://doi.org/10.1016/j.matpr.2021.02.255

Cheng, A., Lin, W.T. & Huang, R. (2011). Application of rock wool waste in cement-based composites. *Materials and Design*, *32*(2), 636-642. https://doi.org/10.1016/j.matdes.2010.08.014

Cherradi, Y., Rosca, I.C., Cerbu, C., Kebir, H., Guendouz, A. & Benyoucef, M. (2021). Acoustic properties for composite materials based on alfa and wood fibers. *Applied Acoustics*, *174*, 107759. https://doi.org/10.1016/j.apacoust.2020.107759

Dong, H.W., Zhao, S.D., Zhu, R., Wang, Y.S., Cheng, L. & Zhang, C. (2021). Customizing acoustic dirac cones and topological insulators in square lattices by topology optimization. *Journal of Sound and Vibration*, *493*, 115687. https://doi.org/10.1016/j.jsv.2020.115687

Escobar, A. (2019). Habitability and design: Radical interdependence and the re-earthing of cities. *Geoforum*, *101*, 132-140. https://doi.org/10.1016/j.geoforum.2019.02.015

García-Ruiz, M.E. & Lena-Acebo, F.J. (2018). Aplicación del metodo delphi en el diseño de una investigación cuantitativa sobre el fenómeno FABLAB [Application of the delphi method in the design of a quantitative investigation on the FABLABS]. *Empiria. Revista de Metodología de Ciencias Sociales*, *40*, 129-166. https://doi.org/10.5944/empiria.40.2018.22014

Ghofrani, M., Ashori, A., Rezvani, M.H. & Arbabi Ghamsari, F. (2016). Acoustical properties of plywood/waste tire rubber composite panels. *Measurement: Journal of the International Measurement Confederation*, *94*, 382-387. https://doi.org/10.1016/j.measurement.2016.08.020

Guevara Patiño, R. (2016). Estado del arte de lectura del contexto [The state of the art as a research technique: knowledge analysis or quest for new meanings]. *Folios*, *44*(2), 165-179.

He, D., Huang, D. & Jiang, D. (2021). Modeling and studies of fracture in functionally graded materials under thermal shock loading using peridynamics. *Theoretical and Applied Fracture Mechanics*, *111*, 102852. https://doi.org/10.1016/j.tafmec.2020.102852

José, F., Vidal, L. & Lluch, A.C. (2019). Diseño y validación mediante Método Delphi de un cuestionario para conocer las características de la actividad física en personas mayores que viven en residencias [Delphy Method validation and design of a questionnaire to assess physical activity]. *Retos*, *2041*(36), 515-520.

Kim, T., Kim, Y. & Cho, H. (2020). Dynamic production scheduling model under due date uncertainty in precast concrete con-

struction. *Journal of Cleaner Production*, *257*, 120527. https://doi.org/10.1016/j.jclepro.2020.120527

Kuranchie, C., Yaya, A. & Bensah, Y.D. (2021). The effect of natural fibre reinforcement on polyurethane composite foams – a review. *Scientific African*, *11*, e00722. https://doi.org/10.1016/j.sciaf.2021.e00722

Lin, C. & Kou, G. (2021). A heuristic method to rank the alternatives in the AHP synthesis. *Applied Soft Computing*, *100*, 106916. https://doi.org/10.1016/j.asoc.2020.106916

Liu, Y., Cao, Z., Wang, Y., Wang, D. & Liu, J. (2021). Experimental study of hygro-thermal characteristics of novel cement-cork mortars. *Construction and Building Materials*, *271*, 121901. https://doi.org/10.1016/j.conbuildmat.2020.121901

Narváez, G. & León, G. (2001). Caracterización y zonificación climática de la región Andina [Characterization and climatic zoning of the Andean region]. *Meteorología Colombiana*, *4*, 121-126.

Nishimura, T. (2015). Chipboard, oriented strand board (OSB) and structural composite lumber. In *Wood Composites* (pp. 103-121). Cambridge (UK): Woodhead Publishing. https://doi.org/10.1016/B978-1-78242-454-3.00006-8

Obaco, M., Royuela, V. & Matano, A. (2020). On the link between material deprivation and city size: Ecuador as a case study. *Land Use Policy*, 104761 (in press). https://doi.org/10.1016/j.landusepol.2020.104761

Opydo, W. (2004). Study of elastic waves of acoustic frequencies generated by surface partial discharges of solid insulators in vacuum. *Vacuum*, *74*(1), 85-92. https://doi.org/10.1016/j.vacuum.2003.12.159

Piuzzi, G.P., Scheuermann Filho, H.C., Villena Del Carpio, J.A. & Consoli, N.C. (2021). The effects of porosity, asphalt content and fiberglass incorporation on the tensile strength and resilient modulus of asphalt concrete blends. *Geotextiles and Geomembranes*, *49*(3), 864-870. https://doi.org/10.1016/j.geotexmem.2021.01.002

Plessis, A. du, Babafemi, A.J., Paul, S.C., Panda, B., Tran, J.P. & Broeckhoven, C. (2021). Biomimicry for 3D concrete printing: a review and perspective. *Additive Manufacturing*, *38*, 101823. https://doi.org/10.1016/j.addma.2020.101823

Quiñones-Bolaños, E., Gómez-Oviedo, M., Mouthon-Bello, J., Sierra-Vitola, L., Berardi, U. & Bustillo-Lecompte, C. (2021). Potential use of coconut fibre modified mortars to enhance thermal comfort in low-income housing. *Journal of Environmental Management*, *277*, 111503. https://doi.org/10.1016/j.jenvman.2020.111503

Rajeshkumar, V., Anandaraj, S., Kavinkumar, V. & Elango, K.S. (2020). Analysis of factors influencing formwork material selection in construction buildings. *Materials Today: Proceedings*, *37*(2), 880-885. https://doi.org/10.1016/j.matpr.2020.06.044

Ranaivomanana, H. & Leklou, N. (2021). Investigation of microstructural and mechanical properties of partially hydrated Asbestos-Free fiber cement waste (AFFC) based concretes: experimental study and predictive modeling. *Construction and Building Materials*, *277*, 121943. https://doi.org/10.1016/j.conbuildmat.2020.121943

Sato, H., Kurisu, K., Morimoto, M. & Maeda, M. (2021). Effects of rainfall rate on physical characteristics of outdoor noise from the viewpoint of outdoor acoustic mass notification system. *Applied Acoustics*, *172*, 107616. https://doi.org/10.1016/j.apacoust.2020.107616

Sivakandhan, C., Murali, G., Tamiloli, N. & Ravikumar, L. (2020). Studies on mechanical properties of sisal and jute fiber hybrid sandwich composite. *Materials Today: Proceedings*, *21*, 404-407. https://doi.org/10.1016/j.matpr.2019.06.374

Sreenivasan, S., Sulaiman, S., Ariffin, M.K.A.M., Baharudin, B.T.H.T. & Abdan, K. (2018). Physical properties of Novel Kenaf Short Fiber Reinforced Bulk Molding Compounds (BMC) for Compression Moulding. In *Materials Today: Proceedings*, *5*, 1226-1232. https://doi.org/10.1016/j.matpr.2017.11.205

Suonox (2019). *Audiglue, silence the noise*. Monterrey (Mexico): Suonox.

Taban, E., Khavanin, A., Ohadi, A., Putra, A., Jafari, A.J., Faridan, M. & Soleimanian, A. (2019). Study on the acoustic characteristics of natural date palm fibres: Experimental and theoretical approaches. *Building and*

Environment, *161*, 106274. https://doi.org/10.1016/j.buildenv.2019.106274

Tang, N., Lei, D., Huang, D. & Xiao, R. (2019). Mechanical performance of polystyrene foam (EPS): Experimental and numerical analysis. *Polymer Testing*, *73*, 359-365. https://doi.org/10.1016/j.polymertesting.2018.12.001

Torres, F.G. & Aragon, C.L. (2006). Final product testing of rotational moulded natural fibre--reinforced polyethylene. *Polymer Testing*, *25*(4), 568-577. https://doi.org/10.1016/j.polymertesting.2006.03.010

Yuan, J.M., Feng, Y.R., Wu, Z.J., Wang, Y.J., Li, S.Y. & Sun, P. (2017). A carbon fiber network/polypropylene composite with a low thermal expansion coefficient and high stiffness. *Xinxing Tan Cailiao/New Carbon Materials*, *32*(3), 271-276. https://doi.org/10.1016/j.carbon.2017.06.069

Summary

Sustainable acoustic insulation for prefabricated concrete homes in Andean zones. The construction sector is undoubtedly one of the main promoters for economic and social development. The modern concept of the prefabrication of elements originated from the industrial revolution to reduce costs and increase production through the mechanization of work, increasing the quality and ease of control in the plant. Prefabricated concrete homes are aimed at the popular sectors, however, when talking about acoustic habitability comfort we refer to constructive solutions used in a building to minimize the transmission of sounds (noise pollution) from outside or from an adjoining enclosure. This is achieved with the use of acoustic insulation materials. In the present research, through a bibliographic review, the updated state-of-the-art search methodology is developed, supported by the Delphi and AHP (hierarchical analytical process) methods and with the opinion of experts to compare the properties of acoustic insulating materials; in order to publicize the best acoustic insulators to be installed inside prefabricated concrete homes. Within the bibliographic review, new technologies with sustainable materials found as feasible prototypes were investigated in Ecuador, where thanks to its diversity of ecosystems and the necessary existing technology, the natural fibers used in the prototypes for insulation/absorption are easily found acoustics in homes.

Authors' address:
Marcel Paredes – corresponding author
(https://orcid.org/0000-0002-3762-9633)
Universidad Nacional de Chimborazo
Facultad de Ingeniería
Av. Antonio José de Sucre, Riobamba
Ecuador
e-mail: marcelparedes@unach.edu.ec

Alexis Andrade
Universidad Nacional de Chimborazo
Facultad de Ingeniería
Av. Antonio José de Sucre, Riobamba
Ecuador

Universidad Politécnica de Valencia
Camí de Vera, s/n, 46022 Valencia
España

Fausto Lopez
Tito Castillo
Valeria Arroba
Universidad Politécnica de Valencia
Camí de Vera, s/n, 46022 Valencia
España